Title

Dynamics and Heterogeneity of Hypothalamus and White Adipose Tissue under Internal and External Cues

Author

Li, Gaoyan

Publication Date

2023

UNIVERSITY OF CALIFORNIA

Los Angeles

Dynamics and Heterogeneity of Hypothalamus and White Adipose Tissue under Internal and External Cues

A dissertation submitted in partial satisfaction of the
requirements for the degree Doctor of Philosophy
in Molecular, Cellular, and Integrative Physiology

by

Gaoyan Li

2023

ABSTRACT OF THE DISSERTATION

Dynamics and Heterogeneity of Hypothalamus and White Adipose Tissue under Internal and External Cues

by

Gaoyan Li
Doctor of Philosophy in Molecular, Cellular, and Integrative Physiology
University of California, Los Angeles, 2023
Professor Xia Yang, Chair

The hypothalamus and the white adipose tissue are both key regulator of energy homeostasis. The hypothalamus is the central hub in metabolic control and links the neuronal, endocrine, and metabolic systems. White adipose tissue (WAT) is highly metabolically dynamic and has emerged as a multifaceted endocrine organ with crucial roles in energy metabolism. Characterized by cell type heterogeneity, these key metabolic tissues exhibit complex cell-type-specific dynamics in response to numerous factors, including age, sex, nutritional state, and pharmacological interventions. Discerning the impacts of these factors broadens our understanding of how metabolic tissue dynamics are shaped and their implications for the development of metabolic disorders. This knowledge further holds promise for the advent of personalized therapeutic strategies. Our research commences by probing the influences of the sex chromosome effect (SCE) and gonadal sex effect (GSE) at a cellular level in the hypothalamus, employing the Four Core Genotypes (FCG) mouse model and single-cell RNA sequencing (scRNA-seq). Analyses of SCE, GSE, and SCE-GSE interactions show that they contribute over 70% of the genetically determined normative sex differences across all hypothalamic cell types and neuronal subtypes. Notably, enrichment analyses of Genome-Wide Association Study (GWAS) signals of these sex factor-specific differentially expressed genes (DEGs) highlight their relevance to neurological disorders, obesity, and Type 2 diabetes. Therefore, the comprehensive understanding of cell types and pathways underlying sex-specific risks paves the way for sex-based personalized therapies. Next, we turn our attention to aging and its effects on WAT. Our findings unveil a surprising age-induced surge in adipogenesis, particularly in visceral fat. Contrary to the conventional age-associated decline in stem cell activity, we reveal that adipocyte progenitor cells (APCs) enhance their adipogenic potential during aging. We identify and characterize a novel Committed Preadipocyte population uniquely enriched in aged mice (CP-A) through scRNA-seq, showcasing high proliferation and adipogenesis activity. Furthermore, we delineate Leukemia Inhibitory Factor Receptor (LIFR) as a functional marker of CP-A, thereby uncovering a novel mechanism pertinent to fat tissue aging with potential clinical implications for age-related metabolic disorders. Lastly, we elucidate the effects of the PPARγ activator rosiglitazone on WAT remodeling and cellular reprogramming in obesity. We demonstrate rosiglitazone's profound influences on adipogenesis, gene expression modulation in epididymal white adipose tissue (eWAT) and inguinal white adipose tissue (iWAT) progenitor cells and preadipocytes, inflammation mitigation, and the promotion of ATP synthesis and ribosome biogenesis. Interestingly, our data suggest a potential role of PPARγ in enhancing ribosome biogenesis efficiency, a facet that merits future exploration. In summary, our studies underscore the importance of understanding the varying metabolic processes and cellular dynamics across metabolic tissues under the influence of internal and external cues, including age, sex, nutritional state, and pharmacological intervention. The delineation of the precise cell types and molecular mechanisms underlying health modulating factors will bolster target identification and pave the way for personalized therapeutic interventions.

The dissertation of Gaoyan Li is approved.

Aldons J Lusis

Claudio Javier Villanueva

Qiong Annabel Wang

Xia Yang, Committee Chair

University of California, Los Angeles

2023

DEDICATION

This dissertation is dedicated to Yang lab members, Junbo Wang and my cat Da-He Li, who accompanied and supported me through this journey towards this PhD.

TABLE OF CONTENTS

ABSTRACT OF THE DISSERTATION ii

DEDICATION vi

TABLE OF CONTENTS vii

LIST OF FIGURES ix

LIST OF TABLES ix

ACKNOWLEDGEMENT xii

VITA xiv

Chapter 1. Introduction 1

Chapter 2. Dissecting the effects of sex chromosomes versus gonads on cellular gene expression in the hypothalamus 4

- 2.1 Introduction 4
- 2.2 Results 4
- 2.3 Discussion 31
- 2.4 Conclusions 34
- 2.5 Methods 34
- 2.6 Figures 40
- 2.7 Tables 59

Chapter 3. Characterizing the effect of aging in mouse visceral WAT 60

- 3.1 Introduction 60
- 3.2 Results 62
- 3.3 Discussion 76
- 3.4 Conclusions 83
- 3.5 Methods 83
- 3.6 Figures 97

Chapter 4. PPARg-Dependent Remodeling of Translational Machinery in Adipose....... 127

4.1 Introduction 127

4.2 Results 129

4.3 Discussion 140

4.4 Conclusions 142

4.5 Methods 143

4.6 Figures 153

References 174

LIST OF FIGURES

Fig 2. 1 Work flow for examining cell-type specific gonadal sex effect and sex chromosome effect in the hypothalamus with four core genotype model 40

Fig 2. 2 Eleven cell types identified in hypothalamus 40

Fig 2. 3 Fifteen neuronal subtypes identified in hypothalamic neurons 42

Fig 2. 4 Differentially expressed genes detected by linear model based method across cell types 43

Fig 2. 5 Differentially expressed genes detected by linear model based method across neuronal subtypes 45

Fig 2. 6 Differentially expressed genes detected by pairwise comparison across cell types........ 47

Fig 2. 7 Differentially expressed genes detected by pairwise comparison across neuronal subtypes 49

Fig 2. 8 Pathways enriched in cell type specific DEGs affected by SCE , GSE and normative sex differences 51

Fig 2. 9 Pathways enriched in neuronal subtype specific DEGs affected by SCE , GSE and normative sex differences........ 53

Fig 2. 10 Sexually dimorphic genes associate with diseases or phenotype GWAS at cell type level 55

Fig 3. 1 APCs in aged mice have a high adipogenic rate *in vivo*……….98

Fig 3. 2 scRNA-seq analysis identifies a novel, age-specific APC population........ 99

Fig 3. 3 CP-A cells are highly proliferative and adipogenic *in vitro* and *in vivo*........ 102

Fig 3. 4 The high adipogenic capacity of CP-A cells is dependent on LIFR 105

Sup Fig 3. 1 Aged mice display substantial fat gain and reduced metabolic rate……….108

Sup Fig 3. 2 Aged mice show new adipogenesis in gWAT 110

Sup Fig 3. 3 Aged mice exhibit high adipocyte regeneration capacity 112

Sup Fig 3. 4 Aged microenvironment does not promote adipogenesis of APCs in young mice........ 115

Sup Fig 3. 5 scRNA-seq of Lin- SVFs in gWAT of young and aged male mice. 116

Sup Fig 3. 6 Comparison of ACS, IAP, CP-1, CP-2, and CP-A populations with previously identified APC populations........ 118

Sup Fig 3. 7 Single-cell RNA-seq analysis of human APCs 120

Sup Fig 3. 8 Enriching APC populations and *in vitro* 3D culture of APCs 122

Sup Fig 3. 9 CP-A cells have high adipogenic potential *in vivo* 125

Sup Fig 3. 10 LIFR signaling controls CP-A adipogenesis 126

Fig 4. 1 Adipose tissue remodeling after acute rosiglitazone treatment……………153

Fig 4. 2 Single-Cell RNA Sequencing Uncovers Stromal Vascular Cell Remodeling after PPARγ agonist treatment 157

Fig 4. 3 Remodeling of epididymal adipocyte precursor cells in response to PPARg agonist.......... 163

Fig 4. 4 Rosiglitazone-driven enhancement of adipocyte differentiation in inguinal adipose tissue 165

Fig 4. 5 Comparison of differently expressed and enriched pathways in response to obesity and rosiglitazone treatment 167

Fig 4. 6 PPARg-driven enhancement in translation efficiency 171

Fig 4. 7 PPARg binding sites in ribosomal genes 172

Sup Fig 4. 1 Host physiology remodeling after rosiglitazone treatment……………155

Sup Fig 4. 2 Adipose stromal vascular fraction Single-Cell RNA Sequencing quality control 159

Sup Fig 4. 3 Adipose-specific macrophage profile remodeling after PPARg agonist treatment.......... 161

Sup Fig 4. 4 Effects of rosiglitazone treatment in the stromal vascular fraction of epididymal adipose tissue 169

LIST OF TABLES

Table 2. 1 Human GWAS of 71 traits and diseases from 16 consortiums used in marker set enrichment analysis (MSEA) 59

ACKNOWLEDGEMENT

I am incredibly grateful to my exceptional advisor, Professor Xia Yang, for her unwavering support and endless guidance throughout my doctoral journey, both academically and personally. I have been more than lucky to have had Dr. Yang as my advisor. I would also like to extend my heartfelt appreciation to my doctoral committee, lab mates, and friends, whose constant encouragement and assistance have made my PhD experience truly rewarding. Lastly, the past several years wouldn't have been as joyful without Junbo by my side.

Chapter 2 is a version of unpublished work Li G, Ahn I, Chen X, Diamante G, Blencowe M, Zhao Y,Arnold A, Yang X. "Dissecting the effects of sex chromosomes versus gonads on cellular gene expression in the hypothalamus." This work was supported by NIH grant R01HD100298 and Iris-Cantor /CTSI Pilot Project Funding.

Chapter 3 is a version of unpublished work Wang G, Li G, Song A, Dai W, Wang Z, Shamlin N, Qin H, Medrano L, Dow J, Li A, Brown L, Armstrong B, Fueger P, Campisi J, Wu X, Jiang L, Yang X, Wang Q. "Distinct adipose progenitor cells emerging with age drive active adipogenesis." This work was supported by NIH grant R01HD096152, R01DK128907, the American Diabetes Association Junior Faculty Development Award 1-19-JDF-023, and the Caltech-COH Initiative Award.

Chapter 4 is a version of unpublished work De Siqueira M, Li G, Zhao Y, Ahn I, Matulionis N, Ramirez C, Tamboline M, Hildreth A, Larios J, Xu S, O'Sullivan T,

Christofk H, Mack J, Yang X, Villanueva C. “PPARg - dependent Remodeling of Translational Machinery in Adipose Progenitors” This work was supported by NIH grant UL1TR001881.

VITA

EDUCATION

2023	PhD Candidate, Molecular, Cellular, and Integrative Physiology University of California, Los Angeles
2018	Bachelor of Science, Biological Sciences Nanjing University, Jiang Su, China

RESEARCH EXPERIENCE

2018 – Present	PhD trainee Department of Integrative Biology and Physiology University of California, Los Angeles
2016 – 2018	Student researcher Department of Life Sciences Nanjing University

MANUSCRIPTS (*, co-first author)

Li G, Ahn I, Chen X, Diamante G, Blencowe M, Zhao Y,Arnold A, Yang X. Dissecting the effects of sex chromosomes versus gonads on cellular gene expression in the hypothalamus.

Wang G*, Li G*, Song A, Dai W, Wang Z, Shamlin N, Qin H, Medrano L, Dow J, Li A, Brown L, Armstrong B, Fueger P, Campisi J, Wu X, Jiang L, Yang X, Wang Q. Distinct adipose progenitor cells emerging with age drive active adipogenesis.

De Siqueira M*, Li G*, Zhao Y, Ahn I, Matulionis N, Ramirez C, Tamboline M, Hildreth A, Larios J, Xu S, O'Sullivan T, Christofk H, Mack J, Yang X, Villanueva C. "PPARg - dependent Remodeling of Translational Machinery in Adipose Progenitors"

PEER-REVIEWED PUBLICATIONS

Ding, J., Blencowe, M., Nghiem, T., Ha, S.M., Chen, Y.W., Li, G. and Yang, X., 2021. Mergeomics 2.0: a web server for multi-omics data integration to elucidate disease networks and predict therapeutics. Nucleic acids research, 49(W1), pp.W375-W387.

AWARDS

2021	Iris Cantor - UCLA Women's Health Center/CTSI Young Investigator Award
2020	Molecular Cellular and Integrative Physiology Program retreat Best Poster Award, UCLA

Chapter 1. Introduction

The hypothalamus plays a pivotal role in regulating numerous physiological processes, including hunger, satiety, energy expenditure, and glucose homeostasis[1]. Neurons in the hypothalamus integrate signals related to energy status and then orchestrate appropriate behavioral and metabolic responses. Dysregulation of these pathways can result in cardiometabolic disorders such as obesity and type 2 diabetes[2]. White adipose tissue (WAT), on the other hand, has traditionally been viewed as a passive storage depot for energy. However, research in recent years has revealed that WAT is a highly active endocrine organ, releasing a variety of hormones, cytokines, and adipokines. These adipokines have diverse functions, influencing appetite and energy expenditure, insulin sensitivity, inflammation, and lipid metabolism[3]. Imbalance in the production or function of adipokines can contribute to cardiometabolic disorders[4]. Characterized by cell-type heterogeneity, these key metabolic tissues exhibit complex cell-type-specific dynamics in response to numerous factors, including age, sex, nutritional state, and pharmacological interventions. These differences in cell type composition and cellular interactions can induce profound effects on metabolism. Given there are multiple types of factors affecting hypothalamus and adipose tissue function, a thorough understanding of the dynamics of cell type composition, the specific gene expression patterns, and the cell type interactions under different physiological or pathological states is essential. The emergence of single-cell transcriptomic approaches has made it possible to study the cellular heterogeneity and functional states in metabolic tissues at the cell type level and set the stage to allow retrieval of cell type specific mechanisms of metabolic diseases.

This dissertation seeks to explore the influences of sex, aging, and drug treatment on cell type composition, gene expression patterns, cell lineage dynamics, and cell-cell interaction within the hypothalamus and WAT. The insights gained from examining these effects elucidate how metabolic tissue dynamics are molded and their implications for metabolic disorder development, ultimately facilitating the development of personalized therapeutic strategies.

In **Chapter 2**, we examine the influences of sex chromosome effect (SCE) and gonadal sex effect (GSE) at a cellular level in the hypothalamus, employing the Four Core Genotypes (FCG) mouse model and single-cell RNA sequencing (scRNA-seq). This analysis identified 11 distinct cell types and 15 neuronal subtypes within the hypothalamus. Based on the analysis of sex-factor-specific and cell type-specific differentially expressed genes, SCE, GSE, and SCE-GSE interactions account for over 70% of the genetically determined normative sex differences across all hypothalamic cell types and neuronal subtypes. Moreover, marker set enrichment analysis of GWAS signals in these sex-factor-specific and differentially expressed genes revealed significant enrichment in neurological disorders, obesity, and type 2 diabetes-related GWAS. Such understanding of these sex differences in the hypothalamus and their potential implications for disease susceptibility and progression is a crucial area of research, paving the way for sex-specific personalized therapies.

In **Chapter 3**, we delve into the impacts of aging on white adipose tissue. We observe that mice mirror human age-associated adipose tissue expansion. Utilizing *in vivo* lineage tracing, we document substantial adipogenesis, particularly in visceral fat, induced by aging. Interestingly, this contrasts with the typical decline in the proliferative and differentiative capacities exhibited by most adult stem cell types, as the adipogenic potential of adipocyte progenitor cells (APCs) appears to be activated with aging. Both *in vivo* transplantation and three-dimensional imaging of transplants demonstrate that APCs from aged mice autonomously exhibit an elevated adipogenic potential. scRNA-seq analysis exposed a global remodeling of APCs instigated by aging. Within this context, we discern a unique Committed Preadipocyte population that is significantly enriched in aged mice (referred to as CP-A), which also exists in humans, and is characterized by a global activation of proliferation and adipogenesis pathways. CP-A cells show high proliferation and adipogenic activity, both *in vitro* and *in vivo*. We identify LIFR as a functional marker of CP-A cells, which is conducive to the adipogenesis of CP-A. Collectively, these observations delineate a novel foundational mechanism implicated in fat tissue aging and hold the potential for the prevention and treatment of age-associated metabolic disorders

In **Chapter 4**, we elucidate the effects of the PPARγ activator rosiglitazone on WAT remodeling and cellular reprogramming in obesity. This study provides a cell type-specific view of how acute rosiglitazone treatment influences white adipose tissue remodeling and cellular reprogramming in the context of obesity. Rosiglitazone was found to induce adipogenesis, reduce progenitor cells, and alter the transcriptomic landscape of both eWAT and iWAT progenitor cells and preadipocytes. Moreover, rosiglitazone demonstrated the capacity to alleviate inflammatory responses and enhance ATP synthesis and ribosome biogenesis in iWAT cells. The observed shift in macrophage subpopulations further illustrates the potent immunomodulatory effects of rosiglitazone. These findings suggest a novel potential role for PPARγ in enhancing translation efficiency, underscoring the need for further investigation into its mechanism. This study thus opens new avenues for understanding the cellular and molecular mechanisms underpinning adipose tissue remodeling and the therapeutic effects of PPARγ agonists in the context of obesity.

In summary, our research emphasizes the importance of understanding the cellular dynamics and diverse metabolic processes across metabolic tissues influenced by various internal and external cues, inclusive of age, sex, nutritional status, and pharmacological interventions. Elucidating the specific cell types and molecular mechanisms underlying health modulating factors will enhance target identification, thus fostering the development of personalized therapeutic strategies.

Chapter 2. Dissecting the effects of sex chromosomes versus gonads on cellular gene expression in Hypothalamus

2.1 Introduction

The hypothalamus, one of the most complex brain regions, is the central regulator of energy homeostasis and links the neuronal, endocrine, and metabolic systems[1]. A number of sex differences were reported in both human and murine hypothalami at the structural, functional and molecular levels[5]. Structural differences included variations in the size and number of neurons in specific nuclei, such as the sexually dimorphic nucleus (SDN) and the ventromedial nucleus (VMN)[6]. As the hypothalamus is heavily involved in the regulation of hormone release, the control of reproductive hormones also have differing roles and responses between sexes. In females, the hypothalamus orchestrates the menstrual or estrous cycle through the secretion of gonadotropin-releasing hormone (GnRH), which stimulates the pituitary to release follicle-stimulating hormone (FSH) and luteinizing hormone (LH). In males, GnRH stimulates the release of LH and FSH to regulate testosterone production and spermatogenesis[7]. Sex differences in the hypothalamus also contribute to disparities in behavior and physiological responses such as feeding behavior, stress response, thermoregulation, and circadian rhythms[8,9]. Sex-specific patterns of hypothalamic activity have been implicated in the sex differences in the prevalence, progression and outcomes of metabolic symptoms, psychiatric diseases and neurological disorders such as depression, anxiety, eating disorders, and metabolic syndrome[1,10–13]. However, the mechanisms behind these sex biases and their effect on the individual cell types and brain regions is still unclear.

Sex differences in tissue functions and disease susceptibility can arise from two biological factors: gonadal sex effect (GSE) and/or the sex chromosome effect (SCE). To date, little is known about the relative contribution of GSE vs SCE and their interactions in the hypothalamus. Moreover, the hypothalamus contains heterogeneous cell populations and neuronal subtypes. Though recent progress in single-cell RNA sequencing (scRNA-seq) has facilitated the transcriptional cataloguing of cell types in the hypothalamus, sex differences attributable to GSE or SCE in individual cell types have yet to be investigated. Understanding the effects of gonadal sex and sex chromosomes on cell-type specific gene regulation will be critical for a high-resolution understanding of sex-biased mechanisms in diseases and the implementation of precision medicine for each sex.

Dissecting GSE vs SCE is challenging because female gonads typically co-occur with XX chromosomes and male gonads with XY chromosomes. Here we used the Four Core Genotypes (FCG) mouse model to separate GSE and SCE. Deletion of the testis determining Sry gene on Y chromosome and insertion of Sry on Chromosome 3 allow the FCG model to consist of 4 types of mice: gonadal males with either XX or XY sex chromosomes, and gonadal females with XX or XY sex chromosomes, which allow for the separation of GSE from SCE[15]. Sex differences between gonadal males and females can be attributed to the effect of gonads and hormones, while differences between XX and XY mice can be attributed to the effects of the X or Y chromosome.

By utilizing the FCG Model, it becomes possible to delineate the distinct contributions of sex chromosome effects and gonadal effects on hypothalamic function at the cellular level, via the application of scRNA-seq. A comprehensive understanding of the molecular physiology underlying the impact of sex differences on hypothalamic functions carries considerable importance. Such knowledge has potential implications in the prevention of diseases with a sex bias, as well as in the facilitation of personalized therapies tailored according to sex.

2.2 Results

Study Overview

Here, our study used the FCG mice to examine cell-type specific GSE vs SCE using scRNAseq. We compared the single-cell transcriptome between four core genotypes to identify the cell types and neuronal subtypes and their corresponding differently expressed genes (DEGs) and pathways influenced by GSE and SCE. And we further investigated the association of the sex-biased genes and circuits with metabolic diseases based on their enrichment patterns for hypothalamus-specific expression quantitative trait loci (eQTL) and splicing quantitative trait loci (sQTL) associated with over 71 GWAS datasets for a broad range of metabolic diseases and neurological disorders with known sex differences. Our cell-level analysis also uncovered larger SCEs in specific cell populations that are masked in low-resolution bulk tissue analysis. （**Figure 2.1**）

11 Cell types identified by hypothalamus scRNAseq

An investigation into the contributions of SCE and GSE to sex differences in the hypothalamus was conducted through single-cell RNA sequencing of all four genotypes in the Four Core Genotype model. These include gonadal males with XX sex chromosomes (XXM), gonadal males with XY sex chromosomes (XYM), gonadal females with XX sex chromosomes (XXF), and gonadal females with XY sex chromosomes (XYF). Briefly, fastq files from the Drop-seq sequencing data were processed using Drop-seq tools (v1.12) and aligned with the mouse reference genome (mm10) via STAR-2.5.0c[22]. A threshold of at least 500 genes and 900 transcripts, with no more than 20% of the total reads being mitochondrial, was used to distinguish single cells from background noise.

The Louvain algorithm was applied to determine cell clusters based on transcriptome pattern similarities, and the clusters were subsequently visualized using Uniform Manifold Approximation and Projection (UMAP). This allowed for the identification of 11 major cell types in the hypothalamus, including neurons, astrocytes, ependymal cells, endothelial cells, tanycytes, myelinating oligodendrocytes, newly formed oligodendrocytes, oligodendrocyte progenitor cells, microglia, mural cells including pericytes and vascular smooth muscle cells (VSMCs), and vascular leptomeningeal cells (**Figure 2.2A**). The cluster-specific expression patterns of these cell types were confirmed by examining specific cell-type markers such as Snap25 and Syt1 for neurons, and Agt for astrocytes (**Figure 2.2B**).

Upon further exploration of cell-type expression patterns across all four genotypes (**Figure 2.2C**), differences in expression patterns among all cell types on the UMAP became evident. In order to visually isolate the effects of the gonadal and chromosomal contributions, UMAPs were generated that focused exclusively on genotypes with different sex chromosomes and the same gonads (**Figure 2.2D**), and on genotypes with the different gonads and same sex chromosomes (**Figure 2.2E**). Visible differences, especially in neurons, were observed between XX and XY chromosomes, indicating a substantial contribution from sex chromosome differences. Contrastingly, differences between the gonadal female group and gonadal male group were less pronounced, suggesting a more modest contribution from gonadal differences. This observation underscores the interplay of both gonadal and chromosomal contributions to expression differences in hypothalamic cells, with sex chromosome differences having a major impact.

15 Neuronal subtypes identified by hypothalamus scRNAseq

As the expression file of hypothalamus neurons are sensitive to both SCE and GSE, neurons in the hypothalamus are highly functionally heterogenic and play an essential role in maintaining bodily homeostasis. This regulatory function encompasses a range of processes, including temperature regulation, hunger, thirst, sleep, and circadian rhythms[1,23]. Different types of neurons achieve these functions via the secretion of numerous neuropeptides. For example, agouti-related peptide is a neuropeptide that acts as an antagonist of the melanocortin receptors MC3R and MC4R in the hypothalamus. It stimulates appetite and reduces metabolism, promoting weight gain. Another neuropeptide, arginine vasopressin, is involved in water retention and increased vascular resistance, leading to increased blood pressure[24,25].

Aiming to be more precise on neuronal subtype annotation and to pinpoint whether sex differences were more pronounced within these diverse neuron populations, the focus was narrowed to only the neuron cluster. The cluster was separated and further divided into fifteen subclusters using integrated canonical correlation analysis[26] of the four genotypes, thereby refining the characterization of hypothalamic neuronal diversity (**Figure 2.3A**).

The identities of these cell types were elucidated by obtaining gene signatures specific to each cluster and comparing them to known genes associated with hypothalamic peptides. Consequently, subclusters of neurons expressing Agrp (Agouti-related protein), Npy (Neuropeptide Y), Avp (Arginine Vasopressin), Oxt (Oxytocin), Bdnf (Brain-derived neurotrophic factor), Cck (Cholecystokinin), Gal (Galanin), Nrgn (Neurogranin), Pomc (Proopiomelanocortin), Tac2 (Neurokinin B), and Vip (Vasoactive intestinal peptide) were identified. The remaining clusters, devoid of subtype-specific hypothalamic peptide gene expression, were named after their specific marker genes. These marker genes were required to be expressed in at least 20% of the single cells within the cluster of interest, to exhibit at least a 0.25 log-fold change compared to other cells, and to possess a false discovery rate (FDR) below 5% (**Figure 2.3B**).

While canonical correlation analysis (CCA) was performed on the four genotypes for more refined annotation of viable neuronal subtypes, the clustering based on the corrected CCA also minimized the visualized expression pattern differences between genotypes (**Figure 2.3C**). Thus, our exploration of the neuronal subtype expression patterns across all four genotypes was based on the Louvain clustering of the top 15 Principal Components. Differences in expression patterns are evident on the tSNE plot (**Figure 2.3D**). Although XXF, XYF, and XXM genotypes exhibited remarkably similar expression patterns, the pattern for the XYM genotype significantly deviated from the other three. This observation underscores the distinct contributions of both SCE and GSE to sex differences in the neuronal subtypes of the hypothalamus, particularly within the XYM genotype.

Differently expressed genes influenced by individual sex factors

To determine which genes were affected by Sex Chromosome Effect and/or Gonadal Sex Effect, we performed both linear model based DEG analysis and pairwise DEG analysis. Linear model based DEGs were identified using the Limma R package[27], which utilized the model Y = A1SCE + A2GSE + A12SCE-GSE. In this way, we were able to identify the genes differently expressed due to SCE, GSE and SCE-GSE Interaction separately by comparing all four groups together in a cell type specific manner. Pairwise DEGs were identified by Wilcoxon Rank Sum test between 4 pair-wise comparisons. The comparisons including 1.XXF vs XYF to identify SCE on gonadal female background 2.XXM vs XYM to identify SCE on gonadal male background 3.XXF vs XXM to identify GSE on XX sex chromosome background 4.XYF vs XYM to identify GSE on XY sex chromosome background. To delve into how each individual sex factor contributes to the general normative sex difference phenotype, DEGs were also generated by comparing XXF and XYM in both comparison methods as a standard of reference.

Overlapped effects and unique contributions of linear model based DEGs influenced by individual sex factors across cell types

In an examination of the linear model-based DEGs under various sex factors, neurons, endothelial cells, and astrocytes emerge as the most affected cell types for both SCE and SCE-GSE interaction (**Figure 2.4B**). In the case of GSE, the most influenced cell types include neurons, endothelial cells, and ependymal cells. Across these three sex factors (SCE, GSE and SCE-GSE interaction), neurons appear to be the most significantly impacted cell type, an observation that aligns with changes in the expression pattern. However, the quantity of DEGs alone does not comprehensively capture the transcriptional distinctions between each sex factor, as a significant fraction of DEGs under a particular sex factor could intersect with those from other sex factors, thus not be unique.

To delve deeper into the uniqueness and overlap among sex factor effects beyond merely counting linear model-based DEGs, the intersections of DEGs across all combinations of sex factors were subsequently explored (**Figure 2.4A**). For neurons, astrocytes, oligodendrocyte precursor cells, myelinating oligodendrocytes, and microglia, the largest fraction of DEGs is shared among SCE, GSE, the interaction effect, and normative sex difference. This suggests that different sex factors can drive a substantial part of the similar transcriptional shift in these cell types. Conversely, for tanycytes and vascular leptomeningeal cells, only a small fraction of linear model-based DEGs overlap, implying that the effects of sex factors in these cell types are largely distinct.

In terms of unique sex factor DEGs that are influenced solely by a single sex factor, the largest sex factor specific DEG set in oligodendrocyte precursor cells, microglia, and vascular leptomeningeal cells is SCE. On the other hand, the GSE-specific DEG have the highest number in neurons, ependymal cells, mural pericytes, vascular smooth muscle cells, and tanycytes. Astrocytes, myelinating oligodendrocytes, and endothelial cells harbor the most extensive SCE-GSE interaction-specific DEGs. The DEGs specific to the normative sex difference, XXF vs XYM, are relatively scarce in most cell types, suggesting that the linear model-based SCE, GSE, and SCE-GSE interaction DEGs can account for a substantial part of the normative sex difference.

Transcriptional contributions of individual sex factors to the normative sex difference of linear model based DEGs across cell types

To better assess the contributions of SCE, GSE, and the SCE-GSE interaction to the normative sex difference, we focused on the overlap between the SCE, GSE, and SCE-GSE interaction DEGs with the XXF vs XYM DEGs in each cell type. This allowed us to distinguish GSE-specific, SCE-specific, SCE-GSE interaction-specific contributions, and shared contributions, which reflect the DEGs shared between multiple sex factors, to the normative sex difference (**Figure 2.4C**). On examining the proportion of normative sex differences accounted for by all three sex factors, these sex factors explain over 70% of the normative sex differences in all cell types. Notably, in neurons, astrocytes, tanycytes, endothelial cells, oligodendrocyte progenitor cells, and myelinating oligodendrocytes, these sex factors account for over 85% of the normative sex difference. This affirms the efficacy of our methods in dissecting and explaining a major portion of normative sex differences.

When considering the contribution of each individual sex factor, the GSE-specific contribution is highest in tanycytes, accounting for over 56% of the total normative sex differences. GSE also contributes to over 30% of the normative sex differences in mural cells, including pericytes and vascular smooth muscle cells, and ependymal cells. However, in other cell types the GSE-specific contribution is lower and in astrocytes GSE only contribute to less than 2% of the normative sex differences. The large variability in GSE-specific contributions across different cell types indicates a cell-type-specific effect.

Conversely, the SCE-specific contribution is more consistent in percentage across cell types compared to GSE. SCE-specific contribution is highest in microglias (contributing to 18% of the total normative sex differences) and contribute to 5-10% total normative sex differences in neurons, astrocytes, tanycytes, oligodendrocyte progenitor cells and myelinating oligodendrocytes. Although the SCE-specific contribution is lower than the GSE-specific contribution in tanycytes, mural cells, and ependymal cells, it is higher in neurons, astrocytes, microglia, oligodendrocyte progenitor cells, and myelinating oligodendrocytes. This underscores the important role the SCE-specific effect plays in normative sex differences.

The SCE-GSE interaction-specific contribution is relatively minor, contributing to 4.3% in ependymal cells and less than 2% in all the other cell types. This underscores a relatively small influence of the interaction-specific effect on the transcriptional shift within the normative sex difference context.

The shared contribution accounts for most of the normative sex differences in all cell types, except for tanycytes. This suggests that different sex factors shared a substantial part of similar impacts on transcriptional shifts in normative sex differences.

Transcriptional contributions of individual sex factors to the normative sex difference of linear model based DEGs across neuronal subtypes

To gain a more detailed understanding of the influence of sex factors on neurons, intersections of DEGs across all combinations of sex factors and normative sex differences were evaluated within 15 neuronal subtypes (**Figure 2.5A**). Notably, the largest faction of DEGs in Agrp.Npy, Avp, Ccnd2.Cck, Gal, and Lhx6 neurons was solely under the influence of SCE. In contrast, in Apoe, Nrgn, Avp.Oxt, and Pomc neurons, the largest faction of DEGs was solely under the influence of GSE. These results suggest a potential exaggeration of SCE or GSE effects outside of normative sex differences within these cell types by the four core genotypes

Further examination was conducted on the overlap between SCE, GSE, and SCE-GSE interaction DEGs with the XXF vs XYM DEGs in each neuronal subtype, allowing for an assessment of the individual contributions of SCE, GSE, and SCE-GSE interaction to normative sex differences (**Figure 2.5B**). Upon examination, these three sex factors collectively accounted for 70%-85% of the normative sex differences in all neuronal types. These findings validate the effectiveness of our methodology in deconstructing and explaining the majority of normative sex differences in these neuronal subtypes.

Regarding the specific contributions of each sex factor, the GSE-specific contribution constituted 33% of the total normative sex differences in Avp.Oxt and Pomc neurons. In other neuronal subtypes, GSE-specific contributions were less than 20%. On the other hand, SCE-specific contributions represented 50% of the total normative sex differences in Agrp.Npy neurons and exceeded 20% in Gal, Bdnf, and Pomc neurons. Both SCE and GSE-specific contributions varied considerably across neuronal subtypes, and the importance of the SCE-specific effect is strongly reflected in normative sex differences among neuronal subtypes. Interestingly, the contributions from SCE-GSE interaction DEGs were entirely shared with SCE or GSE in neuronal subtypes, thus adding to the shared contribution. This shared contribution was the highest, compared to GSE and SCE-specific contributions, in Nrgn, Thy1, and Avp neurons, but not in the remaining neuronal subtypes. This suggests that the influence of different sex factors contributing to normative sex differences is more divergent among neuronal subtypes.

Pairwise Comparison Based Differently Expressed Genes of GSE and SCE

For the identification of pairwise DEGs using the Wilcoxon Rank Sum test, both XXF vs XYF and XXM vs XYM comparisons identify the SCE, albeit on distinct gonadal sex backgrounds. Similarly, both XXF vs XXM and XYF vs XYM comparisons identify the

GSE, but on different chromosomal sex backgrounds. The comparison of XXF vs XYM serves to reflect normative sex differences.

Considering the DEG quantities for the two SCE comparisons (**Figure 2.6B**), the XXM vs XYM comparison captures a higher number of DEGs across all cell types in comparison to the XXF vs XYF comparison. In the XXF vs XYF comparison, the top three cell types with the highest DEG counts include astrocytes, neurons, and endothelial cells. Conversely, in the XXM vs XYM comparison, the top three cell types, which have the highest DEG numbers, are neurons, endothelial cells, and ependymal cells. By comparing the cell type-specific DEGs identified in the XXF vs XYF comparison and those in the XXM vs XYM comparisons **(Supplementary Figure 2.1A)**., it is clear that the difference in these two comparisons is not limited to DEG numbers alone, notably, a considerable portion of the DEGs identified in these two SCE comparisons are not shared across each cell type. This suggests that the gonadal male background may amplify the SCE more than the gonadal female background. Moreover, the interactions between the SCE and GSE may contribute to the differences in the DEGs identified for SCE under the two distinct gonadal sex backgrounds. This effect, which influences all cell types in terms of DEG number, also contributes to different cell types in a cell-type-specific manner. For instance, astrocytes exhibit a relatively stronger SCE in the XXF vs XYM comparison compared to other cell types.

In assessing the DEG counts for the two GSE comparisons (**Figure 2.6C**), it is evident that the XYF vs XYM comparison captures strikingly more DEGs across all cell types than the XXF vs XXM comparison. In both comparisons, neurons have the highest DEG numbers. However, in the XYF vs XYM comparison, neurons have 1297 GSE DEGs, while in the XXF vs XXM comparison, the number stands at a mere 89. Additionally, the overlap in DEGs is quite limited between the two comparisons (**Supplementary Figure 2.1B**). This finding suggests that the male sex chromosome background may amplify the GSE more than the female sex chromosome background in a cell-type-specific manner.

In order to more accurately elucidate the distinctiveness and overlap between the two sex factors, SCE and GSE, we combined the DEGs of XXF vs XYF and XXM vs XYM to represent SCE, and combined the DEGs of XYF vs XYM and XXF vs XXM to represent GSE (**Figure 2.6A**). Notably, the most substantial fraction of DEGs is shared among SCE, GSE and normative sex difference in neurons, astrocytes, endothelial cells and myelinating oligodendrocytes but not other cell types. When it comes to unique sex factor DEGs, which are solely influenced by a single sex factor, neurons, oligodendrocyte precursor cells, ependymal cells, Mural Pericytes VSMCs, Endothelial cells, Myelinating Oligodendrocytes, and Tanycytes exhibit the largest GSE-specific DEG set. Conversely, the most significant number of SCE-specific DEGs is found in in astrocytes and microglias.

Transcriptional contributions of GSE and SCE to the normative sex difference of pairwise comparison based DEGs across cell types

We focused on the overlap between the SCE and GSE among the XXF vs XYM DEGs in each cell type to distinguish GSE-specific, SCE-specific, and shared contributions to the normative sex difference (**Figure 2.6 D**). GSE and SCE in the pairwise DEGs together account for over 75% of the normative sex differences in all cell types. Furthermore, in mural cells and myelinating oligodendrocytes, SCE and GSE account for over 85% of the normative sex difference.

The contributions of each sex factor varied across cell types: the GSE-specific contribution was highest in Tanycytes, contributing to 58% of the total normative sex differences, while it was lowest in astrocytes, contributing to 7.4% of the total normative sex differences. The SCE-specific contribution was highest in astrocytes, contributing to 17% of the total normative sex differences, while contributing to 5-10% of the total normative sex differences in most cell types. The shared contribution of SCE and GSE was the highest, compared to GSE and SCE-specific contributions, in astrocytes, neurons, oligodendrocyte progenitor cells, and myelinating oligodendrocytes, but not in the remaining subtypes.

Similar to the linear model-based DEGs, the pairwise DEGs in general cell types show that the effects of the SCE and GSE together, separated with the FCG model, can explain the majority of normative sex differences. Different sex factors share a substantial portion of similar impacts. The GSE-specific contribution is more varied while the SCE-specific contribution is more consistent across cell types. In contrast to the linear model-based comparison, the pairwise comparison tends to identify fewer

DEGs in each comparison and lacks the capacity to evaluate SCE-GSE interactions. Additionally, there is a smaller quantity of cell types whose normative sex differences can be explained beyond 85% when applying the pairwise comparison. It's interesting to note that the GSE effect captured through the pairwise comparison is more pronounced.

Transcriptional contributions of GSE and SCE to the normative sex difference of pairwise comparison based DEGs across neuronal subtypes

When examining the intersection of DEGs across all combinations of sex factors and normative sex differences in 15 neuronal subtypes (**Figure 2.7A**), we observe a limited shared contribution among all sex factors. The greatest proportion of DEGs, observed in Avp, Nrgn, Avp.Oxt, Pomc, Chchd, and Thy 1 neurons, are exclusively influenced by GSE. Furthermore, the number of DEGs affected solely by SCE is relatively small across cell types, which is consistent with the trend that pairwise comparison captures more GSE effect.

Contributions of SCE and GSE to normative sex differences was examined with overlap between SCE, GSE, and the XXF vs XYM DEGs in each neuronal subtype. In Chchd10 neurons, GSE-specific contribution accounts for 53% of normative sex differences, the highest amongst the neuronal subtypes. Across the remaining neuronal subtypes, GSE-specific contribution varied between 6% - 48%. The maximum SCE-specific contribution was observed in Avp.Oxt neurons (37%), and in other neuronal subtypes, this contribution ranged from 3% - 24%. It was noted that in Avp, Avp.Oxt and Chchd10 neurons, SCE and GSE together explained over 85% of the normative sex differences.

However, in Gal and Agrp.Npy neurons, the proportion explained is less than 50%, indicating that the pairwise-based DEGs approach was less effective in capturing the SCE and GSE effects that could account for the majority of normative sex differences in certain neuronal types.

Pathway analysis of genes implicated in Sex Chromosome Effect and Gonadal Sex Effect

To gain insights into the influence of Sex Chromosome Effects (SCE) and Gonadal Sex Effects (GSE) on various biological pathways, an analysis of pathway enrichment was undertaken. The analysis relied on the framework of linear model-based comparisons, due to the capacity of these models to incorporate all four genotypes within a single model. This broadens the scope of DEGs captured and exhibits better performance in explaining normative sex difference in the context of neuronal subtypes compared to the pairwise comparison.

We employed Fisher's exact test to ascertain the overlap between the identified DEGs and the biological pathways catalogued in KEGG, REACTOME, BIOCARTA, and HALLMARK databases[28–31]. To control for multiple testing, we applied the Benjamini-Hochberg method to estimate the FDR. Furthermore, we calculated fold changes based on the average fold change across all overlapping genes within a pathway. Pathways with -log2(fold change) greater than zero indicate an upregulation in sex chromosomal females (XX) compared to sex chromosomal males (XY) for SCE, or an upregulation in gonadal females (F) compared to gonadal males (M) for GSE. We defined the enrichment score as the ratio of overlapping genes to the total genes within our cell type-specific gene set, scaled by 20,000, and then divided by the total genes within the pathway.

Upon scrutinizing the pathway enrichment results from general cell types, a significant number of pathways emerged. These were broadly classified into five functional categories, namely: ATP Generation, Cell Organization, Cell Signaling, Central Dogma, and Immune Response (**Figure 2.8**).

With respect to ATP generation, it was observed that the ATP synthesis by chemiosmotic coupling pathway was upregulated in gonadal females relative to gonadal males in endothelial cells. In neurons, pathways including oxidative phosphorylation, respiratory electron transport, and ATP synthesis by chemiosmotic coupling, were enriched yet exhibited downregulation in sex chromosomal females (XX) relative to sex chromosomal males (XY). A similar trend of downregulation was observed for these pathways in XXF compared to XYM in neurons. This pattern suggests that SCE may have a contributory role in shaping the ATP generation process in the context of normative sex differences in neurons.

When examining pathways connected with cell signaling, varying pathways across diverse cell types were found to be differently influenced under distinct sex factors. In astrocytes mTOR1 signaling and neurotrophin signaling pathways are impacted by SCE. Both pathways were enriched and exhibited downregulation in sex chromosomal females when compared to their male counterparts. mTORC1 signaling, pivotal in modulating cell growth and metabolism in astrocytes, has been implicated in synaptic plasticity and neuronal function regulation[32]. Similarly, neurotrophin signaling in astrocytes, which these cells both produce and receive, promotes neuronal survival and growth while also participating in synaptic plasticity[33].

Within microglia, the TNF-α signaling via NF-κB pathway was found to be enriched and displayed a decrease in activity in sex chromosomal females relative to males. This downregulation was similarly observed in the comparison of XXF to XYM. TNF-α signaling via NF-κB plays a critical role in microglia as a central component of neuroinflammation and neurodegenerative diseases[34,35]. As the primary immune cells within the hypothalamus, microglial activation characterizes neuroinflammatory conditions. The activation of the NF-κB pathway in microglia yields further pro-inflammatory mediators, potentially perpetuating an inflammatory response that may lead to neuronal damage.

In myelinating oligodendrocytes, the ErbB signaling pathway was upregulated in gonadal females compared to males. With ErbB playing a vital role in myelination and neuregulin-activated ErbB2/ErbB3 controlling myelin sheath thickness[36,37], this pathway is essential in myelinating oligodendrocytes. Evidence has pointed to females exhibiting more rapid myelination during development, suggesting that the GSE-influenced ErbB signaling pathway might contribute to these sex differences[36].

Several mRNA metabolism and protein synthesis related pathways were upregulated in endothelial cells in gonadal females, sex chromosomal females, and normative females when compared to males. Contrarily, in neurons, the same pathways exhibited downregulation in gonadal females, sex chromosomal females, and normative females compared to males. This indicates that various sex factors might influence mRNA metabolism and protein synthesis within a single cell type in the same direction, while different cell types may exhibit different directions of regulation.

Biological pathways enriched under SCE and GSE across neuronal subtypes

To delve deeper into the influence of SCE and GSE on diverse biological pathways in different neurons, a similar analysis of pathway enrichment was undertaken for 15 neuronal subtypes. The significantly enriched pathways were classified into seven functional categories: Ion Transportation, Neuronal Activity, ATP Generation, Cell Organization, Cell Signaling, Central Dogma, and Immune Response (**Figure 2.9**).

In neurons, ion channel transport is crucial for the initiation and propagation of electrical signals or action potentials. Notably, voltage-gated potassium channel pathways were found to be upregulated in gonadal and chromosomal females compared to males in Avp, Bdnf, Car10, and Nrgn neurons. Voltage-gated potassium channels, which open in response to alterations in membrane potential, are integral to repolarizing the membrane post an action potential. Ligand-gated ion channel transport pathways demonstrated upregulation in normative females compared to males in Bdnf neurons, in gonadal, chromosomal, and normative females in Car10 neurons, and in gonadal and chromosomal females in Nrgn neurons. These ligand-gated channels, opening in response to neurotransmitter binding, are critical for neurotransmission, facilitating communication between neurons at synapses. Specific to ionotropic glutamate receptors, both NMDA receptor binding and activation pathway and the trafficking of AMPA receptors pathway were found to be upregulated in normative females in Car10 neurons and in gonadal, chromosomal, and normative females in Nrgn neurons. Both receptors are ion channels that allow for the influx of positive ions into the cell upon activation by the neurotransmitter glutamate and can initiate a variety of processes that are crucial for neural function and plasticity[37,38]. These pathway enrichment results suggest a heightened activity in female ion channel transport under both SCE and GSE, providing insights into the sex differences in neuronal ion channel transport.

For other neuronal activities, the long-term potentiation pathway showed a downregulation in both gonadal and chromosomal females and in normative females in Bdnf, Car10, and Nrgn neurons. In contrast, the long-term depression pathway demonstrated an upregulation under the same sex factors in these neuronal subtypes. The observed enrichment directions of these two pathways indicate diminished synaptic strengthening and increased synaptic weakening in hypothalamic neuronal subtypes in females under both SCE and GSE. This aligns with established knowledge that estrogen can modulate Long Term Potentiation (LTP) within specific brain regions and at certain stages of the menstrual cycle[39,40]. The axon guidance pathway, which contributes to synaptic plasticity in the adult brain, was found to be upregulated in chromosomal, gonadal, and normative females in Avp and Bdnf neurons but downregulated in Thy1 neurons in chromosomal and gonadal females, indicating a neuron subtype-specific manner. The enrichment results of these pathways enhance our understanding of sex differences in neuronal plasticity, thereby illuminating sex-specific biological mechanisms.

Disease associated genetic markers enriched in sex factor DEGs

A number of studies has revealed sex differences in the susceptibility to and progression of a wide range of diseases—including Neurodegenerative Disorders, Mental Health Disorders, Cardiometabolic Diseases, and Autoimmune Diseases. These diseases underscore a intersection with brain function and regulation, also within the hypothalamus. The hypothalamus, instrumental in the maintenance of body homeostasis, regulates various physiological processes such as stress responses, the neuroendocrine system, energy balance, appetite, and hormonal secretion via the pituitary gland. It is plausible that sex differentials in hypothalamic function may underpin the observed sex-biased disease susceptibilities.

In order to assess the potential significance of identified sex factor-specific and cell-type specific DEGs within the human disease context, summary statistics from human Genome-Wide Association Studies (GWAS) were collected and analyzed for an array of 71 traits and diseases[16–21] **(Supplementary Table 2.1).** The association of GWAS Single Nucleotide Polymorphisms (SNPs) with specific genes was considered, taking into account genes located within a 50 kilobase radius of each SNP and incorporating hypothalamus-specific expression and splicing Quantitative Trait Loci (eQTL and sQTL, respectively) from the Genotype-Tissue Expression project (GTEX8) for mapping purposes.

The conversion of identified DEGs into their human orthologues was facilitated through the BiomaRt R package. The Marker Set Enrichment Analysis (MSEA) function from the Mergeomics package was subsequently employed to compare the disease association P-values of SNPs linked to the identified DEGs with those linked to a set of random genes. The aim of this comparison was to establish whether the DEGs demonstrated a more robust association than would be expected by chance, as assessed using a chi-squared-like statistic[41].

The MSEA revealed that 34 of the 71 trait and disease GWAS were enriched in at least one sex factor-specific and cell-type-specific DEG set. Three broad categories emerged with significant enrichment: Neuropsychiatric Disorders related GWAS, Obesity-related GWAS, and Type 2 Diabetes-related GWAS. Neurological Disorders related GWAS included GWAS of Schizophrenia, Major Depressive Disorder (MDD), Anxiety, Depressive Symptoms, Anorexia Nervosa, Autism Spectrum Disorder (ASD), and Attention Deficit Hyperactivity Disorder (ADHD). Obesity-related GWAS encompassed GWAS of Body Mass Index (BMI), Body Mass Index in a European population (BMIeur), Waist Circumference (WC), Body Mass Index in women (BMI women), Childhood Obesity, and Hip Circumference adjusted for BMI (HIPadjBMI). Type 2 Diabetes-related GWAS consisted of GWAS of Type 2 Diabetes (T2D), 2-hour Glucose adjusted for BMI (2hrGlucoseBMI), Area Under the Curve for insulin (AUCins), Area Under the Curve for insulin to glucose ratio (AUCinsAUCgluc), Insulin at 30 minutes adjusted for BMI (Ins30BMI), Corrected Insulin Response with Insulin Sensitivity Index (CIRISI), Corrected Insulin Response (CIR), Fasting Proinsulin, Homeostatic Model Assessment for beta cell function (HOMAB), Homeostatic Model Assessment for Insulin Resistance (HOMAIR), Insulin Sensitivity Index based on a Joint Model Analysis (ISIJMA), and Insulin Sensitivity Index adjusted for Age, Sex, and BMI (ISIAgeSexBMI).

Neuropsychiatric disorders associated genetic markers enriched in sex factor DEGs

Among the Neuropsychiatric Disorders category, Schizophrenia was the most enriched GWAS across various cell types and sex factors. Schizophrenia presents distinct sex disparities in both incidence and symptom severity, with males typically exhibiting symptoms earlier than females. The hypothalamic-pituitary-adrenal (HPA) axis, a critical component of the stress response, has been implicated in schizophrenia[10,13]. Notably, while sex factors influenced DEGs in the majority of the general cell types were enriched with schizophrenia GWAS signals, DEG sets of tanycytes and microglias were not. Furthermore, 8 out of 15 neuronal subtypes related to sex factors DEGs were enriched for schizophrenia, including Nrgn, Car10, Avp, Pomc, Gal, Bdnf, Thy1, Chchd10. This might point to cell type and neuronal subtype-specific mechanisms through which the hypothalamus influences sex differences in schizophrenia.

The GWAS of MDD exhibited strong significance in all of GSE, SCE, and normative sex difference-influenced DEGs of Thy1 neurons. It was also enriched in GSE-SCE interaction-influenced DEG sets of microglia and Tac2 neurons. Depressive symptoms GWAS had a broader enrichment. Anxiety was significantly enriched in multiple cell types and sex factors, while in SCE influenced DEGs of Nrgn neurons and normative sex influenced DEGs of Bdnf neurons there was a stronger significance. Women are almost twice as likely as men to suffer from these conditions. Estrogen influences serotonin and other neurotransmitter systems involved in mood regulation[44]. Moreover, sex differences in stress response, partly controlled by the hypothalamus, may also contribute to these differences.

Less broad enrichment was found for ADHD and ASD. ADHD is generally more frequently diagnosed in males than in females, and the symptoms can present differently between sexes, with males often showing more externalizing behaviors (e.g., hyperactivity, impulsivity) and females showing more internalizing behaviors (e.g., inattentiveness, daydreaming) [45]. ADHD GWAS signals were enriched in both SCE influenced DEGs of Gal neurons. Galanin (GAL) is a neuropeptide involved in both stress-related behaviors and responses to drugs of abuse[46]. ASD is diagnosed approximately 4 times more often in males than in females[47]. ASD GWAS signals were enriched in both GSE influenced DEGs of Agrp.Npy neurons and GSE-SCE interaction influenced Avp neurons. Neurons secreting Agouti-related peptide (AgRP) and Neuropeptide Y (NPY) play a role not only in feeding behavior, but also contribute to promoting social interaction in mice[48]. Studies have shown SNPs in AVP signaling are associated with social impairments[49]. These sex factor-influenced neuropeptide systems may contribute to sex differences in ASD and ADHD symptomatology through their influence on social behavior and stress response.

Obesity related GWAS signals enriched in sex factor DEGs

BMI-related GWAS signals exhibited enrichment across multiple cell types and sex factors, with BMIall and BMIeur showing enrichment with a pronounced significance in SCE, GSE and normative sex differences influenced DEG sets in astrocytes and SCE influenced Nrgn neurons. Sex differences are evident in obesity and BMI, with men having a significantly higher BMI than women. Also, obesity patterns differ between sexes with men are more prone to abdominal obesity. The hypothalamus, crucial in regulating energy homeostasis, plays a substantial role in controlling body weight and food intake, thereby influencing BMI and obesity rates. Astrocytes interact closely with neurons in the hypothalamus, and emerging research suggests they might play a role in regulating energy homeostasis. Neurogranin (Nrgn) expressing neurons plays a crucial role in synaptic plasticity. The enriched BMI-related GWAS signals may imply a potential role for astrocytes and Nrgn neurons in sex differences in obesity and BMI through hypothalamic control of energy balance.

Type 2 Diabetes related GWAS signals enriched in sex factor DEGs

Insulin-related GWAS demonstrate enrichment across diverse cell types and sex factors, with variations depending on the specific GWAS. Type 2 Diabetes GWAS exhibit heightened significance in sex factor influenced DEG sets in several cell types and neurons, including Gal neurons DEGs influenced by SCE, Agrp.Npy neurons DEGs influenced by normative sex differences, and Avp.Oxt neurons DEGs influenced by both SCE and normative sex differences. Additionally, ependymal cells demonstrate elevated significance in DEGs influenced by SCE and normative sex differences. Type 2 Diabetes is characterized by insulin resistance and impaired insulin secretion, both of which are complex traits that are influenced by a variety of genetic and environmental factors. The hypothalamus, with its role in regulating energy balance and glucose homeostasis, is a crucial player in the pathogenesis of T2D[50]. Intriguingly, sex differences have been observed in the prevalence and progression of T2D, with men more likely to develop the disease at a lower BMI than women, and women experiencing a greater increase in cardiovascular risk than men once diagnosed. Agrp and Npy neurons in the hypothalamus play pivotal roles in feeding regulation and energy balance, and their altered function could potentially influence T2D pathogenesis. Gal, Avp, and Oxt neurons are related with stress-related behaviors and an altered stress response is suggested to be associated with insulin resistance, a critical factor in T2D development. The sex factor influenced differences in these specific cell types and neuron types, coupled with hypothalamus roles in stress response and energy balance, could underlie sex differences in T2D susceptibility and progression

2.3 Discussion

The distinction between sex chromosomal effects (SCE) and gonadal sex effects (GSE) is an important but understudied area of biological research. SCE refers to the effects arising directly from the genetic material of the X or Y chromosome, whereas GSE are effects resulting from the action of the gonads through sex hormone production and the structural effect of gonads. These two categories of effects can influence a broad range of phenotypes and have traditionally been challenging to tease apart due to their intertwined roles in sexual differentiation. SCE are often understudied because their effects can be obscured by the potent and pervasive influences of gonadal hormones. Consequently, SCE may exert subtle but crucial effects on sex differences that remain largely unexplored. This highlights the need for the Four Core Genotypes mouse model, which enables the separation of these effects for a more nuanced investigation.

The hypothalamus plays a vital role in numerous physiological functions, including thermoregulation, hunger and satiety, and circadian rhythms. As a number of structural and functional sex differences was reported in human and murine hypothalamus at the structural, functional and molecular levels, the detailed mechanisms underlying these sex differences in the hypothalamus are not yet fully understood, leaving a gap in our understanding of the biological basis of sex differences. This study was designed to fill this knowledge gap and shed light on the role of SCE and GSE in hypothalamus.

In this study, we investigated the cell type-specific contributions of SCE and GSE in the hypothalamus using the FCG mouse model. We observed that SCE, GSE, and their interaction account for more than 70% of genetically determined normative sex differences across all hypothalamic cell types and neuronal subtypes. Our findings illustrate a complex interplay of SCE and GSE within diverse cellular pathways, notably those linked to ion transportation, neuronal activity, ATP generation, cell organization, signaling, central dogma, and immune response. This underscores the importance of considering sex-specific genetic and gonadal contributions when studying cell-specific functions and responses in the hypothalamus. Furthermore, our data suggest that these sex differences are not homogenous across cell types but instead manifest in a cell-type specific manner. An intriguing outcome of our analysis is the enrichment of marker set GWAS signals in sex factor-specific and cell type-specific DEGs for neurological disorders, obesity, and type 2 diabetes. These results underscore the potentially profound implications of our findings for understanding the sex-specific susceptibilities and progressions of these prevalent health conditions. Our work echoes the growing recognition in biomedical research that sex differences at the cellular level can contribute significantly to disease risk and phenotype.

Future studies will be necessary to validate and extend our findings. For instance, it would be informative to probe the mechanistic underpinnings of the SCE and GSE effects observed in our study, which could yield new insights into how sex-specific molecular and cellular processes in the hypothalamus contribute to disease risk and progression. Moreover, it will be critical to determine if and how the pathways we identified interact with each other and with external factors such as hormonal regulation, environmental stressors, and age. Furthermore, the translation of these findings to humans represents an exciting avenue for future research, potentially enabling personalized therapeutic strategies based on sex.

2.4 Conclusions

Utilizing the Four Core Genotypes (FCG) mouse model, this study separated the effects of GSE and SCE, allowing for a detailed analysis of their distinct influences at a cellular level in hypothalamus via the application of single-cell RNA sequencing. Remarkably, the analysis in this study identified 11 cell types and 15 neuronal subtypes in hypothalamus. Based on analysis of sex factor specifc and cell type specific DEGs, SCE, GSE, and SCE-GSE interaction account for over 70% of the genetically determined normative sex differences across all hypothalamic cell types and neuronal subtypes. These DEGs were found to be enriched in diverse ion transportation, neuronal activity, ATP generation, cell organization, cell signaling, central dogma, and immune response related pathways in a cell-type specific manner. Moreover, marker set enrichment analysis of GWAS signals in these sex factor specific and DEGs revealed that 34 of the 71 traits and diseases GWAS were enriched in at least one sex factor-specific and cell-type-specific DEG set. Three broad categories emerged with significant enrichment: Neurological Disorders related GWAS, Obesity-related GWAS, and Type 2 Diabetes-related GWAS. Understanding these sex differences in the hypothalamus and their potential implications for disease susceptibility and progression is a crucial area of research. Enhancing the understanding of the key cell types and pathways underlying sex- specific risks is important for enabling personalized therapies based on sex.

2.5 Methods

Experimental Animals and hypothalamus tissue preparation

The FCG mice breeders were from Dr. Arthur P. Arnold's laboratory at UCLA. In C57BL/6J XYM mice, the testis-determining gene Sry is deleted from the Y chromosome, and an Sry transgene is inserted on chromosome 3. By breeding XYM (gonadal and chromosomal male) with C57BL/6J wildtype XXF (gonadal and chromosomal female), four genotypes were produced, namely, XYM, XXF, XYF (chromosomal male, gonadal female), and XXM (chromosomal female, gonadal male). The mice were housed in groups of three to five, with unlimited access to food and water and maintained in a 12-hour dark/light cycle. All animal experiments were approved by the University of California, Los Angeles Institutional Animal Care and Use Committee (IACUC).

Following the protocol described by Brewer et al, the hypothalamus tissue from XXF, XXM, XYF, and XYM mice was freshly dissected and digested with papain. The resulting suspension was adjusted to a final concentration of 100 cells/μl in 0.01% BSA-PBS.

scRNA-seq library preparation and sequencing for scRNA-seq

Barcoded single cells and cDNA libraries were generated using the Drop-seq protocol V 3.1 and Macosko et al's protocol. A concentration of 100 cells/μl was used to prepare single cell suspensions which were co-flowed with EvaGreen droplet generation oil and ChemGenes barcoded microparticles through a FlowJEM aquapel-treated Drop-seq microfluidic device. The recommended flow speeds for oil, cells, and beads were used

(15,000 µl/hr, 4000 µl/hr, and 4000 µl/hr, respectively), resulting in the generation of STAMPs (single-cell transcriptomes attached to microparticles).

Library quality, average size, and concentration were checked using a TapeStation high sensitivity chip. Tagmentation was then performed using the Nextera DNA Library Preparation kit and multiplex indices were added. The molar concentration of the Drop-seq libraries was quantified using Qubit Fluorometric Quantitation and the library fragment length was estimated using a TapeStation.

Sequencing was carried out on an Illumina HiSeq 4000 instrument, with a sequencing depth of 31,000-34,000 reads per cell.

scRNA-seq data pre-processing and quality control

The Drop-seq sequencing data fastq files were pre-processed using Drop-seq tools version 1.12 and aligned to the mouse reference genome mm10 using STAR-2.5.0c after converting the cleaned reads back to fastq format. Default parameters were followed as specified in Drop-seq alignment cookbook v1.2. To assess the quality of the Chemgenes beads batch, the DetectBeadSynthesisErrors function was employed, which estimated a bead synthesis error rate within the acceptable range (<10%). Single cells were distinguished from background noise by imposing a threshold of at least 500 genes and 900 transcripts, with mitochondrial reads making up no more than 20% of the total reads.

Cell clustering and cell type identification

The Cell clustering and cell type identification were performed using the Seurat R package version 4.0.2. The Louvain algorithm was employed to determine cell clusters based on similarities in transcriptome patterns, and the resulting clusters were visualized using t-Distributed Stochastic Neighbor Embedding (t-SNE) and Uniform Manifold Approximation and Projection (UMAP). Highly variable genes selected using the FindVariableFeatures function with default parameters were subjected to principle component analysis (PCA). The number of Principal Components used for Louvain clustering and subsequent visualization was determined with the Jackstraw permutation approach (n=25 for clustering of all cells and n=15 for neuronal cell sub-clustering). Cell type identities of the clusters were resolved by comparing the cell cluster-specific marker genes expressed in each cluster in our own dataset, identified with a Wilcoxon rank sum test, with known cell-type-specific markers curated from literature, single-cell atlases, and previous studies in the hypothalamus and other brain regions. For a gene to be considered in the cell cluster marker analysis, it had to be expressed in at least 10% of the single cells from the cluster of interest and exhibit at least a 0.25 log-fold change in the cell cluster of interest compared to other cells. Multiple testing was corrected using the Benjamini-Hochberg method to estimate the false discovery rate (FDR). Neuronal subtypes were named with hypothalamic peptide genes that the cluster expressed and/or other cluster-specific marker genes.

Identification of differentially expressed genes (DEGs) and pathways

To determine which genes were affected by SCE and/or GSE, we performed both linear model based DEG analysis and pairwise DEG analysis. Linear model based DEGs were identified using the Limma R package, which utilized the model Y = A1SCE + A2GSE + A12SCEGSE, while pairwise DEGs were identified using the built-in "FindMarkers" function in Seurat V4.0.2.

To be considered a DEG, a gene needed to be expressed in at least 10% of the cells from the cell type and exhibit at least a 1.1-fold change in gene expression between the comparison. The Benjamini-Hochberg method was employed to correct for multiple testing and estimate the false discovery rate (FDR) for both linear model based DEGs and pairwise DEGs.

To assess pathway enrichment, we performed Fisher's exact test to determine the overlap between the DEGs and pathways from KEGG, REACTOME, BIOCARTA, and HALLMARK. Multiple testing correction was performed using the Benjamini-Hochberg method to estimate FDR. The enrichment score was calculated as the number of overlapped genes divided by the number of genes in our cell type-specific gene set, multiplied by 20,000 and then divided by the total number of genes in the pathway.

Disease Enrichment Analysis

To evaluate the potential significance of the identified sex-specific differentially expressed genes (DEGs) in human disease context, summary statistics from human

Genome-Wide Association Studies (GWAS) were assembled for a compilation of 71 traits and diseases. The association of GWAS Single Nucleotide Polymorphisms (SNPs) with specific genes was considered, taking into account genes located within a 50 kilobase radius of each SNP and incorporating hypothalamus-specific expression and splicing Quantitative Trait Loci (eQTL and sQTL, respectively) from the Genotype-Tissue Expression project (GTEX8) for mapping purposes. The conversion of the identified DEGs into their human orthologues was facilitated through the BiomaRt R package. Subsequently, the Marker Set Enrichment Analysis (MSEA) function from the Mergeomics package was applied to compare the disease association P-values of SNPs linked to the identified DEGs with those linked to a set of random genes. This was performed to ascertain if a more robust association than would be expected by chance was demonstrated by the DEGs, as assessed using a chi-squared-like statistic.

2.6 Figures

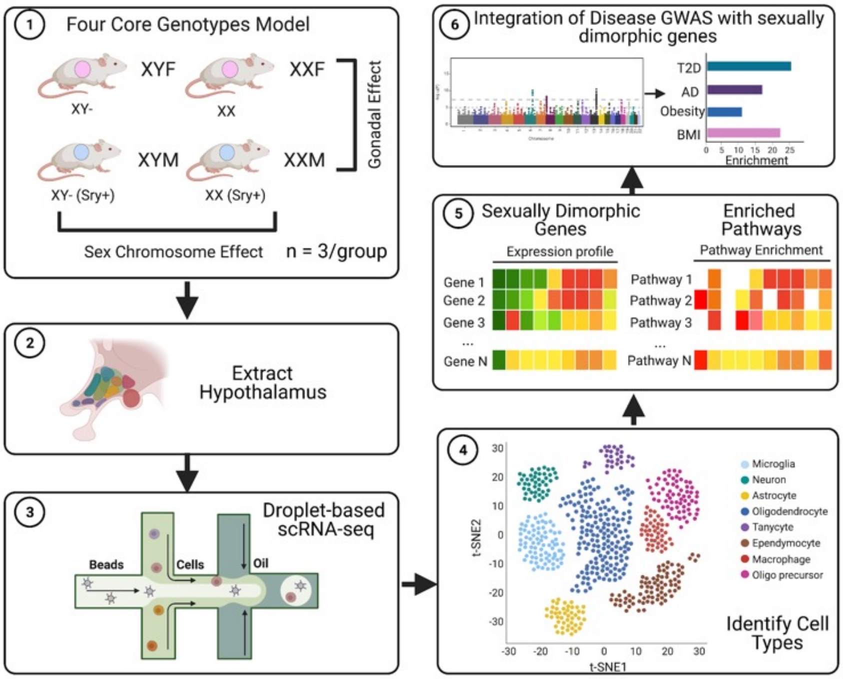

Fig 2. The work flow of examining cell-type specific gonadal sex effect and sex chromosome effect in hypothalamus with four core genotype model

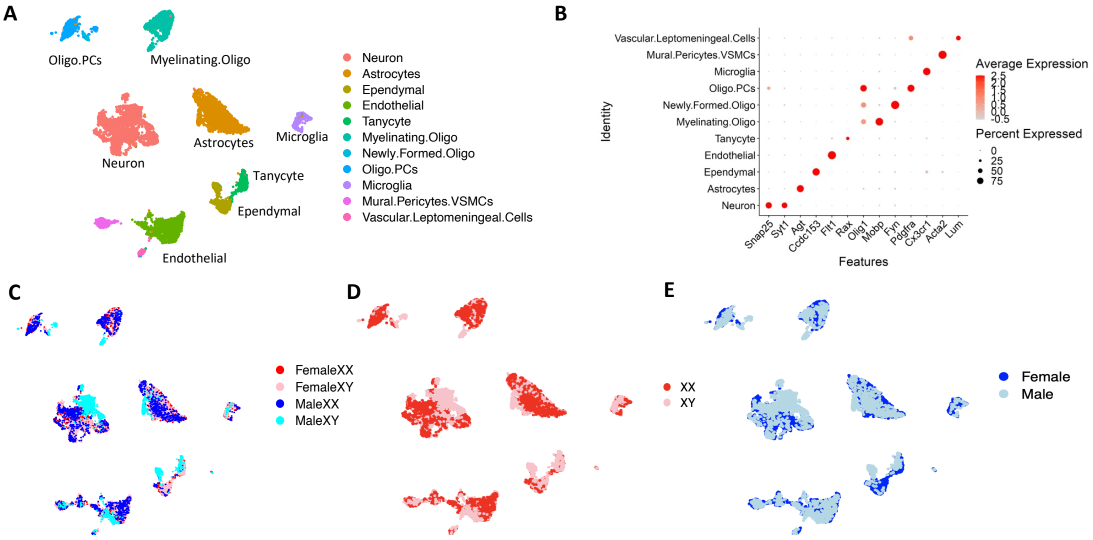

Fig 2. 1 Eleven cell types identified in hypothalamus

A, Uniform Manifold Approximation and Projection (UMAP) plot illustrates the 11 cell types clustered in hypothalamus cells. Each colored dot signifies a cell, with distinct colors indicating various cell types. The Louvain algorithm was utilized to determine cell clusters.

B, Cluster-specific expression of known cell markers: Neurons: Snap25 and Syt1, Astrocytes: Agt, Ependymal cells: Ccdc153, Endothelial cells: Flt1, Tanycytes: Rax, Myelinating Oligodendrocytes: Olig1 and Mobp, Newly Formed Oligodendrocytes: Olig1 and Fyn, Oligodendrocyte Progenitor Cells: Olig1 and Pdgfra, Microglia: Cx3cr1, Mural cells including pericytes and vascular smooth muscle cells: Acta2, and vascular leptomeningeal cells: Lum.

C, UMAP plot showing expression pattern differences between Four Core Genotypes.

D, UMAP plot showing expression pattern differences between hypothalamus cells with sex chromosomal female (XX) and sex chromosomal male (XY).

E, UMAP plot showing expression pattern differences between gonadal female and gonadal male.

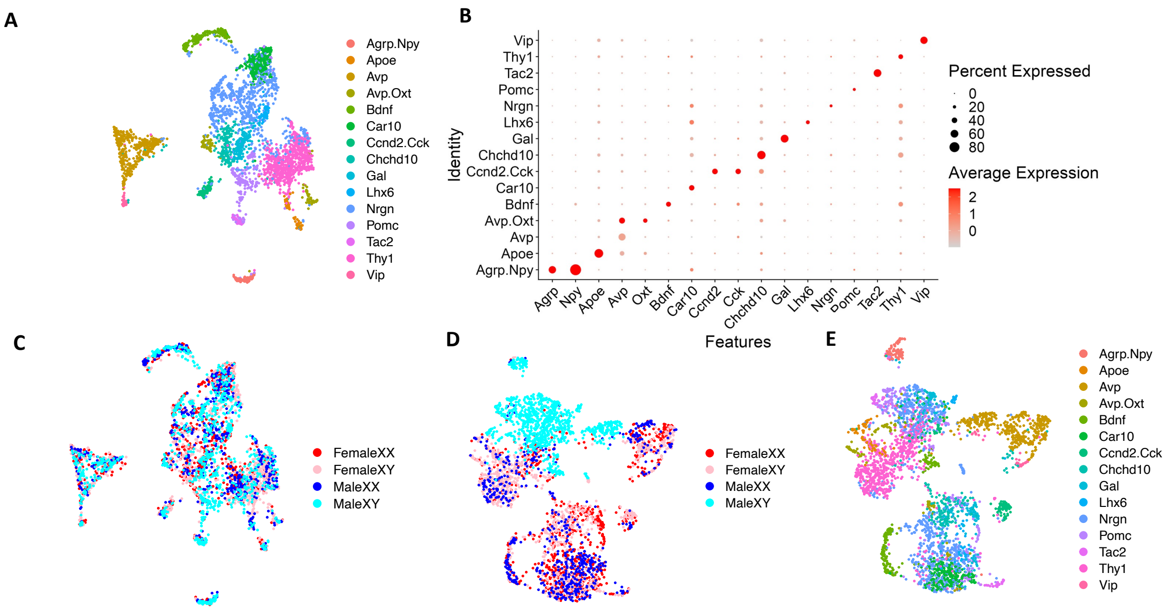

Fig 2. 2 Fifteen neuronal subtypes identified in hypothalamus neurons

A, UMAP plot presenting the integrated clustering of 15 neuronal subtypes across four core genotypes. Here the clusters were derived from an integrated gene expression matrix, which was created by identifying and using "anchors" to correct across the four core genotypes. Each dot represents a single cell, with different colors marking distinct neuronal subtypes. This analysis allows for the identification of common neuronal subtypes across four core genotypes.

B, Neuronal subtypes were named with hypothalamic peptide genes that the cluster expressed and/or other cluster-specific marker genes.

C, D, UMAP plot showing expression pattern differences between Four Core Genotypes based on integrated gene expression matrix (**C**) or non-integrated gene expression matrix (**D**), with the latter reflecting the expression pattern between groups as it was originally measured

E, UMAP plot showing of 15 neuronal subtypes on clustering based on non-integrateed gene expression matrix.

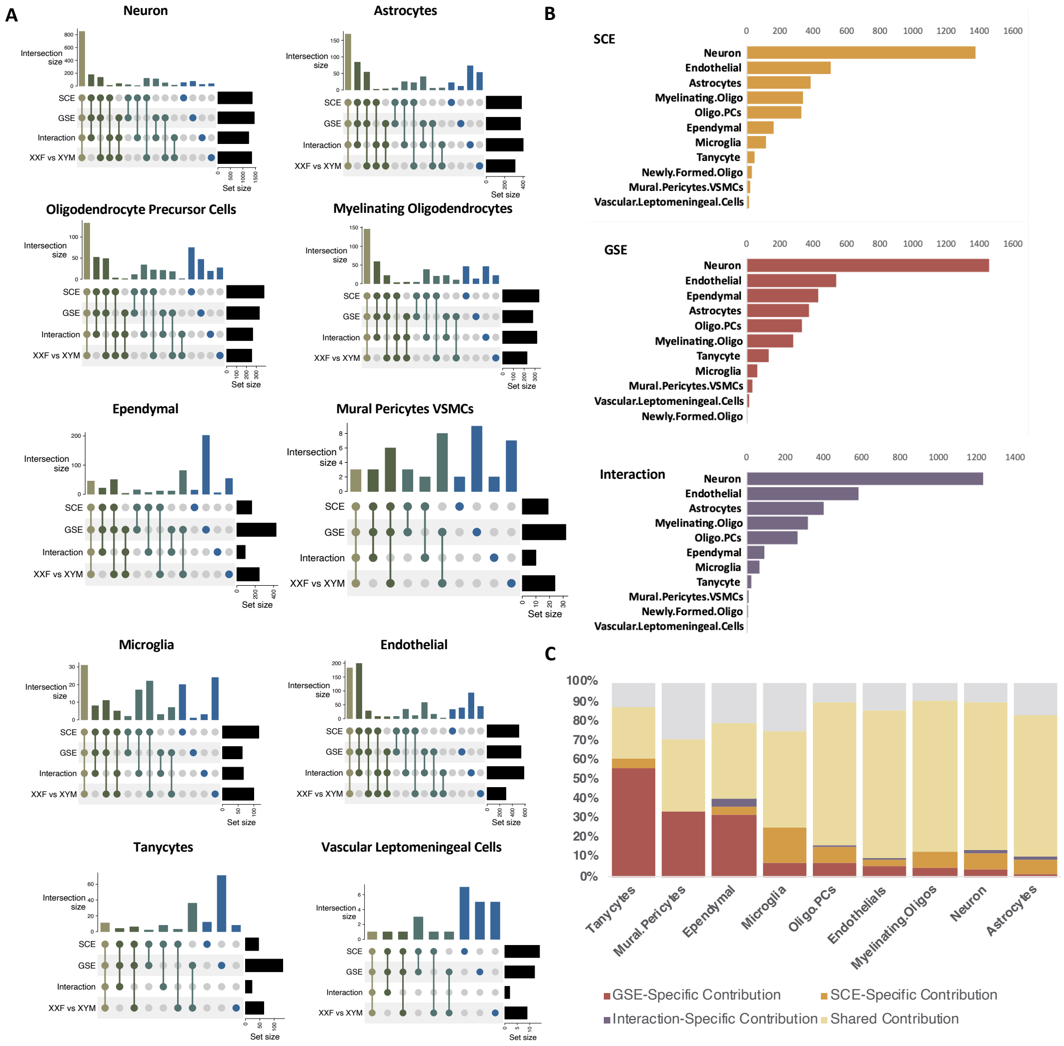

Fig 2. 3 Differently expressed genes detected by linear model based method across cell types

A, UpSet plot illustrating intersections of differentially expressed genes (DEGs) under the influence of 4 sex factors (SCE, GSE, SCE-GSE Interaction and normative sex difference: XXF vs XYM) within each cell type, all at a Bonferroni-adjusted p-value < 0.05. Horizontal bars (set size) indicate total DEGs for each cluster in each plot. In the upset plots, dots point to the specific clusters for which the vertical bars for DEG counts are shown, and vertical lines between dots represent the intersections between two or more clusters.

B, Bar Plot showing DEG numbers under the influence of SCE, GSE and SCE-GSE Interaction across each cell type

C, Stacked bar plot depicting the individual contributions of SCE, GSE, and SCE-GSE interaction to normative sex differences in each cell type, based on overlapping DEGs between SCE, GSE, and SCE-GSE interaction DEGs with the DEGs from XXF vs XYM.

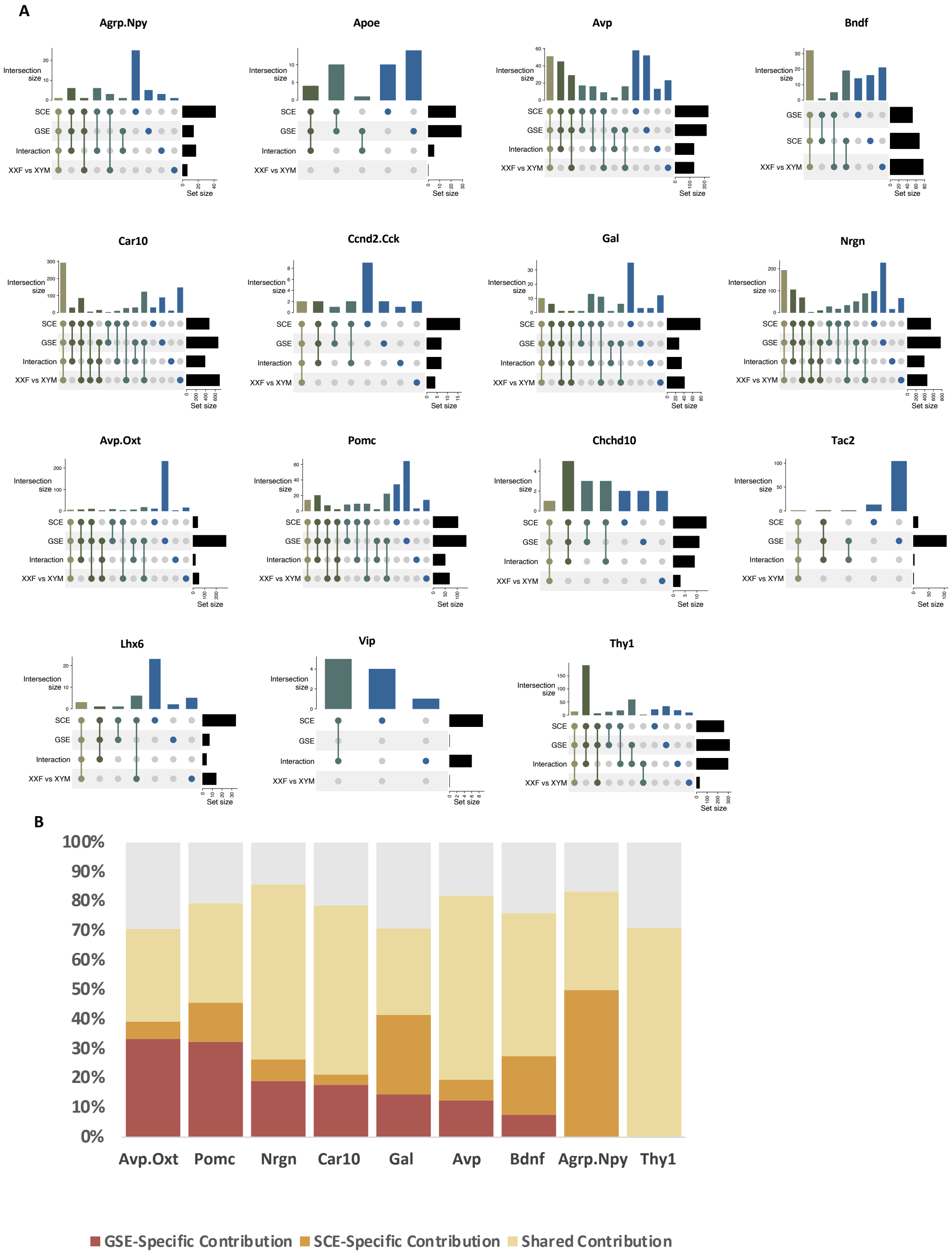

Fig 2. 4 Differently expressed genes detected by linear model based method across neuronal subtypes

A, UpSet plot illustrating intersections of differentially expressed genes (DEGs) under the influence of 4 sex factors (SCE, GSE, SCE-GSE Interaction and normative sex difference: XXF vs XYM) within each neuronal subtype, all at a Bonferroni-adjusted p-value < 0.05. Horizontal bars (set size) indicate total DEGs for each cluster in each plot. In the upset plots, dots point to the specific clusters for which the vertical bars for DEG counts are shown, and vertical lines between dots represent the intersections between two or more clusters.

B, Stacked bar plot depicting the individual contributions of SCE, GSE, and SCE-GSE interaction to normative sex differences in each neuronal subtype, based on overlapping DEGs between SCE, GSE, and SCE-GSE interaction DEGs with the DEGs from XXF vs XYM.

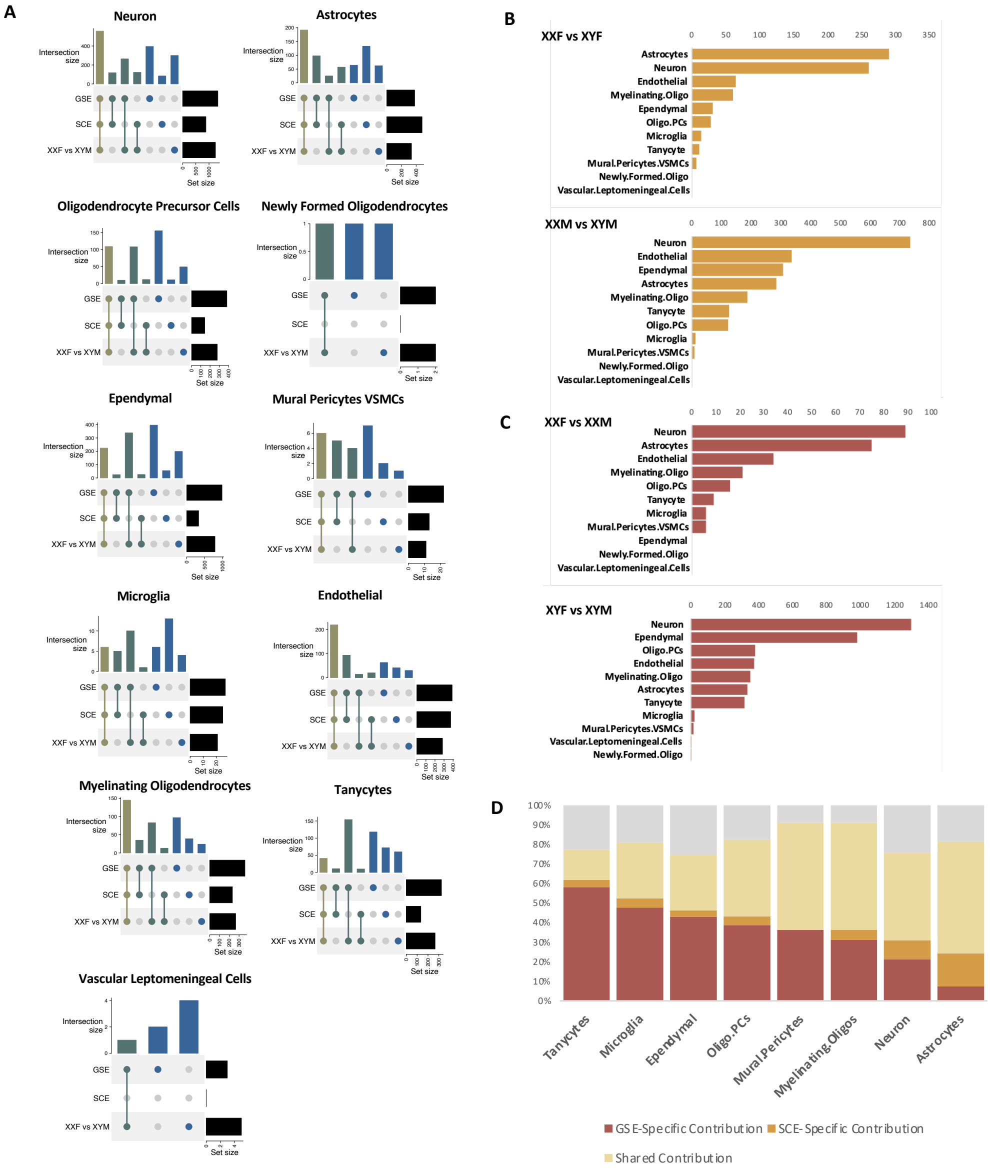

Fig 2. 5 Differently expressed genes detected by pairwise comparison across cell types

A, UpSet plot illustrating intersections of DEGs under the influence of 3 sex factors (SCE, GSE, and normative sex difference: XXF vs XYM) within each cell type. SCE DEGs are union of XXF vs XYF DEGs and XXM vs XYM DEGs while GSE DEGs are union of XXF vs XXM DEGs and XYF vs XYM DEGs all at a Bonferroni-adjusted p-value < 0.05. Horizontal bars (set size) indicate total DEGs for each cluster in each plot.

In the upset plots, dots point to the specific clusters for which the vertical bars for DEG counts are shown, and vertical lines between dots represent the intersections between two or more clusters.

B, Bar Plot showing SCE influenced DEG numbers captured in two separate comparisons: XXF vs XYF and XXM vs XYM

C, Bar Plot showing GSE influenced DEG numbers captured in two separate comparisons: XXF vs XXM and XYF vs XYM

D, Stacked bar plot depicting the individual contributions of SCE, GSE, and SCE-GSE interaction to normative sex differences in each cell type, based on overlapping DEGs between SCE, GSE, and SCE-GSE interaction DEGs with the DEGs from XXF vs XYM.

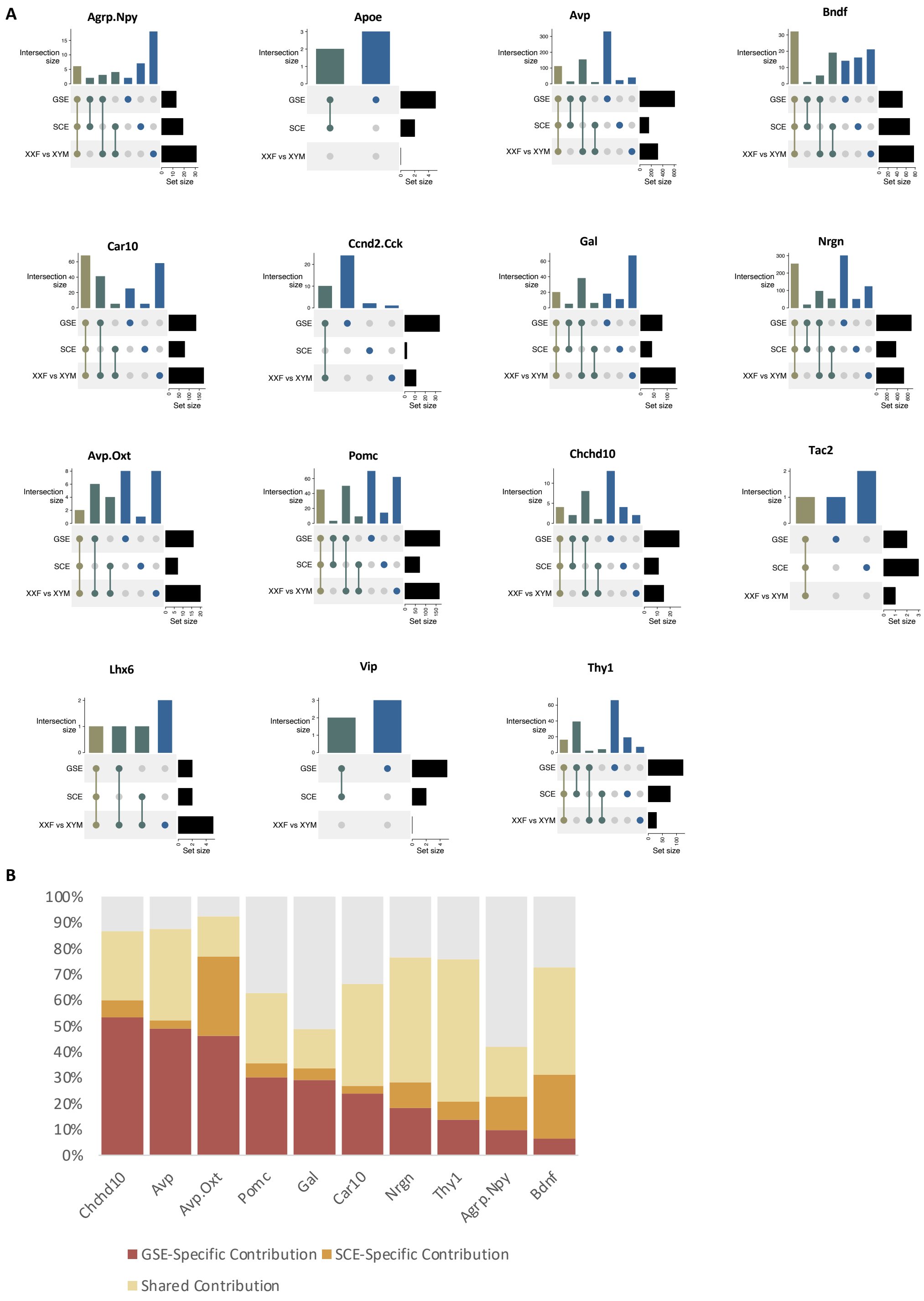

Fig 2. 6 Differently expressed genes detected by pairwise comparison across neuronal subtypes

A, UpSet plot illustrating intersections of DEGs under the influence of 3 sex factors (SCE, GSE, and normative sex difference: XXF vs XYM) within each cell type. SCE

DEGs are union of XXF vs XYF DEGs and XXM vs XYM DEGs while GSE DEGs are union of XXF vs XXM DEGs and XYF vs XYM DEGs all at a Bonferroni-adjusted p-value < 0.05. Horizontal bars (set size) indicate total DEGs for each neuronal subtype in each plot. In the upset plots, dots point to the specific clusters for which the vertical bars for DEG counts are shown, and vertical lines between dots represent the intersections between two or more clusters.

D, Stacked bar plot depicting the individual contributions of SCE, GSE, and SCE-GSE interaction to normative sex differences in each neuronal subtype, based on overlapping DEGs between SCE, GSE, and SCE-GSE interaction DEGs with the DEGs from XXF vs XYM.

Fig 2. 7 Pathways enriched in cell type specific DEGs affected by SCE , GSE and normative sex differences

Dot Plot visualizing the significant pathways that are enriched within the sex factor-specific and cell type-specific DEG sets, considering all pathways at a Bonferroni-adjusted p-value < 0.05. The horizontal axis denotes the cell type-specific DEG set impacted by SCE, GSE, and normative sex differences. On the vertical axis, individual pathway names are displayed on the left, with pathway categories on the right. The size of each dot corresponds to the enrichment score for each pathway, reflecting the ratio of overlapping genes to total genes within the cell type-specific gene set, adjusted by a scale factor of 20,000, and then divided by the total number of genes within the pathway. Dot color represents the log2(fold change), calculated based on the average fold change across all overlapping genes within a pathway. Pathways exhibiting a log2(fold change) greater than zero signify an upregulation in SCE-influenced XX individuals relative to XY individuals, or in GSE-influenced females as compared to males.

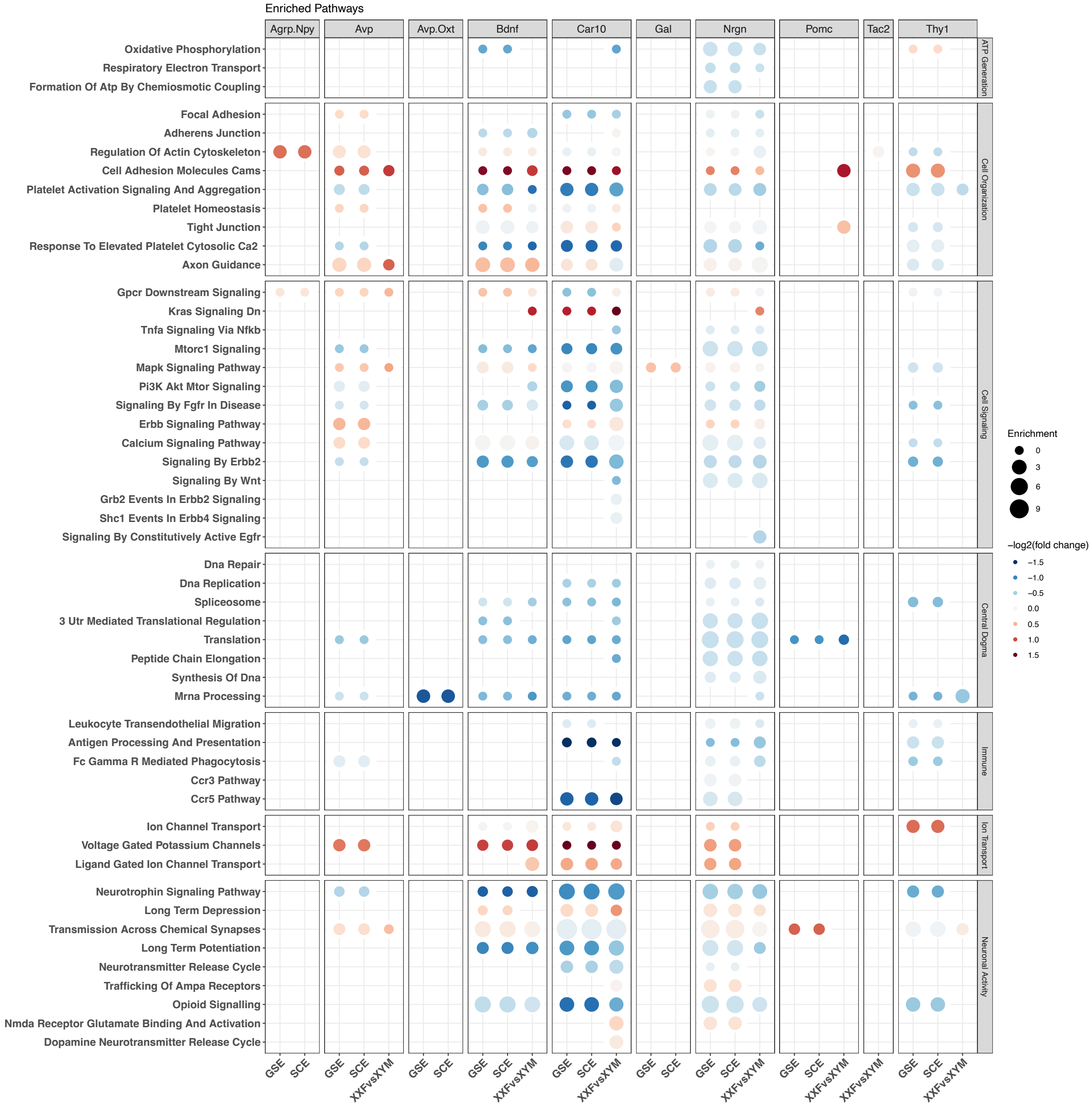

Fig 2. 8 Pathways enriched in neuronal subtype specific DEGs affected by SCE, GSE and normative sex differences

Dot Plot visualizing the significant pathways that are enriched within the sex factor-specific and neuronal subtype specific DEG sets, considering all pathways at a Bonferroni-adjusted p-value < 0.05. The horizontal axis denotes the neuronal subtype specific DEG set impacted by SCE, GSE, and normative sex differences. On the vertical axis, individual pathway names are displayed on the left, with pathway categories on the right. The size of each dot corresponds to the enrichment score for each pathway, reflecting the ratio of overlapping genes to total genes within the cell type-specific gene set, adjusted by a scale factor of 20,000, and then divided by the total number of genes within the pathway. Dot color represents the log2(fold change), calculated based on the average fold change across all overlapping genes within a pathway. Pathways exhibiting a log2(fold change) greater than zero signify an upregulation in SCE-influenced XX individuals relative to XY individuals, or in GSE-influenced females as compared to males.

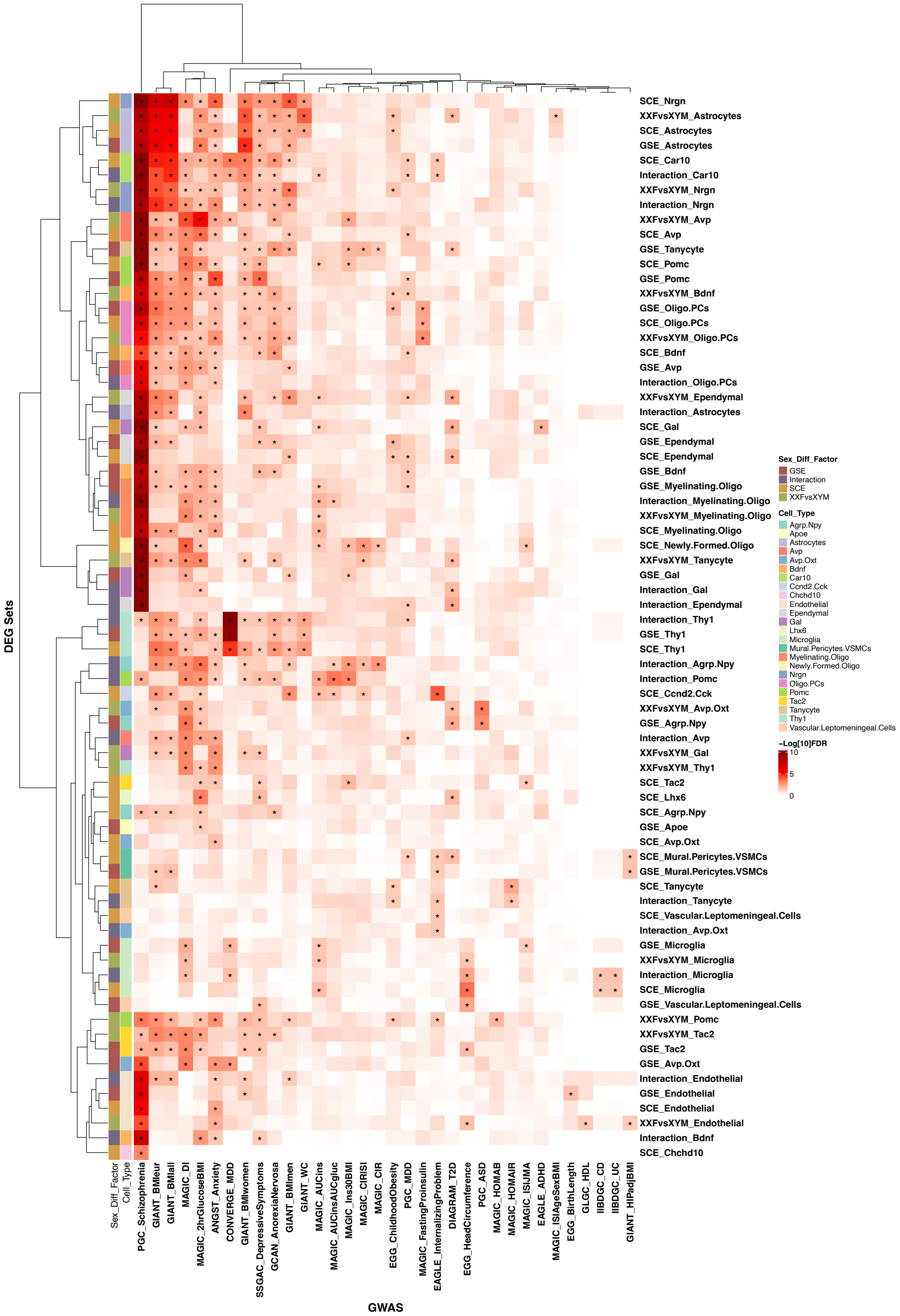

Fig 2. 9 **Sexual dimorphic genes associate with diseases or phenotype GWAS at cell type level**

Heatmap visualizing the GWAS that are enriched within the sex factor-specific and cell type specific DEG sets. The vertical axis signifies DEG sets, specific to cell types, influenced by SCE, GSE, SCE-GSE interaction, and normative sex differences. The horizontal axis represents distinct GWAS. The color within each cell depicts the -log10(FDR), measured using a chi-square-like metric. Cells demonstrating a FDR < 0.05 are highlighted with *.

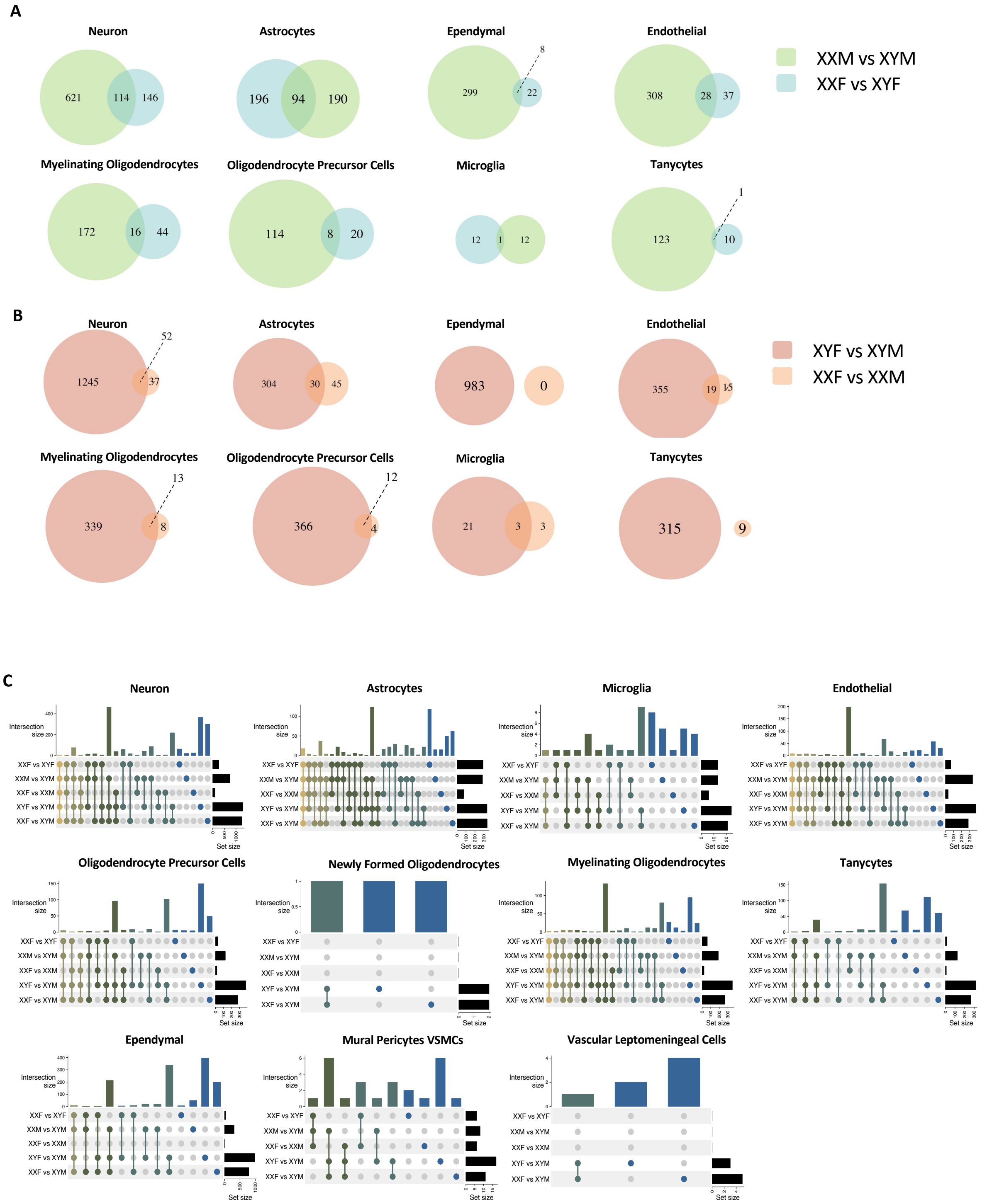

Sup Fig. 2. 1 Intersections of DEGs under pairwise comparison

A, Vein plot showing intersection of DEGs from XXF vs XYF and XXM vs XYM comparisons. Both comparisons infer DEGs influenced by SCE

B, Vein plot showing intersection of DEGs from XXF vs XXM and XYF vs XYM comparisons. Both comparisons infer DEGs influenced by GSE

C, UpSet plot illustrating intersections of DEGs in 5 pairwise comparisons (XXF vs XYF, XXM vs XYM, XXF vs XXM, XYF vs XYM, XXF vs XYM) within each cell type all at a Bonferroni-adjusted p-value < 0.05. Horizontal bars (set size) indicate total DEGs for each cluster in each plot. In the upset plots, dots point to the specific clusters for which the vertical bars for DEG counts are shown, and vertical lines between dots represent the intersections between two or more clusters.

2.7 Tables

GWAS abbreviation	GWAS database	GWAS disease or phenotype name
ADIPOGen_Adiponectin	ADIPOGen	Adiponectin levels
AMDGene_AdvancedAMD	AMDGene	Advanced Age-related Macular Degeneration
AMDGene_GeographicAtrophy	AMDGene	Geographic Atrophy
AMDGene_NeovascularDisease	AMDGene	Neovascular Disease
ANGST_Anxiety	ANGST	Anxiety
CARDIOGRAM_CAD	CARDIOGRAM	Coronary Artery Disease
CONVERGE_MDD	CONVERGE	Major Depressive Disorder
DIAGRAM_T2D	DIAGRAM	Type 2 Diabetes
EAGLE_ADHD	EAGLE	Attention Deficit Hyperactivity Disorder
EAGLE_Aggression	EAGLE	Aggression
EAGLE_InternalizingProblem	EAGLE	Internalizing Problem
EAGLE_SleepBMIadj	EAGLE	Sleep (BMI Adjusted)
EGG_BirthLength	EGG	Birth Length
EGG_BirthWeight	EGG	Birth Weight
EGG_ChildhoodBMI	EGG	Childhood Body Mass Index
EGG_ChildhoodObesity	EGG	Childhood Obesity
EGG_EarlyGrowth	EGG	Early Growth
EGG_HeadCircumference	EGG	Head Circumference
EGG_LateGrowth	EGG	Late Growth
EGG_TannerStage	EGG	Tanner Stage
EGG_TotalGrowth	EGG	Total Growth
GCAN_AnorexiaNervosa	GCAN	Anorexia Nervosa
GIANT_BMIall	GIANT	Body Mass Index (all)
GIANT_BMIeur	GIANT	Body Mass Index (European ancestry)
GIANT_BMImen	GIANT	Body Mass Index (men)
GIANT_BMIwomen	GIANT	Body Mass Index (women)
GIANT_Height	GIANT	Height
GIANT_HIP	GIANT	Hip Circumference
GIANT_HIPadjBMI	GIANT	Hip Circumference (BMI Adjusted)
GIANT_WC	GIANT	Waist Circumference
GIANT_WCadjBMI	GIANT	Waist Circumference (BMI Adjusted)
GIANT_WHR	GIANT	Waist-Hip Ratio
GIANT_WHRadjBMI	GIANT	Waist-Hip Ratio (BMI Adjusted)
GLGC_HDL	GLGC	High-Density Lipoprotein
GLGC_LDL	GLGC	Low-Density Lipoprotein
GLGC_TC	GLGC	Total Cholesterol
GLGC_TG	GLGC	Triglycerides
GUGC_Gout	GUGC	Gout
GUGC_UA	GUGC	Uric Acid levels
IGAP_AlzheimerDisease	IGAP	Alzheimer's Disease
IIBDGC_CD	IIBDGC	Crohn's Disease
IIBDGC_IBD	IIBDGC	Inflammatory Bowel Disease
IIBDGC_UC	IIBDGC	Ulcerative Colitis
MAGIC_2hrGlucoseBMI	MAGIC	Two-hour Glucose (BMI Adjusted)
MAGIC_AUCins	MAGIC	Area Under the Curve for Insulin
MAGIC_AUCinsAUCgluc	MAGIC	Ratio of Area Under the Curve for Insulin and Glucose
MAGIC_CIR	MAGIC	Corrected Insulin Response
MAGIC_CIRISI	MAGIC	Corrected Insulin Response and Insulin Sensitivity Index
MAGIC_DI	MAGIC	Disposition Index
MAGIC_FastingGlucoseInteraction	MAGIC	Fasting Glucose (Interaction Effect)
MAGIC_FastingGlucoseMain	MAGIC	Fasting Glucose (Main Effect)
MAGIC_FastingInsulinInteraction	MAGIC	Fasting Insulin (Interaction Effect)
MAGIC_FastingInsulinMain	MAGIC	Fasting Insulin (Main Effect)
MAGIC_FastingProinsulin	MAGIC	Fasting Proinsulin levels
MAGIC_HbA1C	MAGIC	Hemoglobin A1C levels
MAGIC_HOMAB	MAGIC	Homeostatic Model Assessment for Beta-cell function
MAGIC_HOMAIR	MAGIC	Homeostatic Model Assessment for Insulin Resistance
MAGIC_Incr30	MAGIC	Incremental Insulin Response at 30 minutes
MAGIC_Ins30	MAGIC	Insulin level at 30 minutes
MAGIC_Ins30BMI	MAGIC	Insulin level at 30 minutes (BMI Adjusted)
MAGIC_ISIAgeSexBMI	MAGIC	Insulin Sensitivity Index (Age, Sex, and BMI Adjusted)
MAGIC_ISIAgeSexOnly	MAGIC	Insulin Sensitivity Index (Age and Sex Only Adjusted)
MAGIC_ISIJMA	MAGIC	Insulin Sensitivity Index (Joint Meta-Analysis)
PGC_ASD	PGC	Autism Spectrum Disorder
PGC_BIP	PGC	Bipolar Disorder
PGC_MDD	PGC	Major Depressive Disorder
PGC_Schizophrenia	PGC	Schizophrenia
ReproGen_AgeAtMenarche	ReproGen	Age at Menarche
SSGAC_DepressiveSymptoms	SSGAC	Depressive Symptoms
SSGAC_Neuroticism	SSGAC	Neuroticism
SSGAC_SubjectiveWellbeing	SSGAC	Subjective Well-being.

Table 2. 1 Human GWAS of 71 traits and diseases from 16 consortiums used in

marker set enrichment analysis (MSEA)

Chapter 3. Characterizing the effect of aging in mice visceral WAT

3.1 Introduction

On average, at an equivalent BMI, older adults have more body fat (white adipose tissue, WAT) than younger adults, especially in the visceral (abdominal) area [51,52]. This is partially due to the progressive decline in skeletal muscle mass with age. These age-related alterations in body composition are defined as sarcopenic obesity [53,54]. Visceral adiposity accelerates aging by promoting insulin resistance, cardiovascular dysfunction, and many other chronic diseases, significantly shortening health span [55,56]. Thus, preventing or reducing WAT accumulation is critical for healthy aging. A recent study shows that older individuals have reduced energy expenditure, indicating a global remodeling of tissue metabolism during aging[57]. Unfortunately, the cellular mechanism of age-related visceral WAT accumulation is still poorly understood.

WAT regulates numerous hormonal and metabolic processes, and exhibits compositional and phenotypic plasticity[58]. WAT expands via adipocyte hypertrophy (cell enlargement) or adipogenesis (the generation of new adipocytes). We and others generated multiple mouse models that allow *in vivo* tracking of adipogenesis, and showed that the adipogenesis rate is very low in young adult mice [59-61], similar to that in young adult humans [62]. During aging, it is known that adipocytes undergo hypertrophy

[63], but it remains unclear if WAT also expands through adipogenesis, which would grant WAT an “unlimited” potential to grow.

Adipocyte progenitor cells (APCs), located within the WAT stroma, are a heterogeneous group of mesenchymal stem cells, including adipocyte stem cells and committed progenitor cells[58]. Adipogenesis involves two steps, the proliferation of APCs and the differentiation of APCs into mature adipocytes. APCs express a set of mesenchymal stem cell surface markers, such as Pdgfrα, Pdgfrβ, CD29, CD34, and Sca1[64]. Recently, scRNA-seq has provided unprecedented opportunities to define the heterogeneity of murine and human APCs[65-71], revealing new subtypes and dynamics under various pathophysiological conditions.

In this study, we employed an adipocyte-specific lineage tracing system and found the first cellular evidence that WAT expands with age through massive adipogenesis. Thus, unexpectedly, in contrast to most adult stem cells that exhibit a reduced ability to proliferate and differentiate[72-74], adipogenesis of APCs is unlocked by aging. These newly generated and pre-existing adipocytes are similar in size , and all these cells are larger than adipocytes in young adults, confirming age-related adipocyte hypertrophy and hyperplasia. Through a series of *in vivo* transplantations of adipose tissue and 3D imaging of the transplants, we showed that the APCs in aged mice cell-autonomously gain high adipogenic capacity. scRNA-seq analysis revealed a global transformation of APCs in aged mice and older humans and uncovered a new APC population that is enriched during aging. This new type of APC displays high proliferation and adipogenesis capacity, both *in vivo* and *in vitro*. Leukemia Inhibitory Factor Receptor (LIFR), one of the top markers of this new APC population is critical for the adipogenic potential of such population. These findings provide new insights into the cellular mechanism of age-related adiposity.

3.2 Results

Age-related WAT expansion in mice mimics age-related obesity in humans

As mice age, both males and females showed a gradual increase of bodyweight, and the bodyweight gain was much higher in males than females (**Supplementary Fig.3. 1a-c**). As male mice gained more weight than female mice, we focused on males in this study. The age-related body weight gain in male mice was primarily attributed to gain of WAT, as the percentage of fat mass increased >6-fold during aging (**Supplementary Fig.3.1d**), while the percentage of lean mass decreased ~23% (**Supplementary Fig.3.1e**). Total body water content was also decreased with age (**Supplementary Fig.3.1f**). Among the two types of fat depots, gonadal WAT (gWAT), a typical type of visceral WAT, had the most significant weight gain with age (4.6-fold) (**Supplementary Fig.3.1g**), while subcutaneous WAT (sWAT) increased 2.8-fold (**Supplementary Fig.3.1h**). The aged mice exhibited dramatically reduced oxygen consumption (**Supplementary Fig.3.1i**), slightly reduced physical activity (**Supplementary Fig.3.1j**), and dramatically reduced energy expenditure (**Supplementary Fig.3.1k**). Total movements were not significantly altered (**Supplementary Fig.3.1l**), and food intake was reduced in aged mice (**Supplementary Fig.3.1m**). The drop in oxygen consumption and energy expenditure suggested that the aged mice have significantly lower basal metabolism, similar to humans[57]. Intraperitoneal glucose tolerance tests (GTT) (**Supplementary Fig.3.1n,o**) and insulin tolerance tests (ITT) (**Supplementary Fig.3.1p, q**) showed that aged mice have impaired glucose tolerance and are more insulin resistant. Therefore, mice display a pattern of age-related visceral adiposity, accompanied by reduced energy expenditure and insulin resistance, similar to_age-related obesity and associated metabolic disorder in humans.

WAT undergoes massive adipogenesis during aging.

To better understand adipocyte dynamics, we previously developed the AdipoChaser mice for tracking adipogenesis[66,67,69,81,82]. This mouse model is a doxycycline (dox)-based, tet-responsive labeling system for the inducible, permanent labeling of Adiponectin (Adipoq) expressing cells, which represent mature adipocytes. With the AdipoChaser mice, doxycycline could be introduced at any time to label all mature adipocytes, and new adipocytes generated during the chasing period (after doxycycline withdrawal) would not be labeled. To determine if aging is accompanied by adipogenesis, we labeled all the adipocytes of 3-month-old male AdipoChaser-mT/mG mice (**Supplementary Fig.3.2a**) with GFP and tracked adipogenesis during early aging (**Supplementary Fig.3. b**). Consistent with our previous studies, we observed very few new adipocytes (i.e., GFP negative adipocytes) in the gWAT of 6-month-old mice, indicating that the turnover rate of adipocytes is extremely low in young adults (**Fig. 3.1a,b**). When the mice were 9-month-old, clusters of GFP negative, newly generated adipocytes started to emerge, resulting in an adipogenesis rate of 68.05%. More adipocytes were generated in 12-month-old mice, as 82.33% of the adipocytes were newly formed (**Fig. 3.1a,b**). Adipocyte size was also increased at 12-months, confirming the adipocyte hypertrophy during aging[71] (**Fig.3.1c,d**). The sizes of newly generated adipocytes, however, were not different from the average size of adipocytes of each time point (**Fig.3.1e**). To further confirm adipogenesis during aging, we also generated PdgfraChaser-mT/mG mice (**Supplementary Fig. 3. 2c**) to label and track all Pdgfra+ cells, which labels most of the APCs. We treated 3-month-old male PdgfraChaser-mT/mG mice with doxycycline and tracked adipogenesis of these Pdgfra+ cells during early aging (**Supplementary Fig.3.2d**). In 3-month-old PdgfraChaser-mT/mG mice, GFP+ cells were located in peri-endothelial of blood vessels, and mature adipocytes were not labeled in the gWAT (**Supplementary Fig.3.2e**). When the mice were 12-months-old, clusters of GFP+ adipocytes were found in the gWAT (**Supplementary Fig.3.2e**). These labeled adipocytes represent adipocytes formed during aging originated from Pdgfra+ APCs. Thus, adipogenesis of APCs is a significant contributor to age-related gWAT expansion in the male mice.

APCs from aged mice have a cell-autonomous high adipogenic capacity *in vivo*

Do APCs cell-autonomously undergo massive adipogenesis during aging? Alternatively, is there a systemic stimulus required for age-related adipogenesis? APCs were reported to be less immunogenic and less subject to rejection than other cell types following transplantation into mice[83]. We then set out to test the *in vivo* adipogenic ability of APCs from gWAT of young vs. aged male mice through transplantation. An equal number of APCs (Lin-, CD45- CD31- Ter119-) from the stromal vascular fraction (SVF) of gWAT were mixed from 2.5-month-old male CAG-EGFP mice (GFP+, "young" APCs) and from

12-month-old male Rosa26-loxp-mTomato-stop-loxp-GFP (Rosa26-mT/mG) mice (Tomato+, "aged" APCs). The cell mixture was transplanted into the sWAT of 2.5-month-old male wide type (WT) mice (**Fig.3.1f**). When the Matrigel transplants were dissected 1 month later, we observed that more "aged" APCs (Tomato+) had differentiated into adipocytes (**Fig.3.1g**), resulting in a 2.5-fold more adipocytes compared to “young” APCs (GFP+) (**Fig.3.1h**). These GFP+ and Tomato+ cells (differentiated from GFP+ or Tomato+ APCs) were similar in size (**Fig.3.1i**), and were indeed mature adipocytes, as they had a unilocular morphology (single lipid droplet) (**Fig.3.1j**) and were perilipin positive (**Fig.3.1k**). To further confirm our observation, we also transplanted equal numbers of Tomato+ APCs from the gWAT of 2.5-month-old and 12-month-old male Rosa26-mT/mG mice separately into the different sides of sWATs of the same male WT mice (**Supplementary Fig.3.4a**). Four weeks after transplantation, the "aged" APCs had a significantly higher (3 fold) adipogenesis rate, compared to the "young" APCs (**Supplementary Fig.3.4b—e**). Thus, the APCs from older mice maintain their high adipogenic potential after transplantation into a “young” environment.

To test if age-related systemic stimulation is sufficient to trigger APC adipogenesis, we then took the reverse approach and transplanted APCs from young mice into aged mice. Equal numbers of “young” Tomato+ APCs from gWAT of 2.5-month-old male Rosa26-mT/mG were transplanted into sWATs of 12-month-old and 2.5-month-old male WT mice (**Supplementary Fig.3.4f**). Four weeks after the transplantation, no significant adipogenesis of the “young” APCs was observed in young or old recipient mice

(**Supplementary Fig.3.4g,h**). Similarly, when GFP+ APCs from young CAG-EGFP mice were transplanted into aged WT mice (**Supplementary Fig.3.4i**), the age-related systemic stimulation and microenvironment did not trigger significant adipogenesis of the "young" APCs (**Supplementary Fig.3.4j,k**).

Altogether, these transplantation results indicate that the "aged" APCs cell-autonomously exhibit greater adipogenic rate in the *in vivo* setting, regardless of "young" or "aged" microenvironment.

Aging generates a new APC population with a globally activated adipogenic program

To explore the molecular underpinnings of the adipogenic properties of the APCs from aged mice, we performed scRNA-seq of the CD45- CD31- Ter119- stromal vascular cells from the gWAT of aged and young mice (n=3 mice/group) (**Supplementary Fig.3.5a**). Among the 19,534 cells sequenced, 15,194 cells (78%) were identified as progenitor cells (**Supplementary Fig.3.5b**), based on the expression of classic APC markers PDGFRα, CD34 and Ly6a[64,86,87] (**Supplementary Fig.3.5c-e**). While the variation between mice within the same group was minimal (**Supplementary Fig.3.5f, g**), there were dramatic transcriptomic shifts between young and aged cells (**Supplementary Fig.3.5h**).

Combining the "young" and "aged" progenitor cells, we used unsupervised clustering of gene expression profiles and identified five cell clusters (**Fig.3.2a**). Based on recently published scRNA-seq analyses of WAT APCs[78,84,85], these clusters are: 1) adipocyte stem cell (ASC); 2) intermediate adipocyte progenitor (IAP); 3) committed preadipocyte 1 (CP-1); 4) committed preadipocyte 2 (CP-2); 5) committed preadipocyte, age-specific (CP-A). We found that aging significantly remodeled the progenitor cell population, as "aged" cells had "shifted" away from "young" cells, and cells from the two groups had little overlap (**Fig.3.2b, c**). Using Slingshot trajectory analysis, we revealed potential lineage relationships among these APC clusters. Within the "young" progenitor cells, ASC had two developmental trajectories, both through IAP, and terminated as CP-1 and CP-2 (**Fig.3.2d, Supplementary Fig.3.5i**). Interestingly, within the "aged' progenitor cells, ASC had one additional, unique developmental trajectory, which terminated as CP-A. Quantifying the percentage of each cell cluster showed that the CP-A population is highly enriched in aged mice, whereas the CP-1 population was dramatically reduced in aged mice (**Fig.3.2e**). These results suggest that the aging process generated a new adipogenic lineage from ASC to CP-A.

Next, we used CytoTRACE analysis and sorted the order of these APC clusters based on differentiation status as predicted by transcript abundance (**Fig.3.2f Supplementary Fig.3.5j, k**). From stem cells to committed precursor cells, the order of these clusters was: ASC, CP-2, IAP, CP-1, and CP-A. For each type of cluster, the “Young” APCs were always more stem cell-like compared to the “aged” APCs. And among all clusters, the “aged” CP-A cluster was identified as the most committed APC. The mesenchymal progenitor marker *Pdgfra* was universally expressed in all clusters (**Fig.3.2g**), but each cluster also showed unique markers (**Supplementary Fig. 3. 5l**). The ASC cluster expressed *Cd55*, *Pi16*, and *Dpp4* (**Fig.3.2h**, **Supplementary Fig. 3. 5l, m**); the IAP cluster expressed common adipocyte progenitor markers (e.g., *Pdgfra*), and intermediate levels of ASC markers and committed preadipocytes (**Supplementary Fig.3.5l**); the CP-1 cluster expressed *Apoe*, *Igf1,* and *C7* (**Fig.3.2i**, **Supplementary Fig.3.5l**); the CP-2 cluster expressed *Mfap4*, *Mgp,* and *Cilp* (**Fig.3.2j**, **Supplementary Fig.3.5l**). The CP-A cluster was marked by expression of *Lifr* and *Thbs1* (**Fig.3.2k**, **Supplementary Fig.3.5l, n**). We used LIFR as a CP-A marker and found that LIFR^{high} cells in Lin- SVFs of gWAT gradually increased as mice aged from 6 to 9 months old, and there was a sudden rise (3.8 folds) of LIFR^{high} cells in 12-month-old mice (**Fig. 3. 2l**, **Supplementary Fig. 3. 6a**). LIFR^{high} cells in Lin- SVFs of sWAT also increased during aging, to a much lesser extent (**Fig.3.2l**). We then isolated CP-A cells through fluorescence-activated cell sorting (FACS) and measured the mRNA levels of CP-A markers in CP-A, non-CP-A Lin- SVFs, and mature adipocytes. qPCR confirmed higher expression of *Thbs1*, *Lifr*, *Ccl11*, *Spry1* and *Hsd11b1* (**Supplementary Fig.3.6b**). Among these marker genes, *Lifr*, *Ccl11* and *Hsd11b1* were also highly expressed in mature adipocytes, while *Thbs1* and *Spry1* were selectively expressed in APCs. To validate the *in vivo* fate of ASCs from aged mice, Tomato+ primary ASCs (PDGFRα^{+} DPP4^{+}) from young (3-month-old) or aged (12-month-old) male mT/mG mice were transplanted into young WT recipients and dissected 3 days after the transplantation. Flow cytometry analysis indicated that around 80% of transplanted ASCs from the gWAT of aged mice had differentiated into LIFR$^{\mathbf{high}}$ CP-A cells, while only 15% of ASCs from young mice turned into LIFR^{high} cells (**Fig.3.2m**, **Supplementary Fig.3.6c**). These results demonstrate that ASCs from aged mice are indeed progenitors for CP-As and there is a high rate of commitment of ASCs into CP-As.

We then compared our clusters with the previously published APC clusters in WAT. For each of the published APC clusters in the indicated studies, gene module scores were calculated based on a list of significantly enriched marker genes. Burl et al. identified two major APC clusters (ASC1 and ASC2) in gWAT representing different cell states during adipogenesis. In comparison[65], the ASC cluster we noted highly overlapped with the Dpp4/Pi16/Cd55+ ASC2 cluster. Our CP-1 cluster highly overlapped with the Icam1/Igf1/Adam12+ ASC1 cluster. Our IAP and CP-2 clusters partially overlapped with both ASC1 and ASC2 clusters, and the CP-A cluster partially overlapped with the ASC1 cluster (**Supplementary Fig. 3. 6d, e)**. Sárvári et al. utilized single-nucleus RNA-seq to identify four major APC clusters in gWAT[70]. Our ASC cluster overlapped with the FAP2, FAP3, and FAP4 clusters. IAP, CP-1, CP-2, and CP-A clusters partially overlapped with the FAP1 and FAP2 clusters (**Supplementary Fig.3.6f, g)**. Schwalie et al. identified three major APC clusters in sWAT[87]. Our ASC cluster overlaps extensively with the P1 cluster. Our IAP, CP-1, CP-2, and CP-A clusters overlap with the P2 cluster, and partially overlap with the adipogenesis-regulatory cells, the P3 cluster (**Supplementary Fig.3.6h, i**). Nguyen et al. recently identified the aging-dependent regulatory cell (ARC) in sWAT of aged mice[71]. We did not find many ARCs in all our five clusters, confirming the sWAT specific location of ARCs (**Supplementary Fig.3.6j, k**). Taken together, the ASC, IAP, CP-1, and CP-2 clusters we identified shared similarities with previously defined APC populations. Despite the similarities, our study uniquely identified the CP-A cluster as an age- and depot-specifically enriched population with unique molecular characteristics.

Human visceral WAT shows similar patterns of age-related APC remodeling

To access the translational relevance of these findings, we set out to verify if humans also have the same CP-A population with scRNA-seq. CD45-CD31-CD235a- SVFs from human peripancreatic WAT (pWAT) were used for scRNA-seq (5 human samples of different sexes and ages). Among the 24,794 cells sequenced, 20,431 cells (82%) were identified as progenitor cells (**Supplementary Fig.3.7a)**. Unsupervised clustering of gene expression profiles divided these APCs into eight cell clusters (Hu0-Hu7) (**Fig.3. 2n**). To compare the identified APC populations from mice with the human clusters, we calculated the ASC and CP-A gene module score as a sum of mouse marker genes (**Fig.3.2o**). Clusters Hu0, 2, 3, 6 were enriched with mouse ASC markers, while clusters Hu1, 5, 7 were enriched with mouse CP-A markers (**Fig.3.2o**). Thus, both mouse ASC and CP-A similar cells can be identified in human pWAT. All progenitor cells showed abundant expression of APC marker PDGFRA (**Supplementary Fig.3.7b**) and PDGFRB (**Supplementary Fig.3.7c**). Human clusters similar to mouse ASC had high expression of the ASC markers *CD55* and *Pi16*+ (**Supplementary Fig.3.7d,e**). Human clusters similar to mouse CP-A had high expression of the CP-A marker *LIFR* (**Supplementary Fig.3.7f**), and moderately (or partially) expressed *PPARG*, *FABP4*, and *LPL* (**Supplementary Fig.3.7g–i**). We then used flow cytometry to analyze the CP-A (LIFR^{high}) population in human pWAT of different age groups. Among the six samples obtained from male donors, we isolated SVFs and enriched APC (CD31- CD45-

CD235a- PDGFRα+ cells) (**Supplementary Fig.3.7j, k**), and found a trend for the CP-A population to dramatically increase with age (**Fig.3.2p**). Thus, APCs in human pWAT may undergo similar remodeling during aging, and the human CP-A population may also contribute to age-related obesity.

CP-A population has a high proliferation and adipogenesis rate both *in vitro* and *in vivo*

We next examined the localization of CP-As in human pWAT. Histological examination revealed that CP-As in pWAT from aged humans were distributed throughout the tissue between mature adipocytes, which is different from the typical perivascular enrichment of APCs in young adults (**Fig. 3. 3a**).

Pathway analysis of the mouse scRNA-seq data suggested that proliferation-related pathways, such as TGFβ[68] and mitotic signaling, are enriched in the "aged" ASCs compared to the "young" ASCs (**Fig. 3.3b**). Moreover, the adipogenesis pathway is highly enriched in the age-specific CP-A population (**Fig. 3. 3c**). This analysis suggests that the "aged" ASC and CP-A populations may have increased proliferation and inflammation, and the CP-A population also has increased adipogenesis.

We then determined the capacity of total APC to proliferate and differentiate into adipocytes in 3D culture *in vitro* (**Supplementary Fig.3.8a**). The enriched APCs were first mixed with Matrigel and cultured in the growth medium for 72 hours. An adipogenic cocktail was then added to differentiate these cells into adipocytes. Starting with the same number of cells, “aged” APCs proliferated into more cells compared to the “young” APCs (**Supplementary Fig.3.8b, c**). However, the adipogenesis rate (the percentage of Bodipy+ adipocytes in Tomato+ cells) for both “young” and “aged” APCs were similarly high, close to 100%. The advantage of the 3D culture system is that we do not need the APCs to grow densely and attach prior to adipogenesis. We then added the adipogenic cocktail 16 hours later after seeding to the enriched APC populations (**Supplementary Fig.3.8d, e**). “Aged” APCs had higher (but not significant) adipogenesis rate, and significantly higher proliferation rate, as the total Tomato+ cell number from “aged” APCs was more than 2 fold greater than the “young” APCs (**Supplementary Fig.3. 8e**). We used_qPCR to validate the increase of mRNAs of specific genes during differentiation, after the adipogenic cocktail been added 16 hours after seeding (**Supplementary Fig.3.8f**).

In light of results from the pathway analysis, we next inquired whether the CP-A population generated during aging has a greater capacity for proliferation and differentiation. We next enriched individual APC populations and tested their proliferation and adipogenic capacity *in vitro*. To minimize stress to cells, a magnetic beads-based negative selection was used to enrich APCs (Lin-, CD31- CD45- Ter119-) from freshly isolated SVFs from the gWAT of young and aged male Rosa26-mT/mG mice. To enrich the ASC population, we isolated the DPP4+ population from APCs. DPP4+ and DPP4- populations were validated by flow analysis (**Supplementary Fig.3. 8g**). To enrich the CP-1 and CP-A population, negative selection, depleting DPP4+ ASC, CD9+ CP-2 and IAP populations in APCs were employed. The enriched populations were validated and showed a low percentage of DPP4 and CD9 expression and a high percentage of LIFR expression on flow analysis (**Supplementary Fig.3.8h, i**). Interestingly, more DPP4+ APCs from the gWAT of aged male mice switched from CD9- cells to CD9+ cells, suggesting that a certain number of cells in the aged ASC population may have started the adipogenesis program along the trajectory to IAP (**Supplementary Fig.3.8j**). This also validates that aged ASCs are more differentiated than young ASC as suggested by the CytoTRACE analysis (**Fig.3.2e).** The "aged" ASC population had an adipogenesis rate similar to the "young" ASCs, but they had a significantly higher proliferation rate (**Fig.3.3d, e**). We also compared the age-specific CP-A population with the "young" CP-1 population, which shares the highest molecular similarity with the CP-A population according to the scRNA-seq results. Importantly, the CP-A population not only had a more than four fold higher proliferation rate compared to the CP-1 population, but had the highest adipogenesis rate among all populations tested (**Fig.3.3f, g**). Thus, the CP-A population, uniquely enriched with age, has the most remarkable capacity for proliferation and differentiation *in vitro*.

We then enriched APC subpopulations and measured their proliferation rate *in vivo*. Young (3-month-old) or aged (12-month-old) WT male mice were treated with EdU. 2 hours after EdU incorporation, flow cytometry analysis indicated that around 1.23% of ASCs from the gWAT of aged mice were EdU+, while only 0.3% of ASCs from young mice were EdU+ (**Fig.3.3h, Supplementary Fig.3.8k**). For CP-As, around 3.91% of them were EdU+, while only 0.86% of CP-1s from young mice were EdU+ (**Fig.3.3h, Supplementary Fig.3.8k**). These data indicate that CP-As have a very high proliferation rate *in vivo*.

Next, we enriched APC subpopulations and tested their adipogenic capacity *in vivo*. A large amount of DPP4- APCs (containing all APC populations other than ASC), CP-1, and CP-A populations were collected from freshly isolated SVFs from gWAT of 2.5-month-old and 12-month-old male Rosa26-mT/mG mice, and equal numbers of these enriched "young" and "aged" populations were transplanted into the different sides of the sWATs of male WT mice (**Fig.3.3i**). The "aged" DPP4- APCs grew substantially larger in volume compared to the "young" DPP4- APCs (**Fig.3.3j,k**). More notably, the CP-A population grew six times more in adipocyte number than the CP-1 population (**Fig. 3.3l,m**), indicating that the CP-A population has a striking ability to proliferate and differentiate *in vivo*. These Tomato+ cells (differentiated Tomato+ APCs) were indeed mature adipocytes, as they have a unilocular morphology (single lipid droplet) and were perilipin positive (**Supplementary Fig. 3. 9a, b**).

Taken together, both the *in vitro* and *in vivo* results indicate that the CP-A population has a greater capacity for proliferation and differentiation, compared to the other APC populations.

LIFR is essential for CP-A adipogenesis

As one of the top CP-A markers shared by mice and humans, we next explored the function of LIFR in CP-As. LIFR has been reported to play important roles in cell proliferation, differentiation, and survival[78]. However, the role of LIFR in APCs is not clear. We first treated 3D cultured Tomato+ primary CP-As isolated from aged male Rosa26-mT/mG mice with LIFR inhibitor EC359, together with adipogenic cocktails. LIFR phosphorylates and activates STAT3, which is an essential downstream effector of LIFR[79]. Treating CP-As with LIFR inhibitor EC359 effectively reduced STAT3 phosphorylation level (**Supplementary Fig. 3. 10a**), validating EC359 as a potent LIFR inhibitor. After induced adipocyte differentiation, LIFR inhibitor blocked adipogenesis of these aged APCs, while there was no significant decline in total cell number (**Fig. 3. 4a, b**). When we transplanted GFP+ primary CP-As isolated from aged male CAG-EGFP mice and treated mice with EC359, the number of GFP+ adipocytes differentiated from GFP+ APCs was only about half of the vehicle-treated GFP+ primary CP-As (**Fig. 3. 4c, d**). We then used Lentivirus-mediated shRNA to knockdown *Lifr* in Tomato+ primary Lin- SVFs isolated from aged male Rosa26-mT/mG mice (**Supplementary Fig. 3. 10b**). At the end of the induced adipocyte differentiation, *Lifr* knockdown dramatically reduced the total cell number and sharply reduced the adipogenesis rate of these aged APCs (**Fig. 3. 4e, f**). When we transplanted *Lifr* shRNA Lentivirus-transfected Tomato+ primary Lin- SVFs (isolated from aged male Rosa26-mT/mG mice), the number of Tomato+ adipocytes differentiated from Tomato+ SVFs was only about one-third of the control Lentivirus treated Tomato+ SVFs (**Fig. 3. 4g, h**). We also introduced Lentivirus-mediated *Lifr* over-expression to Tomato+ primary Lin- SVFs isolated from young male Rosa26-mT/mG mice (**Supplementary Fig. 3. 10c**). After induced adipocyte differentiation, overexpression of *Lifr* resulted in a fold increase of adipocyte and total cell number (**Fig. 3. 4i, j**). When we transplanted *Lifr* over-expression Lentivirus-transfected GFP+ primary Lin- SVFs (isolated from young male CAG-EGFP mice), the number of GFP+ adipocytes differentiated from GFP+ primary Lin- SVFs increased by more than one-fold compared to control Lentivirus-transfected GFP+ primary Lin- SVFs (**Fig. 3. 4k, l**). Lastly, we used LIFR inhibitor EC359 to treat mice for 10 weeks, starting at 9 months of age. Inhibiting LIFR resulted in a reduction of gWAT weight, while sWAT weight was not altered (**Supplementary Fig. 3. 10d, e**). These results suggest that LIFR signaling is a critical regulator of CP-A adipogenesis.

3.3 Discussion

As a highly plastic organ, WAT alters in volume in adaptation to a variety of physiological and pathological metabolic challenges. We and others have shown that without any metabolic challenge, healthy young adult mice and humans have extremely low adipocyte turnover rates. WAT plasticity under many physiological and pathological challenges has been extensively studied, such as cold exposure and high fat diet feeding[59,60]. However, the expansion of WAT during early aging is surprisingly understudied. In this study, we provide the first cellular and molecular evidence that aging triggers massive adipogenesis and introduce a newly identified an age-enriched APC population, the CP-As, which have high adipogenic capacity (**Supplementary Fig. 3. 10f**).

Among the two major fat depots, vWAT and sWAT, vWAT exhibits the most adipogenesis during aging. As vWAT and sWAT are fundamentally distinct organs with distinct development timelines, molecular signatures, and metabolic functions[59,60,80], it is not surprising that age-related adiposity happens in the vWAT at a much higher rate. Compared to hypertrophy, which gives WAT only limited potential to expand, adipogenesis is alarming because it grants WAT unlimited potential for growth. Our findings on age-related adipogenesis, therefore, highlights adipogenesis as the key process, besides adipocyte hypertrophy, to target for intervention for age-related obesity and other associated diseases.

Age-related adiposity accelerates aging and shortens life expectancy. Signaling pathways that are known to extend lifespan, e.g., SIRT, FOXO, and JNK, often inhibit adipogenesis (the making of new adipocytes) and decrease WAT mass[81-85]. Conversely, signaling pathways that are known to shorten lifespan, e.g., insulin/IGF-1 and mTOR, often do the opposite[86-88]. Similarly, strategies that promote longevity and youthfulness often inhibit WAT expansion in aged animals and older humans, such as caloric restriction[89-91] and fasting[92]. These critical studies suggest that inhibiting WAT expansion during aging is closely linked to increased health span and lifespan. Our study expands on this and suggests that to limit WAT expansion during aging, it is crucial to understand the underlying mechanism of age-related adipogenesis.

Driven by the state-of-art scRNA-seq technique, several elegant studies provided new insights into APC heterogeneity in a fat depot-specific manner[93-95]. A few major APC subpopulations had been identified, including 1) adipose stem cells (ASCs)[55,56,58], which were also identified in our study as the ASC population; 2) committed preadipocytes (adipocyte progenitors)[65,66,68], which were identified in our study as the CP-1 and CP-2 populations; 3) fibro-inflammatory progenitors (FIPs)[66,96-98], which were identified in the gWAT of young adults with anti-adipogenic behavior, and pro-inflammatory and pro-fibrosis response; 4) adipogenesis regulators (Aregs)[67], Aregs inhibit adipogenesis and were found in sWAT of young adults; 5) aging-dependent regulatory cell (ARC)[71], ARCs were only found in aged sWAT. ARCs secrete pro-inflammatory chemokines and are resistant to adipogenesis, and they inhibit the differentiation and proliferation of neighboring adipogenic precursors. Our ASC cluster bears a close resemblance to the gWAT PDGFRβ+ stromal subpopulation[66]. The gene signatures of our ASC cells are molecularly similar to those of APCs (adipogenic progenitor cells) and CPs (committed preadipocytes), the two adipogenic clusters defined previously[66]. In the same study, another anti-adipogenic subpopulation, or FIPs, was also defined in gWAT. In our gWAT scRNA-seq data, the FIP markers were not apparently enriched within the defined clusters, likely because the previous study analyzed pre-selected PDGFRβ+ cells, which represent a fraction of SVF cells so that FIPs are not resolved by scRNA-seq in our samples. In the present study, we identified a new, committed preadipocyte population, the CP-A population. Although in a strict sense, CP-A is not completely absent from the young mice, the extremely low frequency in young mice and more than 20-fold increase in aged mice make the population highly enriched in the aged state. CP-As are also uniquely enriched in the visceral WAT of older humans. Importantly, the CP-A cells displayed superior capacity, compared to all other known APC subpopulations, to proliferate and differentiate into mature adipocytes, both *in vitro* and *in vivo*. Interestingly, when we observed a high level of adipogenesis in 9-month-old mice, the CP-As (as LIFR high expressing Lin- SVFs) were not significantly increased at this time point. It is possible that CP-As are rapidly disappearing because they on the active path producing new adipocytes, so we did observe an increase in LIFR^{high} APCs. When mice were 12 months old, the number of CP-As significantly increased together with a high level of adipogenesis. This phenomenon may indicate an overproduction of CP-As as mice age further, accelerating the adipogenic capacity of gWAT. CP-As (LIFR^{high} Lin- SVFs) also exist in the sWAT of mice, and the percentage of CP-As also increases during aging, although not as dramatically as in the gWAT. The adipogenesis of CP-As in sWAT, however, may be inhibited by the sWAT-specific ARCs, limiting the expansion of sWAT during aging.

The CP-A markers LIFR and Thbs1 distinguish these cells from other committed preadipocytes. LIFR forms a heterodimer with gp130 and induces the JAK-STAT3 signaling pathway[49], and JAK-STAT3 has been demonstrated to promote adipogenesis from APCs[50]. Pathway enrichment analysis revealed the JAK-STAT3 pathway was upregulated in the CP-A population, suggesting that LIFR signaling was activated. Indeed, we have shown that LIFR controls CP-A differentiation. Inhibition or knockdown LIFR dramatically impairs CP-A adipogenesis, while overexpression of LIFR increases adipogenesis. Moreover, EC359, the first-in-class LIFR inhibitor, decreases gWAT mass specifically after administration to mice. Thus, LIFR plays an essential role in promoting CP-A adipogenesis. Future experiments will focus on determining the cell type(s) that secrete LIF or other ligands that activate LIFR on the CP-A cell membrane. The activation could be endocrine- or paracrine-regulated. Moreover, LIFR continues to be highly expressed in mature adipocytes, and the function of LIFR in mature adipocytes has yet to be explored. A recent study showed that LIFR signaling induces adipocyte lipolysis, which requires STAT3[79]. It is possible that LIFR is only highly expressed in newly generated adipocytes. LIFR, together with a yet unknown set of genes, may make these newly generated adipocytes unique both molecularly and functionally. When we resolve the technical limitations of separating new and pre-existing adipocytes, we will be able to answer these critical questions.

In addition to the discovery of the new age-specific CP-A population, our scRNA-seq data showed that the other APC populations had little overlap between the aged and young groups, indicating that the aging process significantly transformed all APC sub-populations. Indeed, we found that the “aged” ASC population had a higher proliferation rate, which is essential for age-related adipogenesis. Interestingly, a large proportion of aged ASCs expressed CD9, a representative marker of IAP and CP-2 populations. These findings suggest that aged ASCs might have started the differentiation program and have a higher tendency to differentiate into mature adipocytes. CD9 is a marker of the FIP population[66]. Thus, CP-2 is likely to be the analogous population of FIPs. CD9+ progenitors have been reported to control adipose tissue fibrosis[101]. As vWAT fibrosis progresses during aging[102], the ASC to CP-2 transition could contribute to age-related adipose fibrosis and metabolic dysfunction. Due to the presence of anti-adipogenic stromal cell subpopulations identified in multiple fat depots[66,67,71,96,97], we cannot exclude the possibility that the age-dependent gWAT hyperplastic expansion results from the dysregulation of suppressive mechanisms governed by anti-adipogenic cells such as FIPs or Aregs. This question requires further investigation.

Our *in vivo* transplant and *in vitro* differentiation results suggest that “aged” APCs cell-autonomously have a greater adipogenic capacity, even when disassociated within the aging microenvironment. However, the aging microenvironment is potentially crucial for driving the remodeling of APCs, which may have started during early aging. Dr. James Kirkland’s group elegantly showed that APCs could undergo cellular senescence and lose the ability to differentiate into adipocytes[103]. Therefore, their study suggested that cellular senescence contributes to age-related fat loss, which happens in the very aged population. In this study, we focused on WAT expansion during early and middle-aging. Our study indicates that although some APCs may become senescent and stop undergoing adipogenesis during aging, sufficient APCs are generated during early aging and contribute to the massive adipogenesis we observed *in vivo*. Interestingly, senescent cells accumulate specifically in vWAT during early aging[94-96], and we showed that the vWAT has the highest adipogenic rate. It is possible that the senescent microenvironment promotes adipogenesis of APCs in vWAT during early aging. Firstly, cellular senescence positively correlates with WAT mass. Inducing cellular senescence through genetic manipulation often results in WAT expansion[107,108]; in addition to accumulating during aging, senescent cells also accumulate in obesity, especially in the vWAT[109-114], which has active adipogenesis. Secondly, senescent cells are known to stimulate adult stem cell proliferation and differentiation or tumor proliferation[115-117]. Lastly, inflammatory signals are known to promote adipogenesis[118-170]; senescent cells may promote adipogenesis through the senescence-associated secretory phenotype[121-123], which contains numerous pro-inflammatory cytokines. Currently, we are trying to determine if cellular senescence promotes adipogenesis by remodeling the APC niche.

Future studies are required to generate new mouse models to specifically track CP-As *in vivo* and quantify the contribution of CP-As to age-related adipogenesis. Effective strategies eliminating the CP-A population or inhibiting its proliferation and differentiation will prevent the development of visceral adiposity during aging. However, whether adipogenesis during aging promotes or protects from metabolic disorders has yet to be studied. Meanwhile, the newly generated adipocytes may have distinct molecular and metabolic features. Future work will also focus on if manipulating visceral adipogenesis could restore the metabolic function of gWAT and improve age-related metabolic disorders, and eventually increase healthspan and lifespan. Besides APCs, various immune cell types have been reported to regulate APC differentiation and adipose homeostasis under different conditions in mice and humans[124-127]. We have also shown a significant shift in nearly all the immune cells in aged gWAT. The determination of how the CP-A population emerges during aging and whether the immune-regulation of adipose tissue plasticity during aging plays a role in this process is another avenue to pursue. It is also worth investigating the crosstalk between different immune cell types and all the APC subpopulations to better understand the molecular and cellular dynamics in adipose remodeling to pinpoint key regulatory cell types and genes. Other than immune cells, other key regulators discussed above, such as cellular senescence, adipose fibrosis, may also remodel the APC subpopulations and promote the generation of the CP-A population.

3.4 Conclusions

Here, we find that mice mimic age-related fat expansion in humans. *In vivo* lineage tracing shows that massive adipogenesis (the generation of new adipocytes), especially in the visceral fat, is triggered during aging. Thus, in contrast to most types of adult stem cells that exhibit a reduced ability to proliferate and differentiate, the adipogenic potential of adipocyte progenitor cells (APCs) are unlocked by aging. *In vivo* transplantation and 3D imaging of transplants show that visceral APCs in aged mice cell-autonomously gain high adipogenic capacity. Single-cell RNA sequencing analyses reveal that aging globally remodels APCs. Herein, we identify a novel Committed Preadipocyte population uniquely enriched in Aged mice (CP-A), existing both in mice and humans, with a global activation of proliferation and adipogenesis pathways. CP-A cells display high proliferation and adipogenesis activity, both *in vivo* and *in vitro*. LIFR serves as a functional marker of CP-A, which promotes CP-A adipogenesis. Together, these findings define a new fundamental mechanism involved in fat tissue aging and offer prospects for preventing and treating age-related metabolic disorders

3.5 Methods

Mice

Mice were maintained in a 12h dark/light cycle and housed in groups of three to five with unlimited access to water and food (chow diet, number 5058, lab diet; or doxycycline chow diet [600 mg/kg], S4107, Bio-Serv, as described for individual experiments). All mice were on a pure C57BL/6J background. Adn-rtTA and FAT-

ATTAC mouse lines were generated in the Scherer laboratory as previously described1,2. TRE-Cre (Jax stock no. 006234), Rosa26-loxP-STOP-loxP-mT/mG (Jax stock no. 007676), Pdgfra-rtTA (Jax stock no. 034459), and CAG-EGFP (Jax Stock no. 006567) mouse lines were obtained from the Jackson Laboratories. The Institutional Animal Care and Use Committees of City of Hope, Duarte, have approved all animal experiments.

Metabolic cage studies were performed in the City of Hope Comprehensive Metabolic Phenotyping Core facility. Oxygen consumption was calculated relative to lean mass. GTT was performed in mice without access to food for 12 h before administration of 2 g/kg body weight glucose by intraperitoneal injection. ITT was performed in mice without access to food for six hours before administering 0.75 U/kg body weight insulin (Eli Lilly) by intraperitoneal injection. To induce adipocyte apoptosis in FAT-ATTAC mice, AP21087 (Ariad Pharmaceuticals) in 4% ethanol, 10% PEG400, 1.75% Tween-20 in water were administered by intraperitoneal injection at a dose of 0.2 μg/g body weight every day for 7 days.

Isolation of mouse adipose SVFs and enrichment of APC subpopulations

gWAT was minced and transferred to a 50 mL Falcon tube containing 10 mL digestion buffer (100mM HEPES pH 7.4; 120mM NaCl; 50mM KCl; 5mM Glucose; 1mM CaCl2, 1.5% BSA, and 1 mg/mL collagenase D, Roche, 11088882001). The tissue was incubated in a 37℃ shaking water bath for 30 min. Digestion was stopped by adding 35 mL 2% FBS in PBS. The solution was passed through 100 μm and then 40 μm strainers and centrifuged at 400 g for 5 min. The supernatant was aspirated, and the SVF pellet was collected.

Lin- SVF and enriched ASC, CP-A, CP-1 were obtained by MACS (Stemcell Technologies, 17656). To obtain Lin- SVF, anti-mouse-CD45-PE (1:200, BioLegend, 103106), anti-mouse-CD31-PE (1:200, BioLegend, 102408), and anti-mouse-Ter119-PE (1:200, BioLegend, 116208) were used. To enrich the ASC subpopulation, additional anti-mouse-DPP4/CD26-PE antibody (1:50, BioLegend, 137804) was used. To enrich CP-A and CP-1 subpopulations, the above 4 antibodies plus anti-mouse-CD9-PE (1:200, BioLegend, 124806) antibodies were used. To obtain immune cells from gWAT, anti-mouse-CD45-PE (1:200, BioLegend, 103106) was used and isolated by MACS.

Flow cytometry

For flow cytometry analysis, cells were blocked with anti-mouse-CD16/32 (1:500, BioLegend, 101302) or Human Fc Block (1:20, BD, 564219) for 10 min, and then stained with anti-mouse-CD45-Pacific Blue (1:400, BioLegend, 103126), anti-mouse-CD31-Pacific Blue (1:400, BioLegend, 102422), anti-mouse-Ter119-Pacific Blue (1:400, BioLegend, 116232), anti-mouse-CD140a-APC (1:200, BioLegend, 135908), anti-mouse-DPP4/CD26-PE/Cy7 (1:100, BioLegend, 137810), anti-mouse-CD9-PE (1:400, BioLegend, 124806), anti-LIFR (1:200, Proteintech, 22779-1-AP), and anti-rabbit-488 (1:200, Invitrogen, A-21206) ; anti-rabbit-BV421 (1:200, BioLegend, 406410), anti-human-CD45-PE (1:400, BioLegend, 304039), anti-human-CD31-PE (1:400, BioLegend, 303106), anti-human-CD235a-PE (1:400, BioLegend, 349106), and anti-human-CD140a-APC (1:100, BioLegend, 323512) for individual experiments for 20 min on ice. After antibodies incubation, the cells were washed once with 2% FBS/PBS, and analyzed by BD Fortessa cytometer. The flow plots were analyzed by FlowJo (V10).

For FACS isolation of ASCs from gWAT, total SVFs were blocked with anti-mouse-CD16/32 (1:500, BioLegend, 101302) for 10 min, and then stained with anti-mouse-CD45-PerPC/Cy5.5 (1:400, BioLegend, 103132), anti-mouse-CD31-PerPC/Cy5.5, (1:400, BioLegend, 102420), anti-mouse-Ter119- PerPC/Cy5.5, (1:400, BioLegend, 116228), anti-mouse-CD140a-APC (1:200, BioLegend, 135908), anti-mouse-DPP4/CD26-PE/Cy7 (1:100, BioLegend, 137810), anti-LIFR (1:200, Proteintech, 22779-1-AP), and anti-rabbit-488 (1:200, Invitrogen, A-21206). DAPI was added to distinguish live and dead cells. DAPI- Lin- (CD45- CD31- Ter119-) CD140a+ LIFR- DPP4+ cells were sorted using BD FACSAria III sorter as ASCs.Isolation of human adipose SVFs

Peri-pancreatic WAT samples from deceased cadaveric donors were dissected from the pancreas (processe time within ~8-12 hours). All of the experiments were immediately performed using the fresh tissue samples, without freezing or any preservation. The sampling and examination of human tissues have been approved by the Ethics Committee of COH. WAT from five donors (male, 44-year-old; male, 21-year-old; female, 42-year-old; male, 24-year-old; male, 57-year-old) were used for scRNA-seq, and WAT from four donors (all males, 25, 27, 39, 56, 57, and 58-year-old) were used for flow cytometry analysis. Adipose tissue was minced and transferred to a 50 mL Falcon tube containing 10 mL digestion buffer (1 × PBS, and 10 mg/mL collagenase D, Roche, 11088882001). The tissue was incubated in a 37℃ shaking water bath for 45 min. Digestion was stopped by adding 35 mL 2% FBS in PBS. The solution was passed through a 250 µm mesh (Spectrum, 146487), and then 100 µm and 40 µm strainers, and centrifuged at 600 g for 5 min. The supernatant was aspirated, and the SVF pellet was collected. To obtain Lin- SVFs, cells were incubated with anti-human-CD45-PE (1:200, BioLegend, 304039), anti-human-CD31-PE (1:200, BioLegend, 303106), and anti-human-CD235a-PE (1:200, BioLegend, 349106), and isolated by MACS (Stemcell Technologies, 17654). To enrich immune cells, anti-human-CD45-PE (1:200, BioLegend, 304039) was used and isolated by MACS.

scRNA-seq

Lin- SVF and CD45+ immune cells from 2.5-month-old or 12-month-old C57BL/6J male mice gWAT or Lin- SVFs from human peri-pancreatic adipose tissue (Supplementary Supplementary Table 4) were freshly collected and resuspended in PBS containing 0.04% BSA at a concentration of 800~1000 cells/µl. Cell number and viability were measured by trypan blue using a TC20 Automated Cell Counter (BioRad). Single-cell RNA libraries were prepared by the City of Hope Integrative Genomics Core facility according to the ChromiumTM Single Cell 3’ Reagent Kits v3 User Guide (10x Genomics). Approximately 10,000 cells were loaded on a Chromium single cell Controller instrument (10x Genomics) to form single cell gel beads in emulsion (GEMs). After reverse transcription, GEMs were harvested and the cDNAs were amplified and cleaned up with the SPRIselect Reagent Kit (Beckman Coulter). The barcoded sequencing libraries were constructed using the Chromium Single-Cell 3’ Library Kit

(10x Genomics) for enzymatic fragmentation, end-repair, A tailing, adaptor ligation, ligation cleanup, sample index PCR, and PCR cleanup. Libraries were then sequenced with a NovaSeq 6000 instrument (Illumina) with a depth of 50-100 k reads per cell.

scRNA-seq data processing and quality control

The 10X Genomics Cell Ranger version 3.0.2 single-cell software3 was used to perform sample demultiplexing sequencing alignment to mouse genome mm10, filtering, and unique molecular identifier (UMI) counting to generate gene count matrices. Single cells were identified from background noise by filtering on the proportion of mitochondrial reads (threshold: < 10%), the number of UMI (thresholds: 700-22,000), and the number of detected genes (thresholds: 200-6,000).

Identification of cell clusters

The Seurat R package version 3.04 was used to determine cell clusters by the Louvain algorithm based on similarities in the transcriptome patterns and visualized with t-Distributed Stochastic Neighbor Embedding (t-SNE) and Uniform Manifold Approximation and Projection (UMAP). Highly variable genes selected using the FindVariableFeatures function with default parameters were used for principal component analysis (PCA). The number of Principal Components （n=35 for mouse gWAT cells and n=25 for human pWAT cells） used for Louvain clustering and following visualization was determined using the Jackstraw permutation approach. Following unsupervised clustering, the cell type identities of the clusters were resolved by comparing the cell cluster specific marker genes expressed in each cluster in our own dataset, as identified with a Wilcoxon rank sum test, with known cell-type specific markers curated from literature, single cell atlases, and previous studies in the SVF. To be considered in the cell cluster marker analysis, a gene had to be expressed in at least 10% of the single cells from the cluster of interest and exhibit at least a 0.25 log fold change in the cell cluster of interest than in other cells. Multiple testing was corrected using the Benjamini-Hochberg method to estimate false discovery rate (FDR).

Identification of differentially expressed genes (DEGs) and pathways

To quantitatively determine which genes were affected by aging, we compared the cell transcriptome of each cell type between age groups using the Wilcoxon rank sum test. To be considered in the analysis, a gene had to be expressed in at least 10% of the single cells from at least one of the two groups for that cell type and there had to be at least a 1.1-fold change in gene expression between the groups. Multiple testing correction was performed using the Benjamini–Hochberg method to estimate FDR.

For ASC, CP-1 and CP-2 populations shared between both the young and aged mice, the DEGs were identified by comparing the two age groups and then subjected to pathway enrichment analysis. Since CP-A is only present in the aged group, the CP-A marker genes in the aged condition were used as DEGs and subject to pathway enrichment analysis. Pathways from HALLMARK were assessed for overlap with the DEGs using Fisher's exact test and corrected for multiple testing using the Benjamini–Hochberg method to estimate FDR. Enrichment score is calculated by number of overlapped genes/number of genes in our cell type specific gene set × 20000/number of genes in the pathway.

Single-cell trajectory analysis

To infer cell lineages of complex communities of heterogeneous cells, pseudo-temporal reconstruction was performed by two methods. The Slingshot R package6 was used to infer multiple branching lineages for pre-existing clusters based on the minimum spanning tree followed by simultaneous principal curves with a user-defined root cluster. Here we used ASC as the root cluster because of its adipocyte stem cell suggestive gene expression pattern. The Cytotrace R package7 was implemented with default parameters to estimate the developmental potential of ten cell sets (five APC subtypes in “aged” and “young” conditions) based on feature selected gene-count measures of the normalized expression matrix with APC subtype annotation and “aged” and “young” condition annotation.

Cell-cell communication analysis

Both the Cellphone DB database8 and the iTALK database9 were used to curate ligand-receptor pairs that may mediate intercellular cross-talk between the APC subtypes and immune cell types. Pathway enrichment of the ligand-receptor pairs between cell types were further analyzed based on the overlap with selected pathways from KEGG, Reactome, BIOCARTA, and HALLMARK. Top ligand-receptors were ranked based on the formula: the expression value of the ligand gene from the ligand-secreting cell type * the expression value of the receptor gene from the receptor cell type.

In vivo transplantation of APCs and APC subpopulations

Lin- SVF from the epididymal white adipose tissue (gWAT) of 12-month-old aged Rosa26-loxP-STOP-loxP-mT/mG and 2.5-month-old young CAG-GFP mice were isolated and mixed together at a 1:1 ratio. The cells were resuspended in Matrigel (Corning, CB-40234C). A total volume of 20 µl Matrigel was injected into the subcutaneous adipose depot of recipient mice at a concentration of 10,000 cells/µl. After four weeks, the recipient mice were euthanized, and sWAT was collected. The Matrigel containing transplant was dissected under a fluorescence microscope (Keyence), and the whole transplant was captured under a confocal microscope (Zeiss, LSM880).

For single Tomato+ SVF transplant, Lin- SVF from the epididymal white adipose tissue (gWAT) of 12-month-old aged and 2.5-month-old young Rosa26-loxP-STOP-loxP-mT/mG mice were isolated. The cells were resuspended in Matrigel. A total volume of 20 µl Matrigel was injected to the subcutaneous adipose depot of recipient mice at a concentration of 5,000 cells/µl. The comparable aged and young Lin- SVF were injected into either side of the subcutaneous adipose depot of the same recipient. After four weeks, the recipient mice were euthanized, and subcutaneous adipose tissue was collected.

For transplantation of ASC, CP-1, and CP-A, each cell population was isolated from Rosa26-loxP-STOP-loxP-mT/mG mice and resuspended in Matrigel at a concentration of 1,000 cells/µl. Then 20 µl Matrigel of ASC from 12-month-old aged and 2.5-month-old young mice, or enriched CP-A from aged mice and CP-1 from young mice were injected into either side of sWATs of recipient mice. After two weeks, the recipient mice were euthanized, and subcutaneous adipose tissue was collected.

For 3D imaging and quantification of Matrigel transplants, The Matrigel containing transplant was dissected under a fluorescence microscope (Keyence), and the whole transplant was captured under a confocal microscope (Zeiss, LSM880). Original files were imported to Imaris (Bitplane). All the images and videos were made using Imaris. Quantification of mature adipocyte number and volume were analyzed by the spot function of Imaris. Spots were added to adipocytes manually by a person who is blinded to the transplant images.

EdU proliferation assay

12-month-old or 2.5-month-old male mice were treated with 12.5 mg/kg EdU (5-ehynyl-2'-deoxyuridine, Invitrogen, A10044) through i.p. injection. SVFs from gWAT tissues were harvested 2 hours after EdU injection, and stained with antibodies for flow cytometry analysis. Cells were further stained by using Click-iTTM Plus EdU Alexa Fluor 647 Kit For Imaging (Invitrogen, C10340) with modified procedures. Briefly, cells were fixed with 1% PFA (Electron Microscopy Sciences, 15714S) for 15 min at room temperature, and then incubated with 0.2% saponin (Sigma, 47036-50G-F). Reaction cocktail was added the cells according to the manufacturer's instruction. Cells were then washed with 0.2% saponin, and counterstained with 10 µg/ml Hoechst 33342. Cells were analyzed by BD Fortessa cytometer. The flow plots were analyzed by FlowJo (V10).

In vitro 3D differentiation of APCs and APC subpopulations

Lin- SVF or enriched ASC, CP-1, and CP-A populations were isolated from gWAT of Rosa26-loxP-STOP-loxP-mT/mG mice that were 12-month-old or 2.5-month-old. The cells were cultured as described previously13. After isolation by MACS, the cells were resuspended in complete SVF culture medium (DMEM/F12, Life technologies 10565018) containing 10% FBS (Sigma, 16H328), 1% penicillin/streptomycin, (Hyclone SV30010), and 0.1% gentamicin (Life technologies 1855724) at a concentration of 2,000 cells/µl. The same volume of Matrigel was added to the suspension, and 10 µl mixture was added to the 12-well plate. The plate was incubated in the 37℃ CO2 incubator for 15 min to induce the formation of the gel. Then complete SVF culture medium was added to the wells, and the cells were cultured in the 37℃ CO2 incubator. After three days or 16 hours, an adipogenic cocktail containing dexamethasone (1 µM), insulin (5 µg/ml), isobutylmethylxanthine (0.5 mM), and rosiglitazone (1 µM) was added to induce adipocyte differentiation. After six days of adipogenic induction, the cells were then stained with Bodipy (Invitrogen) and imaged under a confocal microscope (Zeiss, LSM880). The images were analyzed using Zen blue (Zeiss).

LIFR inhibitor EC359 treatment

EC359 (MCE, 50-196-9583) was dissolved in vehicle made with 10% DMSO (Sigma, D8418), 40% PEG300 (Sigma, 202371), 5% Tween-80 (Sigma, P4780) and 45% Saline. Mice were injected with 5 mg/kg EC359 through i.p. for 10-week-treatment or s.c. for *in vivo* CP-A transplantation. Control groups were injected with equal volume of vehicle.

Transfection of APCs with lentiviral particles

APCs were seeded onto 24-well-plate. After reaching 70-80% confluency, cells were treated with 10 µg/ml polybrene (Sigma), and 10 µl per well of LIFR shRNA (m) Lentiviral Particles (Santa Cruz, sc-35809-v) or LIFR Lentiviral Activation Particles (m) (Santa Cruz, sc-421433-LAC). Control shRNA Lentiviral Particles (Santa Cruz, sc-108080) or Control Lentiviral Activation Particles (Santa Cruz, sc-437282) were used as control, respectively. 12 hours after transfection, medium was replaced with fresh SVF complete medium. After reaching confluency, the cells were collected for *in vivo* transplantation or *in vitro* 3D differentiation assays.

Real-Time PCR analysis

RNA was extracted using RNAqueousTM-Micro Total RNA Isolation Kit (Invitrogen, AM1931), and first-strand cDNATM was synthesized using iScript cDNA Synthesis Kit (Bio-Rad, 1708891). Real-Time PCR was performed with the SYBR Green PCR system (Applied Biosystems, A25742). Tbp was used as the internal control for normalization. Primer sequences were as listed: Tbp, 5'-CAGCCTTCCACCTTATGCTC-3', 5'-CCGTAAGGCATCATTGGACT-3'; Thbs1, 5'-AGATGGCAAAGGAGATGCCT-3', 5'-

GCCATCACCATCAGAGTCCT-3'; Lifr, 5'-CTTCGATCCTCAACACAGAGCAG-3', 5'-CGCTTGCTCTACTGTGATGTCG-3'; Ccl11, 5'-AGAGGCTGAGATCCAAGCAG-3', 5'-TGGGAGGTGAAGGAAGTGAC-3'; Spry1, 5'-GGAGGCCGAGGATTTCAGAT-3', 5'-ACAGAATCGTAGCAGGCTGA-3'; Hsd11b1, 5'-CCAGAAGGTAGTGTCTCGCT-3', 5'-GCTCCGCAAATGTCATGTCT-3; Adipoq, 5'-GTTGCAAGCTCTCCTGTTCC-3', 5'-ATCCAACCTGCACAAGTTCC-3'; Plin1, 5'-CTCTGGGAAGCATCGAGAAG-3', 5'-GCATGGTGTGTCGAGAAAGA-3'; Pparg, 5′-TGCACTGCCTATGAGCACTT-3′, 5′-AACCATTGGGTCAGCTCTTG-3′.

Histological analysis

10% formalin-fixed tissues were processed with a standard paraffin tissue embedding protocol to produce sections for H&E staining by the City of Hope Pathology Core facility. For immunofluorescence staining, the sections were dewaxed in xylene and rehydrated in a graded series of ethanol to ddH2O. Slides were placed in 10 mM sodium citrate buffer and boiled for 30 min for antigen retrieval, then blocked in PBST with 5% BSA for 30 min. Primary antibodies used were LIFR (1:200, Proteintech, 22779-1-AP), CD29 (1:400, BioLegend, 303002), Perilipin (1:500, Novus, NB100-60554), GFP (1:400, Abcam, ab13970), and mCherry (1:100, Abcam, ab167453) as described for individual experiments, and incubated at 4℃ overnight. After three times wash with PBS, secondary antibodies used were Alexa Fluor 647 Donkey-anti-Rabbit IgG H&L (1:200, Invitrogen, A-31573), Alexa Fluor 488 Donkey-anti-Goat IgG H&L (1:200, Invitrogen, A-11055), Alexa Fluor 594 Donkey-anti-Rat IgG H&L (1:200, Invitrogen, A-21209), Alexa Fluor 594 Donkey-anti-Mouse IgG H&L (1:200, Invitrogen, A-21203), and Cy3 Donkey-anti-Chicken IgG H&L (1:200, Jackson Immuno, Inc., 703-165-155), and incubated at room temperature for 2 hours. Slides were then counterstained with DAPI and mounted with prolong Anti-Fade mounting medium (Invitrogen, P36961) after being washed with PBS three times. Images were acquired using a fluorescence microscope (Keyence). Adipocyte number and size were analyzed by Image J pluggin Adipocyte Counting Macro.

Western blot analysis

Proteins were extracted from cells using RIPA Lysis Buffer (Merck Millipore, 20-188) supplemented with protease inhibitor (Roche, 11836170001), phosphatase inhibitor cocktail (Sigma, P0044, P5726), and 1 mM PMSF (Sigma, P7626), and then separated by SDS-PAGE and transferred to PVDF Blotting Membrane (Bio-Rad, 1620177). Antibodies against phospho-Stat3 (Tyr705) (Cell Signaling Technology, 9145S) and Stat3 (Cell Signaling Technology, 4904S) were used. β-actin (Cell Signaling Technology, 3700S) was used as loading control.

Statistical analysis

GraphPad Prism was used to perform statistical analysis and generate graphs. Data values are presented as means ± s.e.m..

3.6 Figures

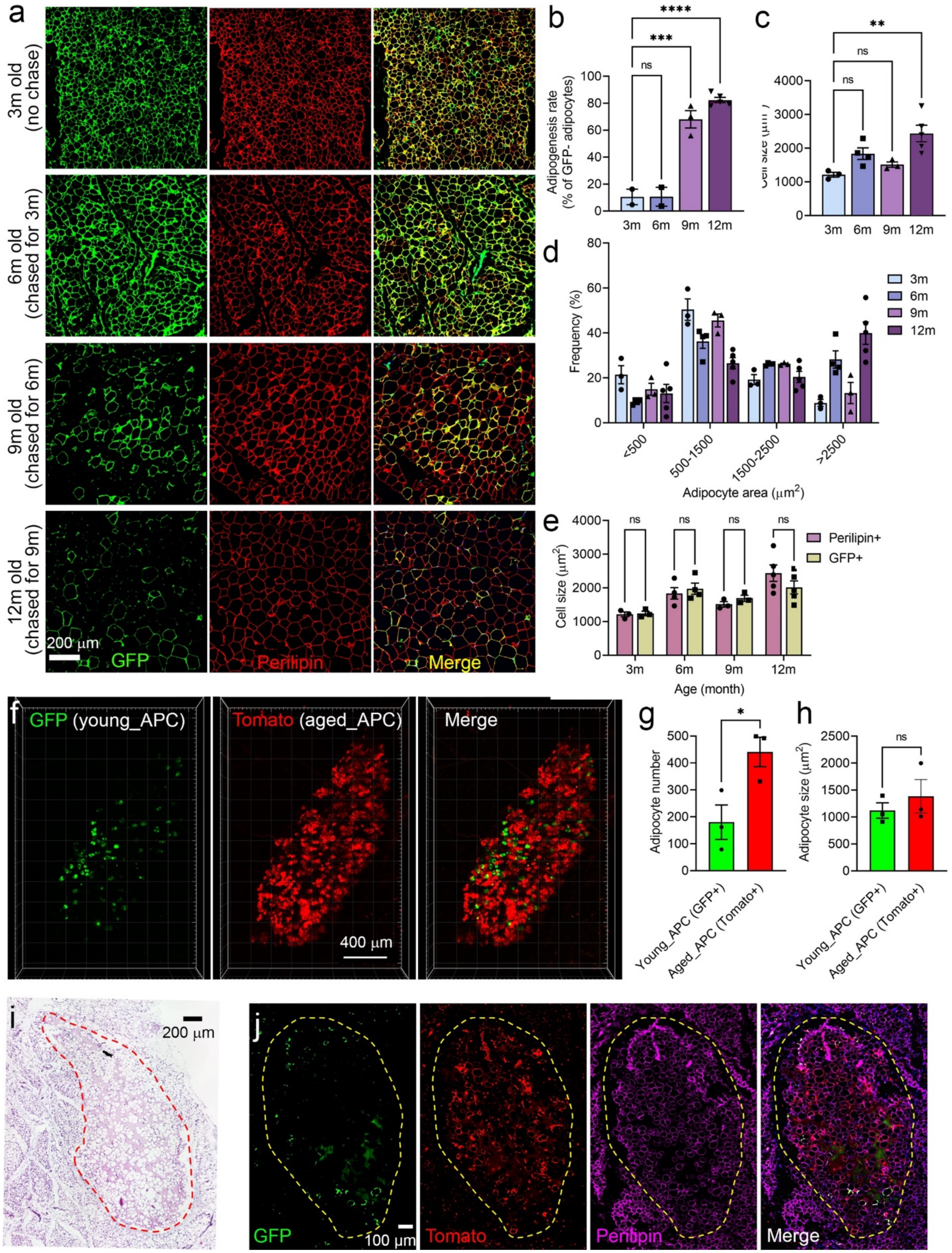
a
3m old (no chase)
6m old (chased for 3m)
9m old (chased for 6m)
12m old (chased for 9m)
200 µm
GFP
Perilipin
Merge
b
Adipogenesis rate (% of GFP- adipocytes)
ns
***
****
3m
6m
9m
12m
c
Cell size (µm²)
ns
ns
**
d
Frequency (%)
<500
500-1500
1500-2500
>2500
Adipocyte area (µm²)
e
Cell size (µm²)
Perilipin+
GFP+
Age (month)
f
GFP (young_APC)
Tomato (aged_APC)
Merge
400 µm
g
Adipocyte number
*
Young_APC (GFP+)
Aged_APC (Tomato+)
h
Adipocyte size (µm²)
ns
i
200 µm
j
GFP
100 µm
Tomato
Perilipin
Merge

Fig 3. 1 **APCs in aged mice have a high adipogenic rate *in vivo*.**

a, Representative GFP and perilipin staining of gWAT samples from the AdipoChaser-mTmG male mice at the indicated ages.

b, New adipogenesis rate (percentage of GFP- adipocytes) of gWAT from the male mice at the indicated ages.

c-e, Mean adipocyte size (c), cell size distribution (d), and comparison between mean cell size of pre-existing adipocytes (GFP+ adipocytes) and all adipocytes (perilipin+ adipocytes) of gWAT from the male mice at the indicated ages.

a-e, n=3, 3-month-old; n=4, 6-month-old; n=3, 9-month-old; n=5, 12-month-old. **p<0.01; ***p<0.005; ****p<0.001; two-way ANOVA. All data represent the mean ± s.e.m.

f, Matrigel plugs of transplant of mixed APCs (Lin-, CD45-CD31-Ter119-) isolated from 2.5-month-old (young) male CAG-EGFP and 12-month-old (aged) Rosa26-mT/mG mice were profiled for 3-dimensional Tomato and GFP signals.

g, h, Quantification of Tomato+ and GFP+ adipocyte number (g) and mean cell size (h). n=3 transplantations. *p<0.05; two-tailed Student's t-test. All data represent the mean ± s.e.m.

i, Hematoxylin and eosin (HE) staining in the transplanted Matrigel plug within the sWAT.

j, Immunofluorescence staining of GFP, Tomato, and Perilipin in the transplanted Matrigel plug.

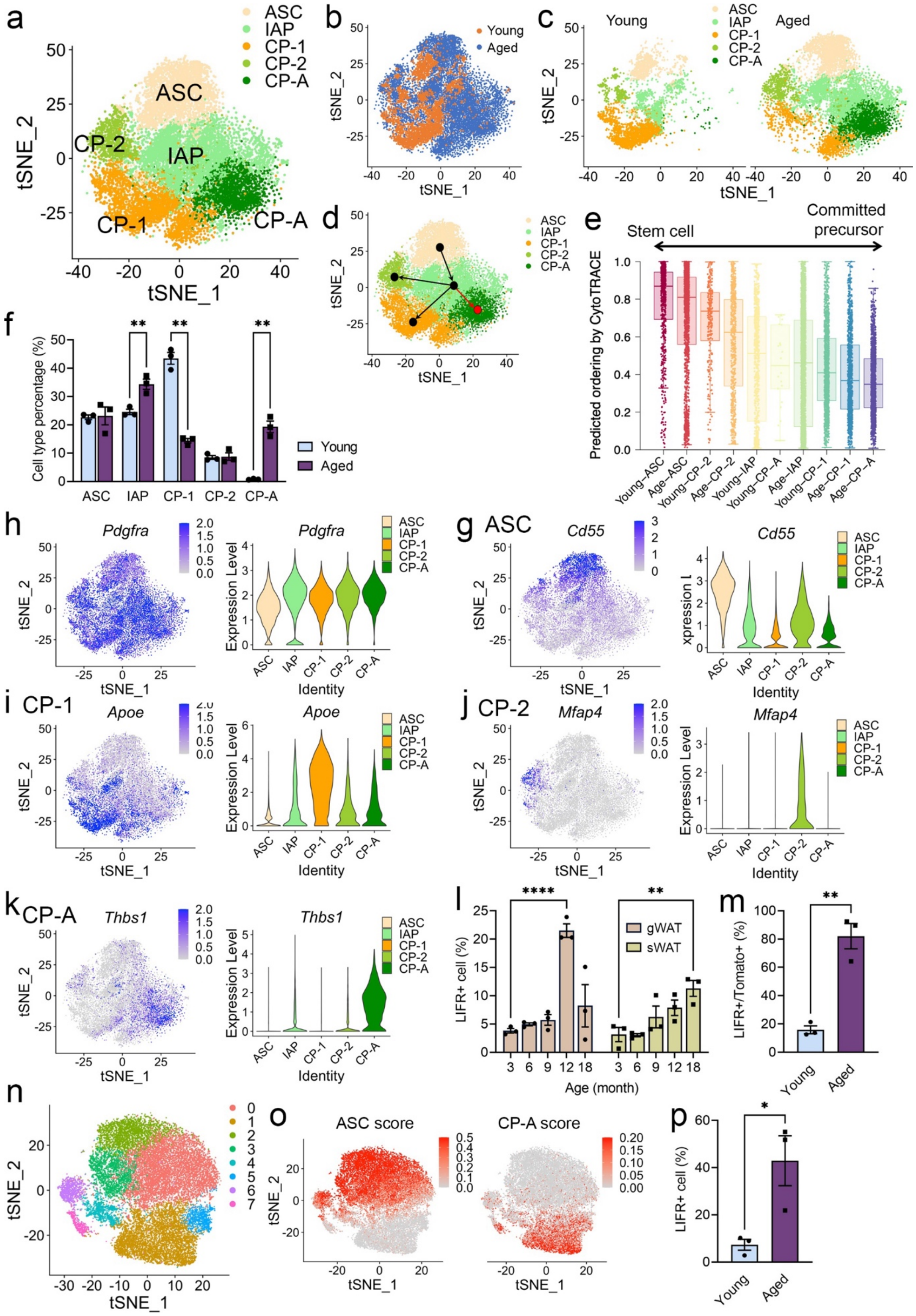

Fig 3. 2 **scRNA-seq analysis identifies a novel, age-specific APC population**

a, Progenitor populations from each group (4,337 "young" and 10,757 "aged" cells) were selected for t-distributed stochastic neighbor embedding (t-SNE) plot. K-means clustering (k=25) was applied to the t-SNE plot to identify five clusters, ASC, IAP, CP-1, CP-2, and CP-A. This data is from a single experiment. n=3 per group.

b, **c**, t-SNE plot showing differences between young and aged adipocyte APCs, indicating the CP-A cluster uniquely exists in the aged group.

D, Slingshot trajectory analysis of five clusters shows a new, age-specific trajectory from ASC to CP-A.

e, Box plot showing median and distribution of CytoTRACE values (modified gene count measure) per APC subtype in young and aged mice. A Higher CytoTRACE value means less differentiated status.

F, The percentage of each cluster in young and aged APCs. N=3 per group. **p<0.01; two-way ANOVA. All data represent the mean ± s.e.m.

g–k, Individual gene t-SNE and violin plots showing the expression and distribution of representative marker genes: general APC marker *Pdgfra* (g), cluster-specific markers *Cd55* for ASC (h), *Apoe* for CP-1 (i), *Mfap4* for CP2 (j), and *Thbs1* for CP-A (k).

l, Flow cytometry analysis of CP-A (LIFR+) cell percentage in the gWAT and sWAT from male mice at indicated ages. n=3 per group. **p<0.01; ****p<0.001; two-way ANOVA. All data represent the mean ± s.e.m.

m, FACS-isolated ASCs (PDGFRα+ DPP4+ cells) from 2.5-month-old (young) or 12-month-old (aged) Rosa26-mT/mG male mice were suspended in Matrigel and transplanted into the sWAT of 2.5-month-old male WT mice (3×10^5 per one sWAT). After 3 days, SVFs from the sWAT with transplanted Matrigel plug were analyzed for differentiated CP-A cells (Tomato+ PDGFRα+ LIFR+). n=3 per group. **p<0.01; two-tailed Student's t-test. All data represent the mean ± s.e.m.

n, The APC populations from 5 human donors were selected for tSNE plot.

o, ASC and CP-A score of clusters in human APCs. The scores calculate the top 20 ASC and CP-A marker genes for each cell.

p, Flow cytometry analysis shows the percentage of LIFR+ populations within the PDGFRα+ population in each peripancreatic WAT sample from men of different ages. n=3 per group. *p<0.1; distribution-free one-sided Wilcoxon rank sum test. All data represent the mean ± s.e.m.

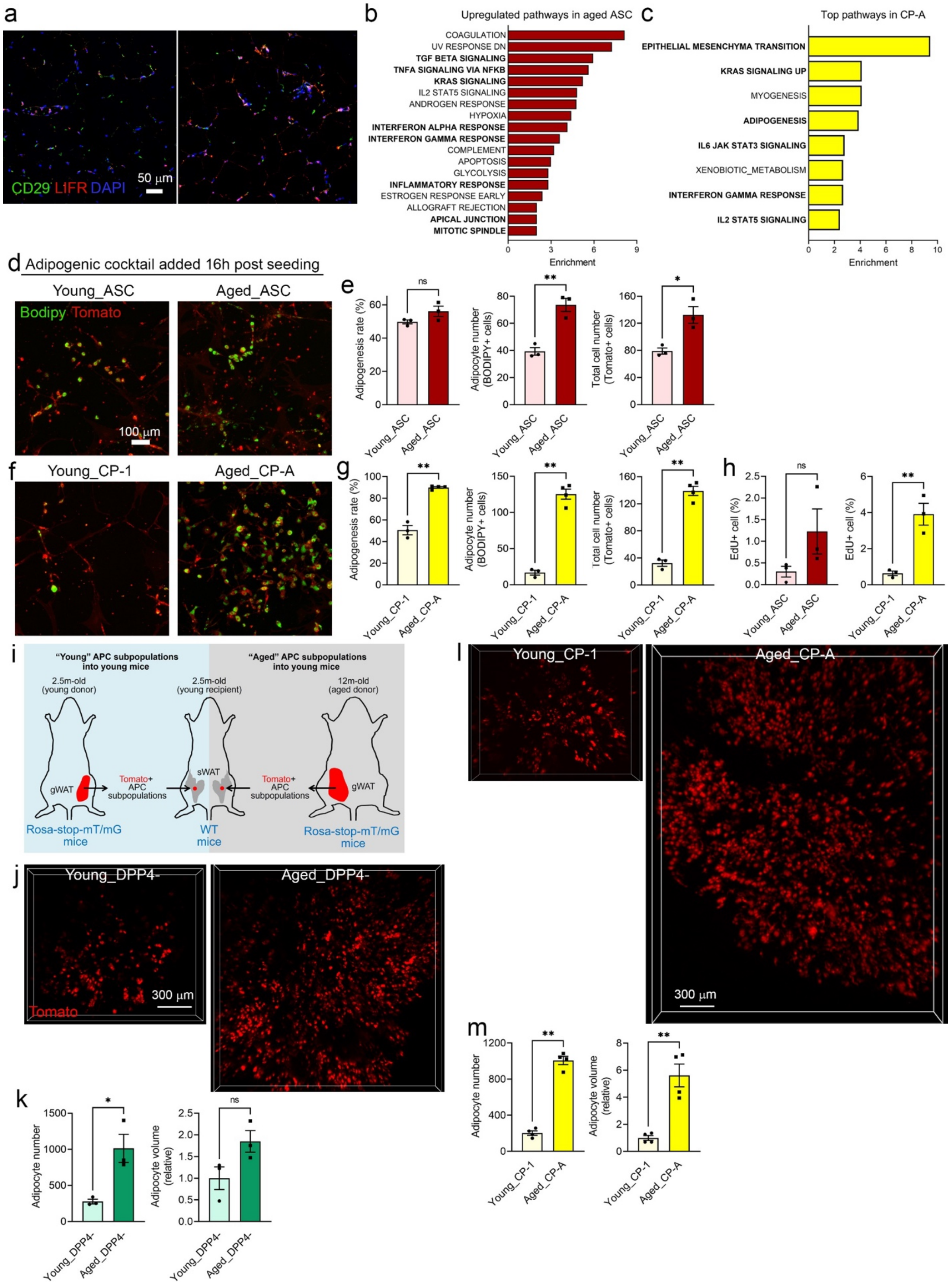

Fig 3. 3 **CP-A cells are highly proliferative and adipogenic *in vitro* and *in vivo***
a, Immunofluorescence staining of CD29 and LIFR in peripancreatic WAT sample from men of different ages (left: 29-year-old, right: 64-year-old).

b, Top upregulated pathways in “aged” ASCs compared to “young” ASCs.

c, Top pathways in the age-specific CP-A population.

Enrichment score (b and c): Number of overlapped genes/number of genes in our cell type specific gene set × 20000/number of genes in the pathway. Pathway source: HALLMARK. Statistic cut off: FDR<0.05

d, f, Young ASC and CP-1 populations were enriched from the SVFs isolated from the gWAT of 2.5-month-old (young) male Rosa26-mT/mG mice; aged ASC and CP-A populations were enriched from the SVFs isolated from the gWAT of 12-month-old (aged) male Rosa26-mT/mG mice. For each APC population, 1 × 10^4 cells were suspended in Matrigel and seeded in tissue culture dishes. 16 hours later, the adipogenic cocktail was added to induce APC differentiation. Cells were imaged 6 days later with BODIPY labeling lipid droplets**.** Representative confocal fluorescent images show Tomato+ cells and GFP+ cells (adipocytes are positive for BODIPY staining) from the young and aged ASC populations (d), young CP-1 population and aged CP-A population (f).

e, **g**, Quantification of adipogenesis rate, adipocyte number (GFP+ cells), and total cell number (Tomato+ cells). e, n=3 per group; g, young, n=3; aged, n=4.

h, Flow cytometry analysis of EdU+ proliferating cell percentage in young ASC, aged ASC, CP-1, and CP-A populations.

i, Young DPP4- (none ASC APCs) and CP-1 populations were enriched from the SVFs isolated from the gWAT of 2.5-month-old (young) male Rosa26-mT/mG mice. Aged DPP4- (none ASC APCs) and CP-A populations were enriched from the SVFs isolated from the gWAT of 12-month-old (aged) male Rosa26-mT/mG mice. For each APC population, 2×10^4 cells were enriched. Each enriched APC population was suspended in Matrigel and transplanted into the sWAT of 2.5-month-old WT male mice. Young and aged DPP4- populations were transplanted into either side of the sWATof the same 2.5-month-old male WT mice. Young CP-1 and aged CP-A populations were transplanted into either side of the sWATof the same 2.5-month-old male WT mice.

j, l, Dissected Matrigel plugs were profiled for 3-dimensional Tomato signals.

k, Quantification of Tomato+ adipocyte number generated from young and aged DPP4- cells. n=3 transplantations.

m, Quantification of Tomato+ adipocyte number generated from young CP-1 and Aged CP-A cells. n=4 transplantations.

*$p<0.05$; **$p<0.01$; two-tailed Student's t-test. All data represent the mean ± s.e.m.

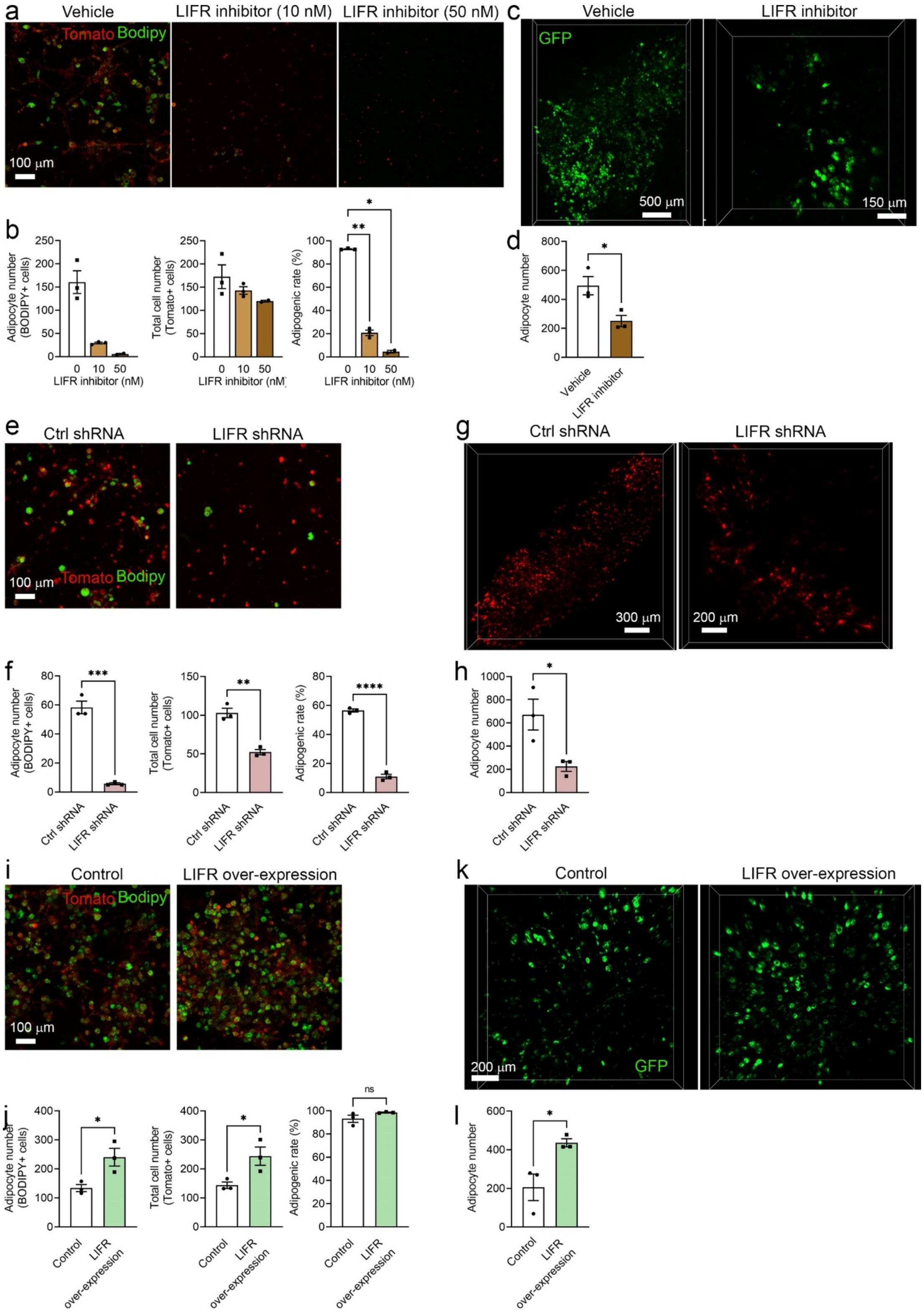

Fig 3. 4 The high adipogenic capacity of CP-A cells is dependent on LIFR

a, CP-A cells were isolated from the gWAT of 12-month-old (aged) male Rosa26-

mT/mG mice. 1 × 10^4 cells were suspended in Matrigel and seeded in tissue culture dishes. 16 hours later, the adipogenic cocktail was added to induce APC differentiation with or without LIFR inhibitor EC359 at indicated concentrations. Cells were imaged 6 days later with BODIPY labeling lipid droplets.

b, Quantification of adipogenesis rate, adipocyte number (GFP+ cells), and total cell number (Tomato+ cells). n=3 per group. *p<0.05; **p<0.01; two-way ANOVA. All data represent the mean ± s.e.m.

c, CP-A cells were isolated from the gWAT of 12-month-old (aged) male CAG-EGFP mice. 2 × 10^4 cells were suspended in Matrigel and transplanted into the sWAT of 2.5-month-old WT male mice. Recipient mice were treated with vehicle or LIFR inhibitor EC359 at 5mg/kg s.c. 3 times per week. Matrigel plugs were dissected and profiled for 3-dimensional GFP signal 2 weeks after transplantation.

d, Quantification of GFP+ adipocyte number generated from EC359-treated CP-A transplants. n=3 transplantations. *p<0.05; two-tailed Student's t-test. All data represent the mean ± s.e.m.

e, Lin- (CD45- CD31- Ter119-) SVFs isolated from the gWAT of 12-month-old (aged) male Rosa26-mT/mG mice were transfected with control or LIFR shRNA lentiviral particles. 5 × 10^3 cells were suspended in Matrigel and seeded in tissue culture dishes. 16 hours later, the adipogenic cocktail was added to induce APC differentiation. Cells were imaged 6 days later with BODIPY labeling lipid droplets.

f, Quantification of adipogenesis rate, adipocyte number (GFP+ cells), and total cell number (Tomato+ cells). n=3 per group. **p<0.01; ***p<0.005; ****p<0.001; two-tailed Student's t-test. All data represent the mean ± s.e.m.

g, Lin- (CD45- CD31- Ter119-) SVFs isolated from the gWAT of 12-month-old (aged) male Rosa26-mT/mG mice were transfected with ctrl or LIFR shRNA lentiviral particles. 2 × 10^4 cells were suspended in Matrigel and transplanted into the sWAT of 2.5-month-old WT male mice. Matrigel plugs were dissected 2 weeks after transplantation and profiled for 3-dimensional Tomato signal.

h, Quantification of Tomato+ adipocyte number generated from LIFR-knockdown transplants. n=3 per group. *p<0.05; two-tailed Student's t-test. All data represent the mean ± s.e.m.

i, Lin- (CD45- CD31- Ter119-) SVFs isolated from the gWAT of 2.5-month-old (young) male Rosa26-mT/mG mice were transfected with ctrl or LIFR over-expression lentiviral particles. 2 × 10^4 transfected cells were suspended in Matrigel and seeded in tissue culture dishes. 16 hours later, the adipogenic cocktail was added to induce APC differentiation. Cells were imaged 6 days later with BODIPY labeling lipid droplets.

j, Quantification of adipogenesis rate, adipocyte number (GFP+ cells), and total cell number (Tomato+ cells). n=3 per group. *p<0.05; two-tailed Student's t-test. All data represent the mean ± s.e.m.

k, Lin- (CD45- CD31- Ter119-) SVFs isolated from the gWAT of 2.5-month-old (young) male CAG-EGFP mice were transfected with control or LIFR over-expression lentiviral particles. 2 × 10^4 transfected cells were suspended in Matrigel and transplanted into the sWAT of 2.5-month-old WT male mice. Matrigel plugs were dissected 2 weeks after transplantation and profiled for 3-dimensional GFP signal.

l, Quantification of GFP+ adipocyte number generated from LIFR over-expression transplants. n=3 per group. *p<0.05; two-tailed Student's t-test. All data represent the mean ± s.e.m.

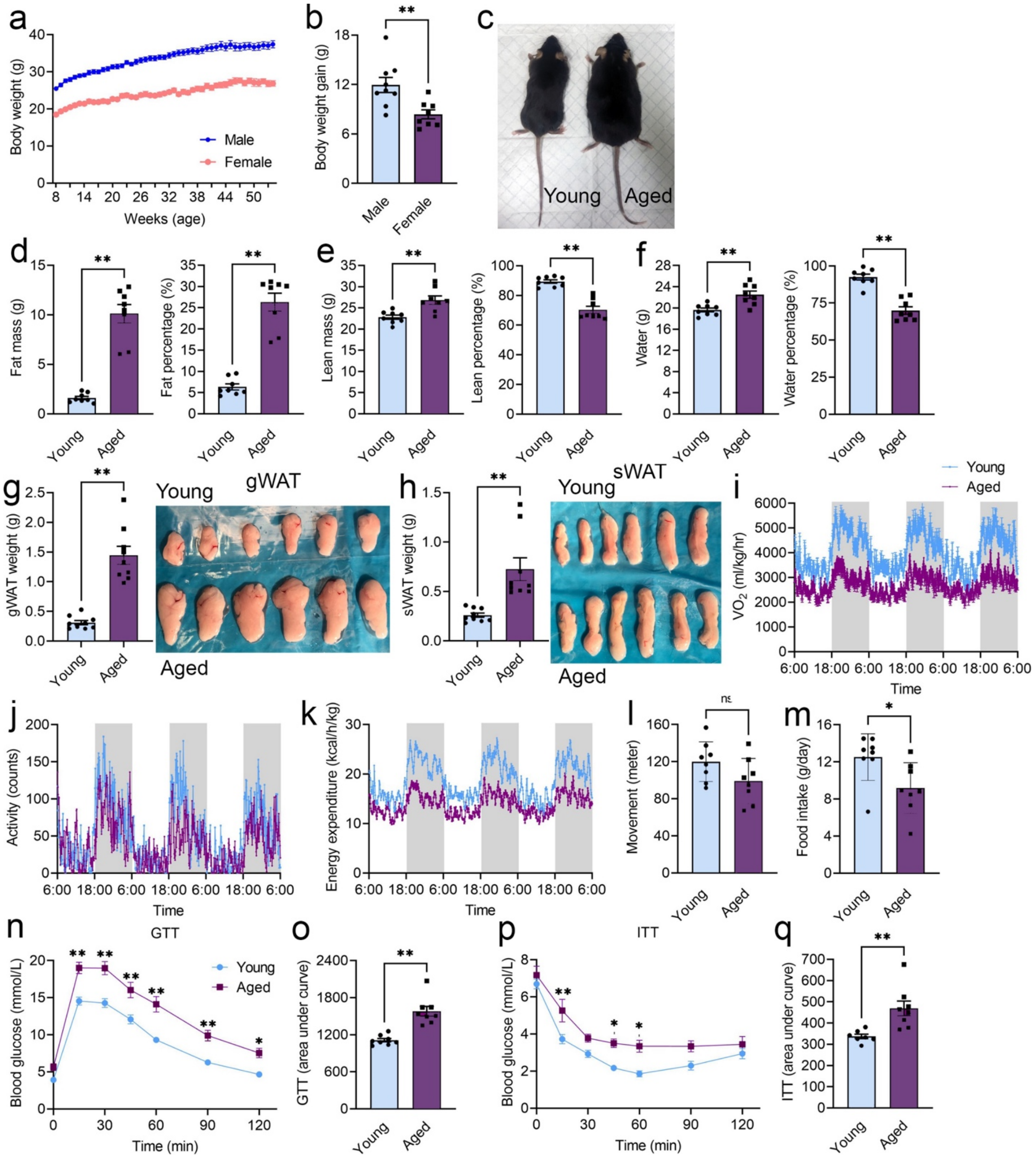

Sup Fig 3. 1 Aged mice display substantial fat gain and reduced metabolic rate
a, **b**, Body weight curve (a) and body weight gain (b) of male and female C57BL/6J mice from 8-week-old to 54-week-old (n=9 male mice; n=8 female mice).

c, Images of young (2.5-month-old) and aged (12-month-old) male mice.

d-f, Magnetic resonance imaging (MRI) was used to measure fat mass (d), lean mass (e), and water content (f) (n=8 mice per age group).

g, h, Tissue weight and whole-tissue pictures of gWAT (e) and sWAT (f). n=9 mice per each age group.

i–m, Metabolic cage studies; oxygen consumption (i), physical activity (j), energy expenditure (k), total distance (l), and food intake (m), were determined for young and aged mice. n=8 mice per age group.

n–q, GTT (n, o) and ITT (p, q) were performed on young (2.5-month-old) and aged (12-month-old) mice. For GTT, n=8 per age group; for ITT, n=7, young; n=8, aged.

b, d–f, g, h, l, m, o, q, *$p<0.05$; **$p<0.01$; two-tailed Student's t-test. n, p, *$p<0.05$; **$p<0.01$; Two-way ANOVA. All data represent the mean ± s.e.m.

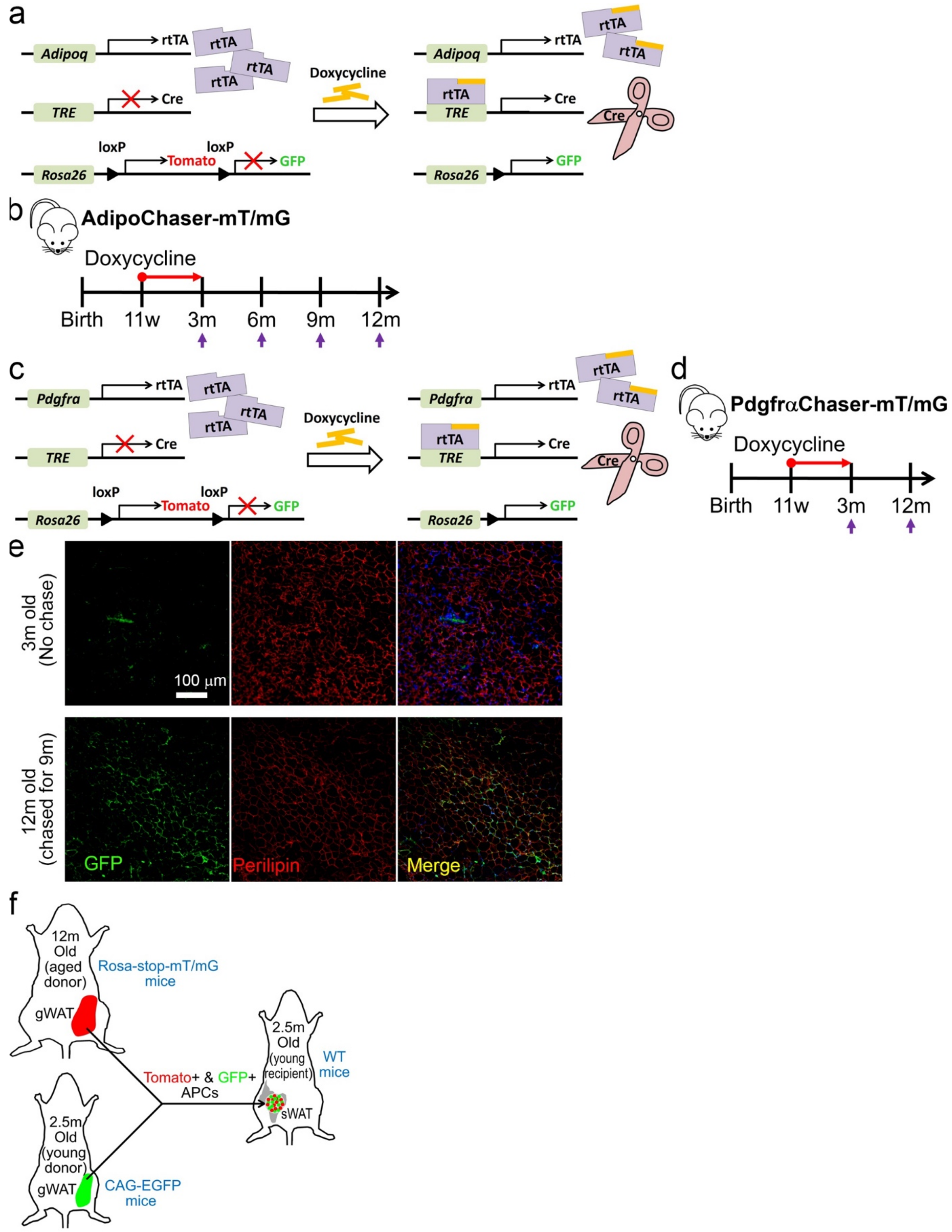

Sup Fig 3. 2 Aged mice show new adipogenesis in gWAT

a, Doxycycline-inducible, adipocyte-specific labeling of mature adipocytes by the

AdipoChaser mouse model. The doxycycline (dox)-based, tet-responsive, Cre-loxP "pulse-chase" labeling system is derived from interbreeding three transgenic strains: 1) mice expressing the "tet-on" transcription factor rtTA under the adiponectin promoter (Adn-rtTA); 2) mice expressing tet-responsive CRE (TRE-Cre) that is activated by rtTA in the presence of dox; and 3) reporter mice expressing membrane located tdTomato or GFP reporter gene from the Rosa26 locus in a Cre-dependent manner (Rosa26-l loxP-mtdTomato-loxP-mGFP, mT/mG). This model allows labeling of pre-existing adipocytes as GFP+ cells by dox treatment, tracking the fate of these cells, and identification of newly generated adipocytes (GFP- adipocytes) post dox treatment.

b, Experimental design for Fig. 1a. 3-month-old male AdipoChaser-mTmG mice were fed with a doxycycline diet for 1 week to ensure a uniform and permanent labeling of all mature adipocytes, followed by a standard chow diet for 3, 6, or 9 months.

c, Doxycycline-inducible, labeling of Pdgfra+ mural cells by the PdgfraChaser mouse model. This model allows tracking the fate of Pdgfra+ cells post dox treatment.

d, Experimental design: 3-month-old male PdgfrαChaser-mTmG mice were fed with a doxycycline diet for 1 week to ensure a uniform and permanent labeling of all PDGFRα+ cells, followed by a standard chow diet for 9 months.

e, GFP (green) and perilipin (red) immunofluorescence staining in gWAT of young (3-month-old) and aged (12-month-old) PdgfrαChaser-mTmG male mice. These images are representative of two independent experiments.

f, Experimental design for Fig. 1f. APCs (Lin-, CD45- CD31- Ter119-) were enriched from isolated SVFs from both 2.5-month-old (young) male CAG-EGFP and 12-month-old (aged) Rosa26-mT/mG mice. An equal number of GFP+ and Tomato+ cells (1 ×

10^5) were mixed together and suspended in Matrigel. The cell mixture was transplanted into the sWAT of 2.5-month-old male WT mice.

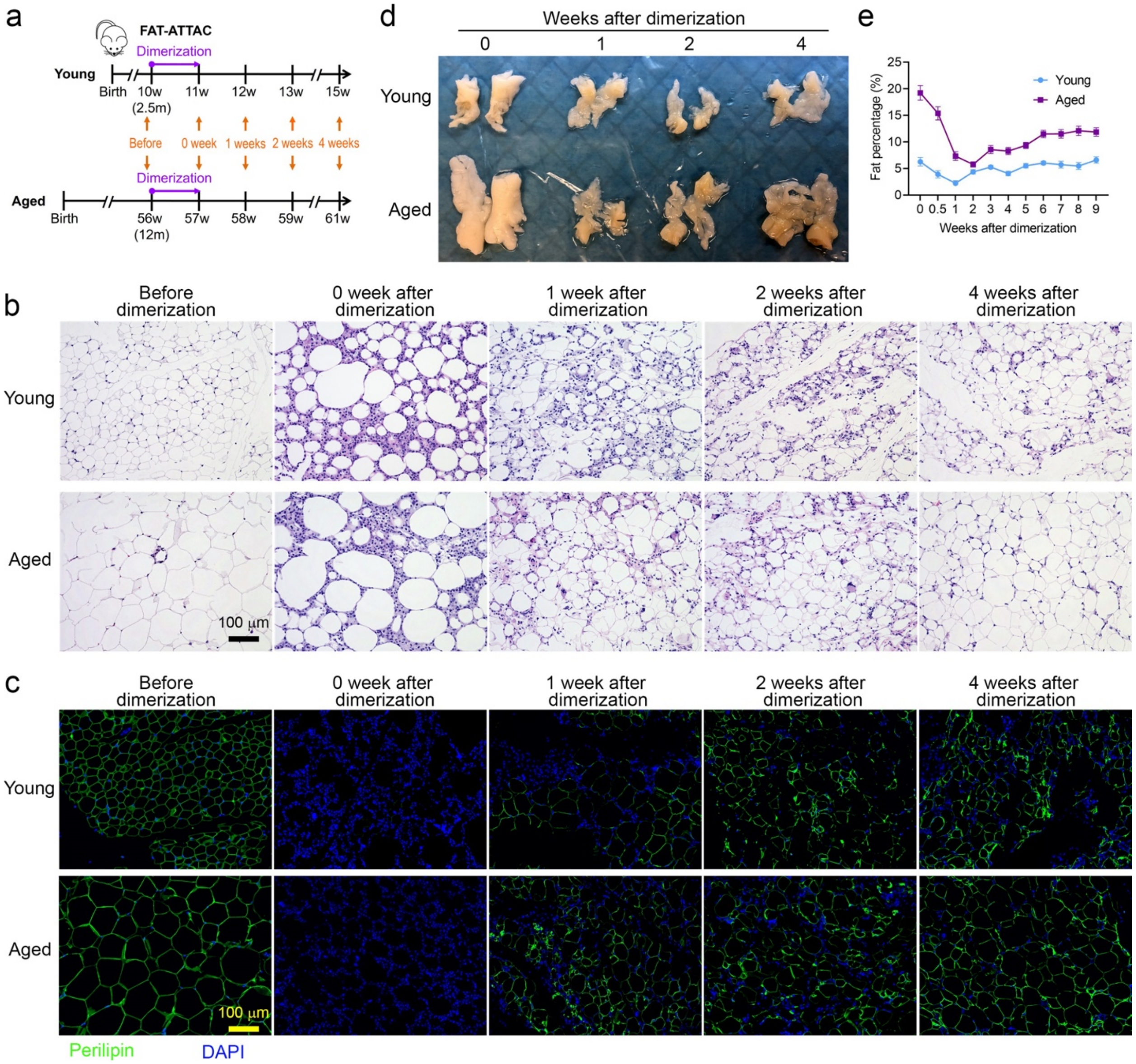

Sup Fig 3. 3 Aged mice exhibit high adipocyte regeneration capacity

a, Experimental design: young or aged FAT-ATTAC mice were dimerized daily for seven days, and gWAT samples were collected before, or 0, 1, 2, 4 weeks after dimerization.

b, Hematoxylin and eosin (HE) staining in gWAT of young (2.5-month-old) and aged (12-month-old) FAT-ATTAC mice before and after dimerization. These images are representative of two independent experiments.

c, Perilipin (green) and DAPI (blue) immunofluorescence staining in gWAT of young (2.5-month-old) and aged (12-month-old) FAT-ATTAC mice before and after dimerization. These images are representative of two independent experiments.

d, Whole-tissue images of gWAT from young (2.5-month-old) and aged (12-month-old) FAT-ATTAC mice after dimerization.

e, Magnetic resonance imaging (MRI) was used to measure fat percentage for 9 weeks after dimerization. Young, n=6; aged, n=9.

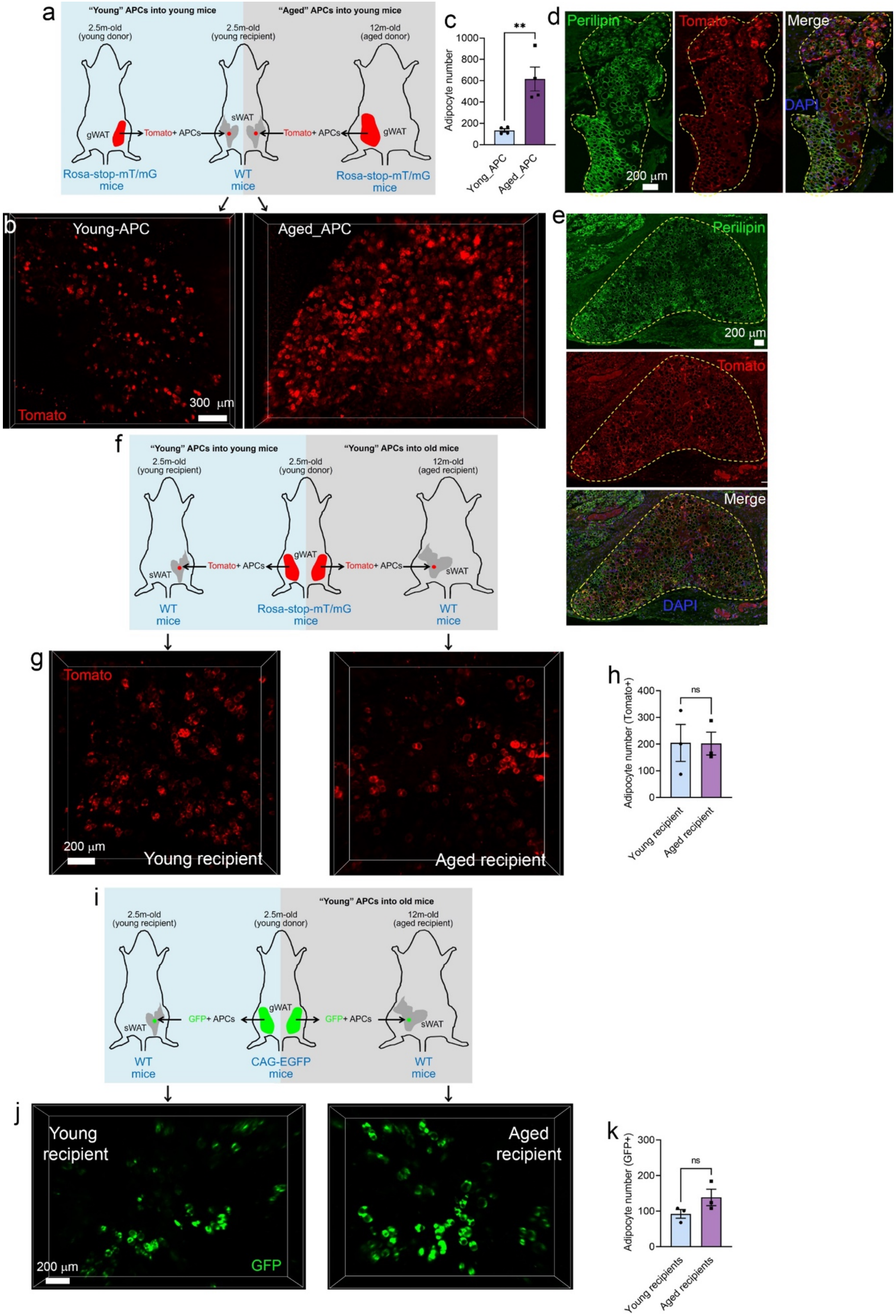
a
"Young" APCs into young mice
"Aged" APCs into young mice
2.5m-old (young donor)
2.5m-old (young recipient)
12m-old (aged donor)
gWAT
Tomato+ APCs
sWAT
Rosa-stop-mT/mG mice
WT mice
c
**
Adipocyte number
1000
800
600
400
200
0
Yong_APC
Aged_APC
d
Perilipin
Tomato
Merge
DAPI
200 µm
b
Young-APC
Aged_APC
Tomato
300 µm
e
Perilipin
200 µm
Tomato
Merge
DAPI
f
"Young" APCs into young mice
"Young" APCs into old mice
2.5m-old (young recipient)
2.5m-old (young donor)
12m-old (aged recipient)
sWAT
gWAT
Tomato+ APCs
WT mice
Rosa-stop-mT/mG mice
g
Tomato
200 µm
Young recipient
Aged recipient
h
Adipocyte number (Tomato+)
400
300
200
100
0
ns
Young recipient
Aged recipient
i
"Young" APCs into old mice
2.5m-old (young recipient)
2.5m-old (young donor)
12m-old (aged recipient)
sWAT
gWAT
GFP+ APCs
WT mice
CAG-EGFP mice
j
Young recipient
Aged recipient
200 µm
GFP
k
Adipocyte number (GFP+)
300
200
100
0
ns
Young recipients
Aged recipients

Sup Fig 3. 4 Aged microenvironment does not promote adipogenesis of APCs in young mice

a, APCs (Lin-, CD45-CD31-Ter119-) were enriched from isolated SVFs from both 2.5-month-old (young) or 12-month-old (aged) Rosa26-mT/mG mice. These Tomato+ cells (1×10^5) were suspended in Matrigel. The cell mixture was transplanted into either side of the sWAT of the same 2.5-month-old male WT mice.

b, Dissected Matrigel plugs were profiled for 3-dimensional Tomato signal.

c, Quantification of Tomato+ adipocyte number. n=4 per group. **p<0.01; two-tailed Student's t-test. All data represent the mean ± s.e.m.

d, e, Immunofluorescence staining of Tomato and Perilipin in the transplanted Matrigel plugs of young (d) and aged (e) APCs.

f, APCs (Lin-, CD45-CD31-Ter119-) were enriched from isolated SVFs from 2.5-month-old (young) male mT/mG mice. 1×10^5 cells were suspended in Matrigel and transplanted into the sWAT of 2.5-month-old (young) or 12-month-old (aged) male WT mice.

g, Dissected Matrigel plugs were profiled for 3-dimensional Tomato signal.

h, Quantification of Tomato+ adipocyte number. n=3 per group. two-tailed Student's t-test. All data represent the mean ± s.e.m.

i, Similar experiments were performed using Lin- (CD45-CD31-Ter119-) SVFs isolated from 2.5-month-old (young) male CAG-EGFP mice.

j, Dissected Matrigel plugs were profiled for 3-dimensional GFP signal.

k, Quantification of GFP+ adipocyte number. n=3 per group. two-tailed Student's t-test. All data represent the mean ± s.e.m.

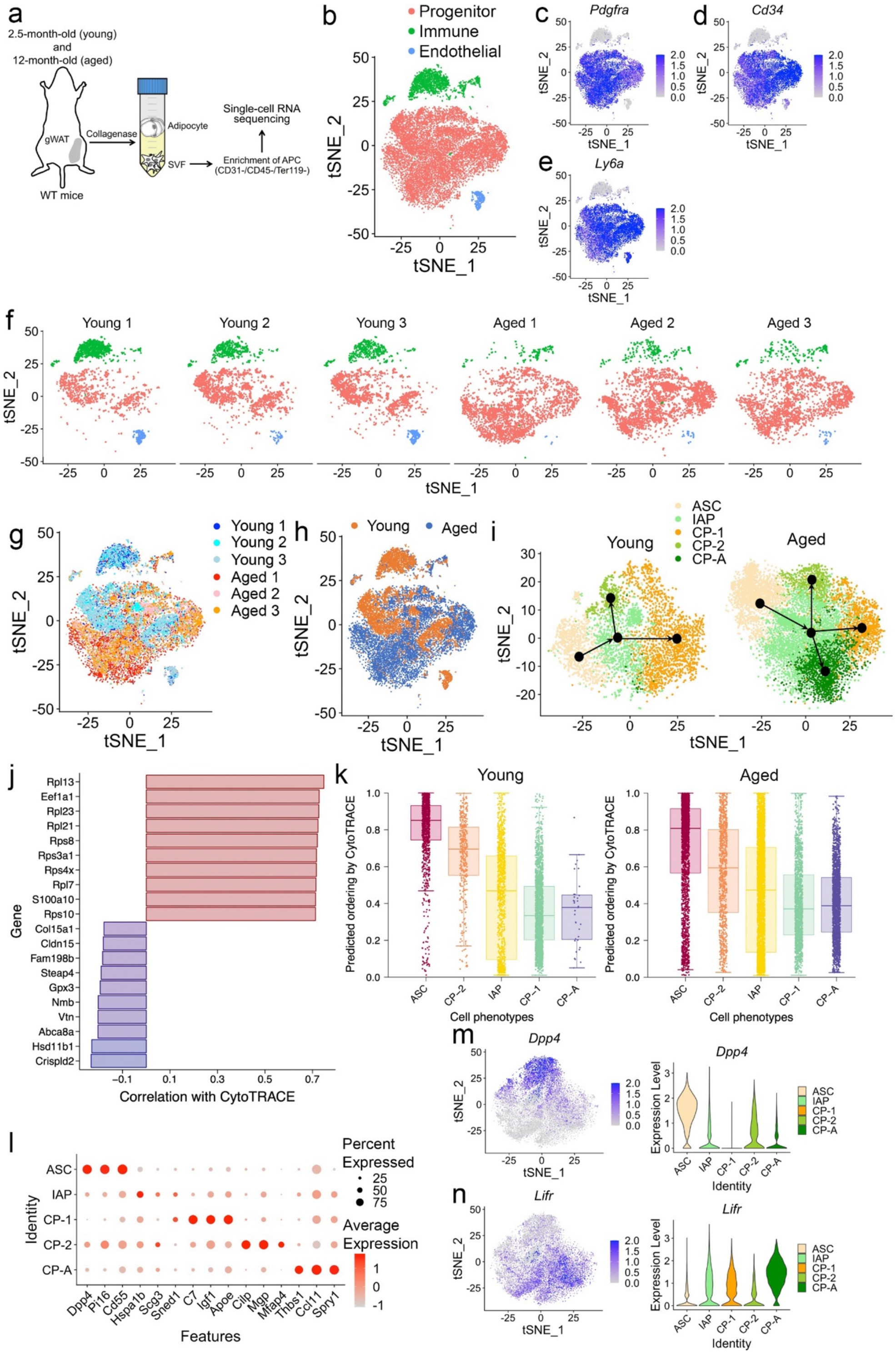

Sup Fig 3. 5 scRNA-seq of Lin- SVFs in gWAT of young and aged male mice.
a, Lin- (CD45-CD31-Ter119-) SVFs isolated from gWAT of 2.5-month-old (young) and 12-month-old (age) male WT mice were used for scRNA-seq.

b, t-SNE plot of 19534 cells in three major cell clusters: progenitor cells, immune cells, and endothelial cells

c-e, t-SNE plots showing expression and distribution of stem cell marker genes *Pdgfrα* (c), *Cd34* (d), and *Ly6a* (e).

f, Lin- SVFs from each mouse (2,199 cells from "young 1", 2,394 cells from "young 2", 2,539 cells from "young 3", 5,150 cells from "aged 1", 4,109 cells from "aged 2", and 3,072 cells from "aged 3") are illustrated in the t-SNE plot.

g, h, t-SNE plots showing differences between young and aged Lin- SVFs. Cells were labeled with different colors for each individual sample (n=3) (g), or cells were labeled with different colors for different age groups (h).

i, Slingshot trajectory analysis of five APC clusters in each age group, showing an age-specific trajectory from ASC to CP-A in the aged group.

j, Bar plot shows the top 10 (less differentiated; red) and bottom 10 (most differentiated; blue) genes in this dataset based on their correlation with CytoTRACE values.

k, Box plot showing the median and distribution of CytoTRACE values (modified gene count measure) per APC population in young and aged mice, separately.

l, Dot plot showing the scaled average expression of the top three marker genes in each APC cluster (young and aged combined).

m, n, Individual gene t-SNE and violin plots, showing the expression and distribution of the ASC marker Dpp4 (m), and the CP-A marker Lifr (n).

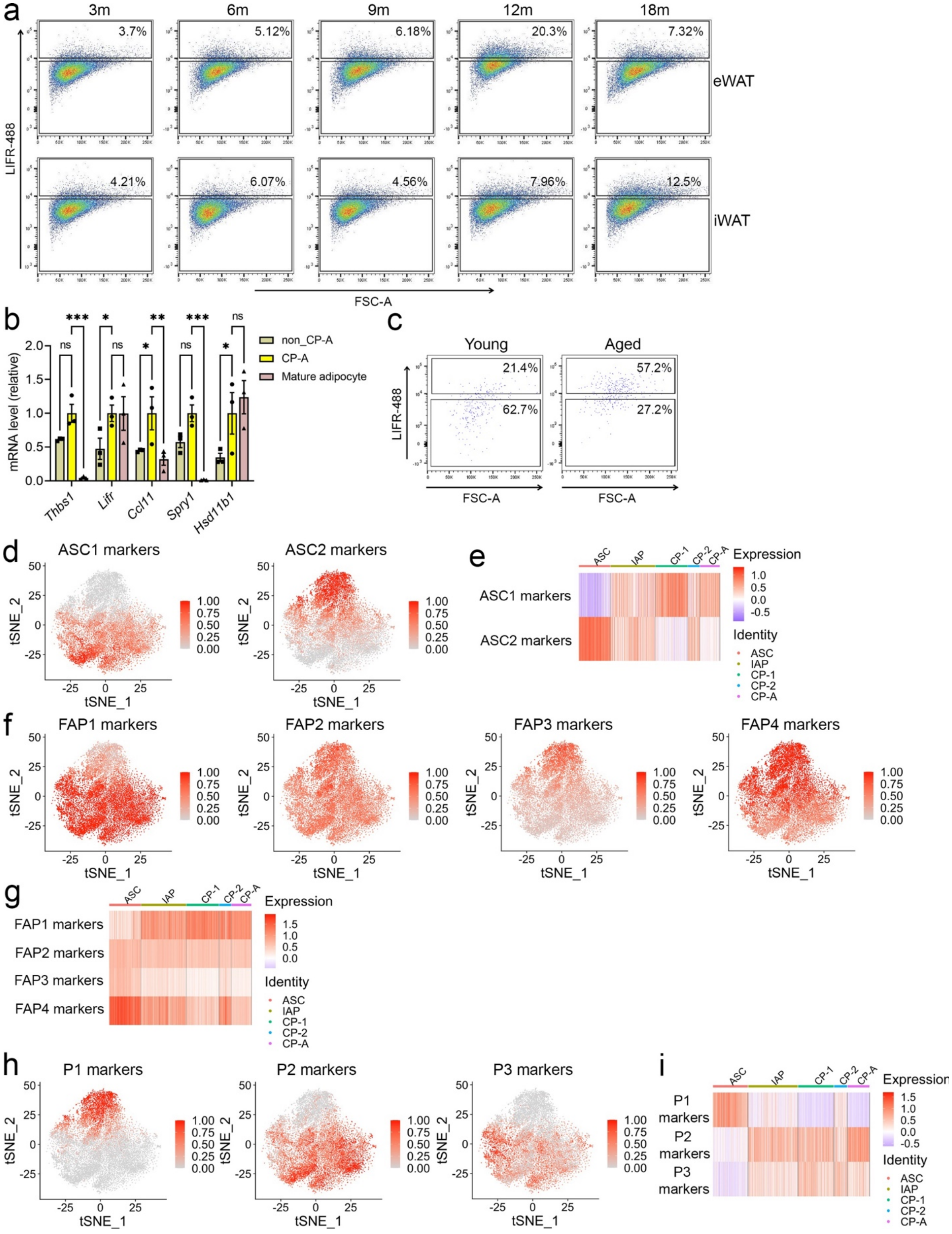

Sup Fig 3. 6 Comparison of ACS, IAP, CP-1, CP-2, and CP-A populations with previously identified APC populations

a, Representative flow cytometry plots for Fig. 2l of LIFR+ cell percentage in total PDGFRα+ APCs in the gWAT and sWAT from male mice at indicated ages.

b, Real-Time PCR analysis shows mRNA levels of representative CP-A marker genes.

c, Representative flow cytometry plots for Fig. 2m of LIFR+ cell percentage in total transplanted Tomato+ cells.

d, t-SNE plot showing gene module scores of the top 50 markers of ASC1 and ASC2 as reported by Burl et al. in eWAT from 2.5-month-old (young) or 12-month-old (aged) male WT mice.

e, Heatmap of gene module scores by group identities with the 50 top cluster markers as reported by Burl et al.

f, t-SNE plot showing gene module scores of the top 50 markers of FAP1-4 as reported by Sárvári et al. in eWAT from 2.5-month-old (young) or 12-month-old (aged) male WT mice.

g, Heatmap of gene module scores by group identities with the 50 top cluster markers as reported by Sárvári et al..

h, t-SNE plot showing gene module scores of the top 50 markers of P1-3 as reported by Schwalie et al. in sWAT from 2.5-month-old (young) or 12-month-old (aged) male WT mice.

i, Heatmap of gene module scores by group identities with the 50 top cluster markers as reported by Schwalie et al.

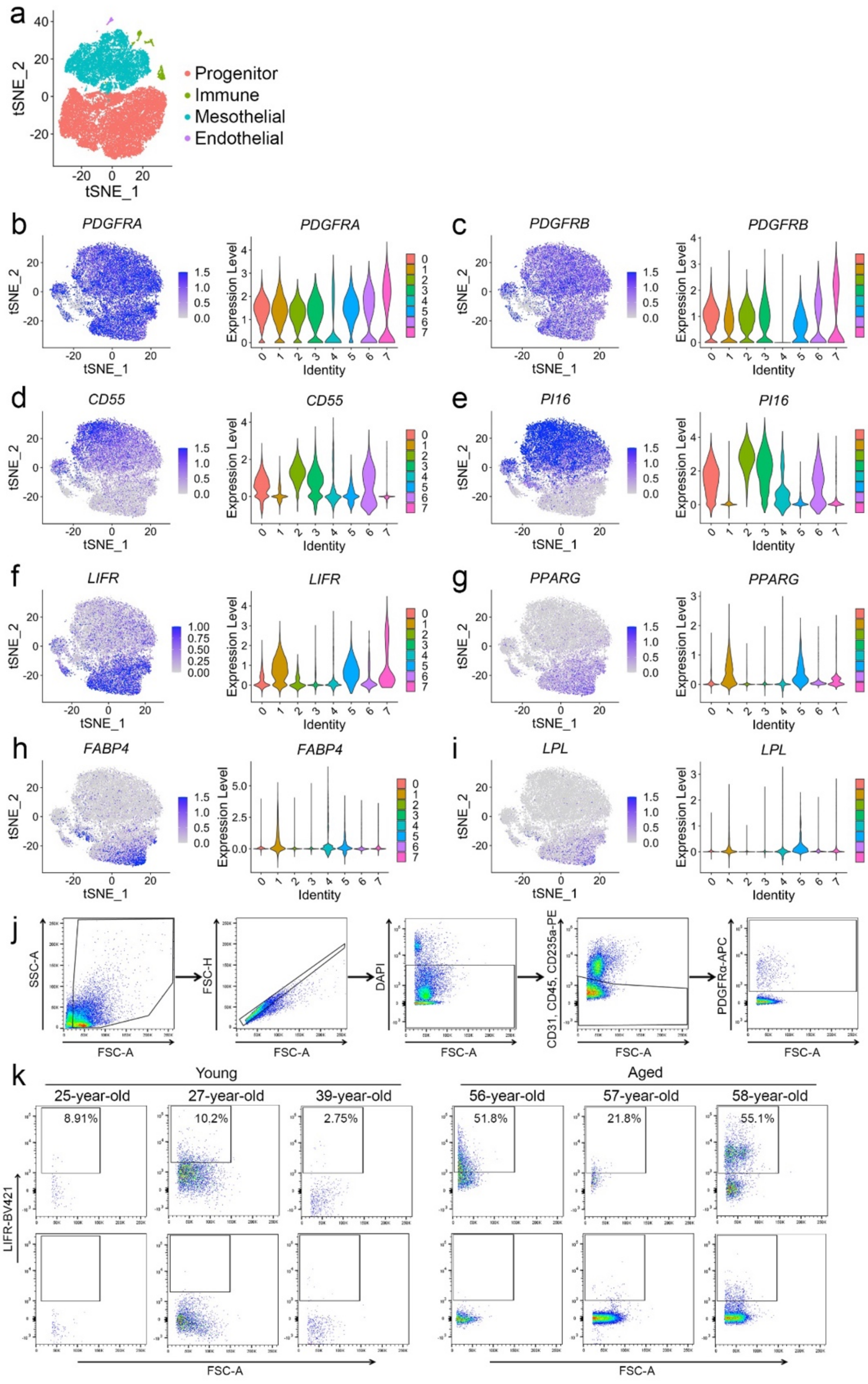

Sup Fig 3. 7 Single-cell RNA-seq analysis of human APCs

a, t-SNE plot of 24794 human pWAT cells in four major cell clusters, progenitor cells, immune cells, mesothelial cells and endothelial cells with k-means clustering (k-means=25).

b–i, Individual gene t-SNE plots showing the expression levels of the indicated genes: adipocyte stem cell/progenitor markers *Pdgfra* (b) and *Pdgfrb* (c), ASC markers *Cd55* (d), and *Pi16* (e), CP-A marker *Lifr* (f), and committed preadipocyte markers *Pparg* (g), *Fabp4* (h), and *Lpl* (i).

j, Flow cytometry strategy for identifying PDGFRα+ cells in Fig. 2p. Single cells were selected based on forward and side scatter profiles. Live cells were gated as DAPI-. Immune cells, endothelial cells, and erythrocytes were gated out using CD45, CD31, and CD235a antibodies.

k, Flow cytometry plots of LIFR+ cells in each human sample with FMO controls for Fig. 2p.

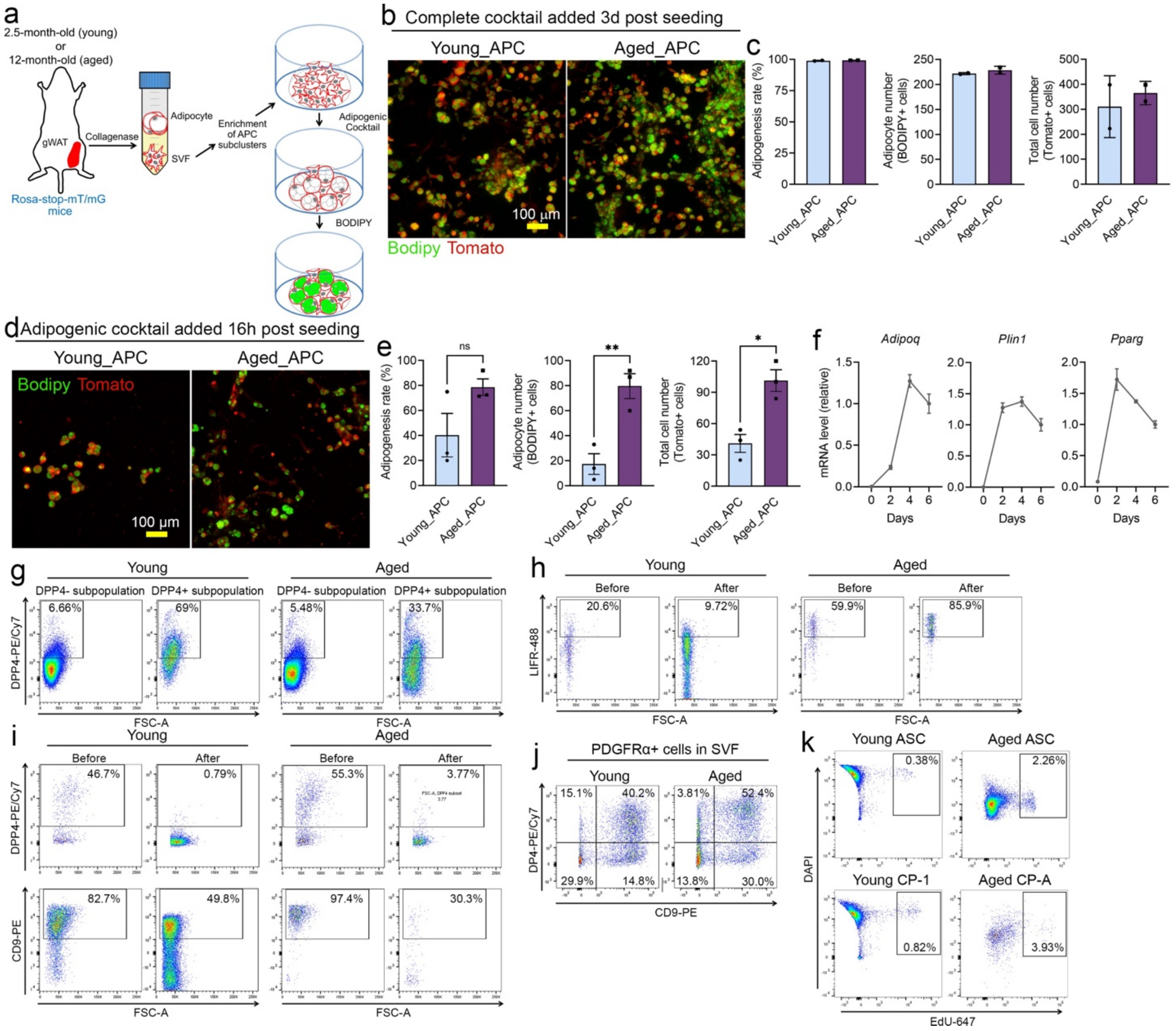

Sup Fig 3. 8 Enriching APC populations and *in vitro* 3D culture of APCs

a, APCs (Lin-, CD45- CD31- Ter119-) were enriched from isolated SVFs from both 2.5-month-old (young) and 12-month-old (aged) Rosa26-mT/mG male mice. 1×10^4 cells were suspended in Matrigel and seeded in tissue culture dishes. The adipogenic cocktail was added 3 days post seeding. Other experimental conditions are the same as described in Fig. 3d

b, Representative confocal fluorescence images of Total APCs (Tomato+ cells) and differentiated adipocytes (Bodipy+ cells).

c, Quantification of adipogenesis rate, adipocyte number (Bodipy+ cells), and total cell number (Tomato+ cells). n=2 per group. All data represent the mean ± s.e.m.

c, Representative confocal fluorescent images show young and aged Lin- (CD45-CD31-Ter119-) total APCs (Tomato+ cells) and adipocytes (Bodipy+ cells). The adipogenic cocktail was added 16 hours post seeding. Other experimental conditions are the same as described in Fig. 3c.

e, Quantification of adipogenesis rate, adipocyte number (GFP+ cells), and total cell number (Tomato+ cells). n=3 per group. *p<0.05; **p<0.01; two-tailed Student's t-test. All data represent the mean ± s.e.m.

f, Real-Time PCR analysis shows mRNA level of adipogenesis-related genes in CP-A cells treated with adipogenic cocktail.

g, DPP4+ population was enriched by magnetic bead-associated cell sorting (MACS). Flow cytometry analysis validates the isolation of DPP4+ and DPP4- populations within the Lin- (CD45-CD31-Ter119-) SVF after MACS in 2.5-month-old (young) or 12-month-old (aged) male WT mice.

h, CP-1 and CP-A populations were enriched through MACS-based negative selection, depleting DPP4+ ASC, CD9+ CP-2 and IAP populations in Lin- SVFs. Flow cytometry analysis validates increased LIFR+ cell percentage in enriched CP-A population after MACS.

i, Flow cytometry analysis validates depletion of DPP4+ and CD9+ populations from the enriched CP-A population after MACS from 2.5-month-old (young) or 12-month-old (aged) male WT mice.

j, Flow cytometry analysis shows DPP4+ and CD9+ population percentages in PDGFRα+ eWAT SVFs from 2.5-month-old (young) or 12-month-old (aged) male WT mice.

k, Representative flow cytometry plots of EdU+ proliferating cells in ASC, CP-1, and CP-A populations from 2.5-month-old (young) or 12-month-old (aged) male WT mice for Fig. 3h.

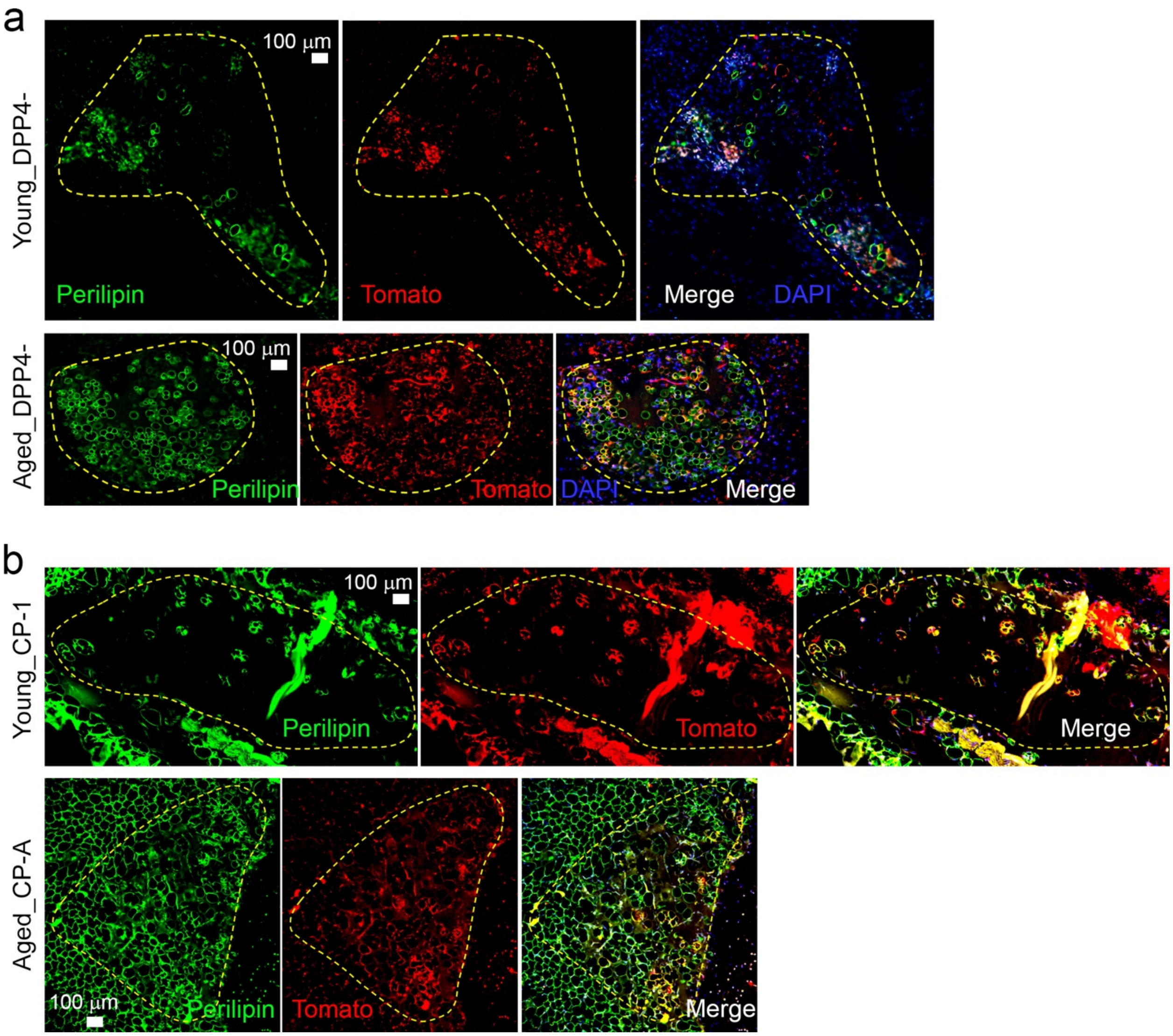

Sup Fig 3. 9 CP-A cells have high adipogenic potential *in vivo*

a, Immunofluorescence staining of Tomato and Perilipin in the transplanted Matrigel plugs of DPP4- APCs in Fig. 3j.

b, Immunofluorescence staining of Tomato and Perilipin in the transplanted Matrigel plugs of CP-1 and CP-A cells in Fig. 3l.

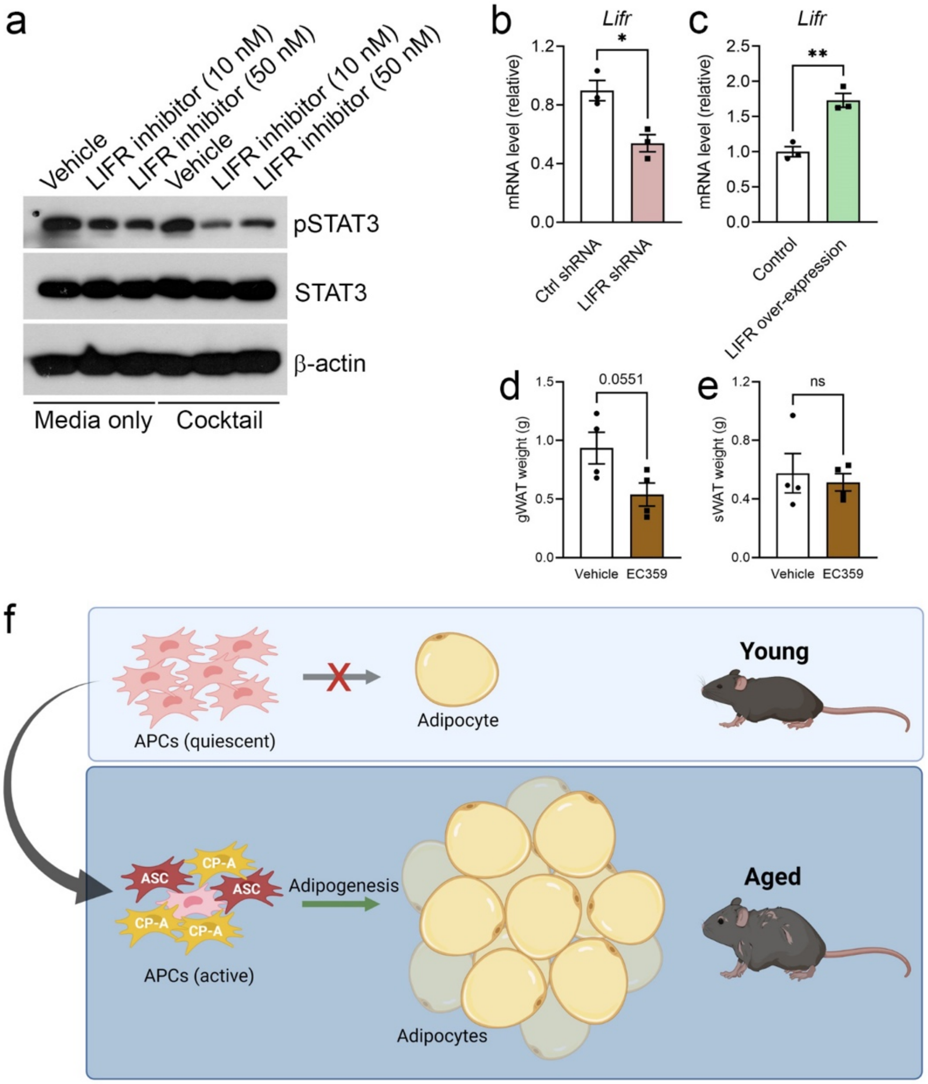

Sup Fig 3. 10 LIFR signaling controls CP-A adipogenesis
a, Western blot analysis of LIFR signaling after LIFR inhibitor, EC359 treatment.

b, Real-Time PCR analysis of *Lifr* mRNA level after LIFR knock down in Fig. 4e, g.

c, Real-Time PCR analysis of *Lifr* mRNA level after LIFR overexpression in Fig. 4i, k.

d, e, 9-month-old WT male mice were treated with LIFR inhibitor EC359 or vehicle for 10 weeks. Tissue weight of gWAT (d) and sWAT (e) after treatment. n=4 per group. Two-tailed Student’s t-test. All data represent the mean ± s.e.m.

f, Summarization of key findings: APCs in young adult mice are quiescent. These cells do not undergo adipogenesis unless triggered by metabolic challenges (such as high fat diet feeding or cold exposure). The aging process remodels APCs and generates ASCs that are highly proliferative, and CP-As that are both highly proliferative and adipogenic. LIFR, as a functional marker, regulates CP-A adipogenesis. The proliferation and differentiation of APCs in aged mice are spontaneous, without any external metabolic challenges. Illustration created with BioRender.com

Chapter 4. PPARg- Dependent Remodeling of Translational Machinery in Adipose

4.1 Introduction

Obesity is a complex and multifactorial chronic medical condition that results from an imbalance between energy intake and energy expenditure. This leads to an excessive accumulation of body fat, which has significant negative effects on an individual's physical, psychological, and social health and well-being, as well as an increased risk of developing several chronic diseases, such as cardiovascular disease, type 2 diabetes, and certain cancers, among others [128,129].

The adipose tissue plays a crucial role in the pathology of obesity. Its plasticity and functional heterogeneity allow it to respond to different stimuli, thereby facilitating the regulation of systemic energy balance. Adipose tissues, primarily the epididymal white adipose tissue (eWAT) and inguinal white adipose tissue (iWAT), differ in their metabolic profiles and response to external stimuli. eWAT is more associated with visceral fat accumulation and is linked to metabolic dysfunction, while iWAT tends to be subcutaneous and may offer some protective effects against metabolic disease.

However, during obesity, a maladaptation of adipose tissue ensues, impairing its function and contributing to systemic insulin resistance and inflammation[130]. The adipose progenitor cells (APCs) contribute significantly to this maladaptation, although their role is not yet fully understood. Single-cell RNA sequencing studies have begun to reveal the impressive heterogeneity and plasticity of these cells, yet questions remain about their contribution to metabolic homeostasis and potential targeting for therapy[131-143].

Peroxisome proliferator-activated receptor gamma (PPARγ), a nuclear receptor, plays a pivotal role in adipocyte differentiation and function, and is a key target of thiazolidinediones (TZDs), such as rosiglitazone. These drugs enhance insulin sensitivity, modulate inflammatory responses, and can even induce modest reductions in weight and adiposity in some individuals with obesity and insulin resistance [144-148]. Interestingly, whole-body insulin-sensitizing effects of rosiglitazone do not necessarily require PPARγ in adipocytes, suggesting that PPARγ-independent targets in adipose tissue or PPARγ's roles in other tissues and cell types, such as APCs, could be essential for the action of TZDs.

In this study we explore the substantial remodeling effects of acute rosiglitazone treatment on the white adipose depots of obese subjects. By employing Single-Cell RNA Sequencing, we uncover significant shifts in the stromal vascular cell composition after PPARγ agonist treatment. We observe a major shift in macrophage subpopulations, highlighting the immunomodulatory effects of rosiglitazone. A detailed profiling of adipose precursor cells in epididymal white adipose tissue (eWAT) reveals rosiglitazone drives a reduction in progenitor cells, induces adipogenesis, and remodels gene expression patterns in both progenitor cells and pre-adipocytes. The effects extend to the inguinal adipose tissue (iWAT), where rosiglitazone not only replicates its effects observed in eWAT, but also promotes enhanced adipocyte differentiation. Pathway analysis of differentially expressed genes reveals cell type-specific effects of rosiglitazone treatment and highlights its role in attenuating inflammatory responses, promoting ATP synthesis, and inducing ribosome biogenesis. Further analysis suggests a potential mechanism by which PPARγ drives enhancement in translation efficiency.

4.2 Results

Acute rosiglitazone treatment confers improvement in glucose tolerance and remodeling in the adipose tissue

To evaluate the impact of an acute PPARg agonist treatment on host physiology we treated wild-type (WT) C57BL/6 lean mice and obese Lepob/ Lepob (ob/ob) mice with either Rosiglitazone (Rosi) or Vehicle (Veh) by oral gavage for three days (**Figure 4.1A**). Despite no changes in body weight (**Figure 4.1B**), ob/ob mice treated with rosiglitazone (ob/ob-Rosi) presented an outstanding improvement in glucose tolerance, comparable to lean mice (**Figure 4.1C**). As expected, since we did not observe changes in total body weight, only a slight increase in brown adipose tissue (BAT) mass was observed after rosiglitazone treatment in both lean and obese mice (**Figure 4.1D**). No significant mass differences were observed in the inguinal white adipose tissue (iWAT), and epididymal white adipose tissue (eWAT) (**Figure 4.1E-F).** We next examined histological sections from adipose tissue and liver. Remarkably, ob/ob-Rosi mice had a decrease in the crown-like structures in the eWAT with no major alterations in the iWAT and BAT in both obese and lean conditions (**Figure 4.1G**). In addition to the remodeling in the adipose tissue microenvironment, the liver of WT-Veh mice presented no major histological changes but a minor increase in total mass (**Supplementary Figure 4.1A-B**). In contrast, the liver of ob/ob-Rosi mice exhibited a decrease in lipid accumulation (**Supplementary Figure 4.1A**) characterized by a reduction in the surface area covered by lipid droplets (**Supplementary Figure 4.1C**). Next, to assess the tissues responsible for the improvement in glucose homeostasis, we adapted the conventional glucose tolerance test by mixing the glucose bolus with 18F-FDG. After one hour of conscious glucose uptake, mice were subjected to PET/CT scans (**Supplementary Figure 4.1D**). ob/ob-Rosi mice exhibited an increase in glucose uptake in the brain, heart, liver, muscle, and adipose tissue (axillary) compared to ob/ob-Veh mice (**Supplementary Figure 4.1E-F**). To better visualize the glucose uptake in the fat depots and exclude the higher signals (e.g., heart, bladder), we reprocessed and cleared the scans using Dragonfly. Strikingly, ob/ob-Rosi mice had much greater glucose uptake in the adipose tissues compared to ob/ob-Veh mice (**Figure 4.1H**). Overall, acute rosiglitazone treatment resulted in a major remodeling of the obese host physiology, especially in the adipose depots.

scRNAseq uncovers stromal vascular cell remodeling after PPARg agonist treatment

Next, to investigate how rosiglitazone treatment could be affecting the stromal vascular fraction in the adipose tissue, we performed single-cell RNA Sequencing in both eWAT and iWAT. Since the most dramatic responses were observed in obese mice, we focused our efforts on ob/ob mice, treating them with either vehicle or rosiglitazone for 3 days. Additionally, we included a WT-Veh group to compare the baseline of a lean mice (**Figure 4.2A**). Briefly, datasets from both eWAT and iWAT were separately processed through the 10X Genomics Cell Ranger version 3.0.2 single-cell software to perform sample demultiplexing sequencing alignment to mouse genome mm10, filtering, and unique molecular identifier (UMI) counting to generate gene count matrices. Single cells were identified from background noise with the default setting of cell ranger. The filtered matrix was further selected with the proportion of mitochondrial reads (threshold: < 25%), the number of UMI (thresholds: 700-22,000), and the number of detected genes (thresholds: 200-6,000) (**Supplementary Figure 4.2A-B**). The split view t-SNE graphs visualizing expression patterns of the individual mice showed high reproducibility within groups (**Supplementary Figure 4.2C-D**).We were able to identify 10 major cell types described to be present in the adipose tissue: Smooth Muscle Cells (SMC), Neutrophils (Neu), B Lymphocytes (BC), Endothelial cells (EC), Adipocyte Progenitor Cells (APC), Natural Killer T cells (NKT), Dendric Cells (DC), Perivascular Macrophages (PVM), Lipid-Associated Macrophages (LAM), Non-Perivascular-like Macrophages (NPVM), and Proliferating-LAM (P-LAM) (**Figure 4.2B-E**). Interestingly, tissue-specific differences between eWAT and iWAT were evident, such as the exclusively presence of SMC and PLAM, in the eWAT and DC in the iWAT (**Figure 4.2B-C**). Remarkably, ob/ob-Rosi samples from both eWAT and iWAT presented a significant shift in the population's clusters resembling the expression pattern in the lean WT-Veh mice, presenting a major transcriptome remodeling induced by acute rosiglitazone treatment (**Figure 4.2 B-E**).

Rosiglitazone treatment leads to major shifts in macrophage subpopulations

Despite the presence of crown-like structures in the histology of the ob/ob-Veh (**Figure 4.G**), we did not observe the presence of a large population of Lipid-Associated Macrophages (LAM) by scRNA-seq in the ob/ob-Veh samples in either iWAT or eWAT (**Figure 4.2B-C**). Therefore, we hypothesized that due to the high lipid content of those cells, they may have floated associated with the mature adipocyte layer during enzymatic digestion. To test that, we collected the lipid layer after the enzymatic digestion, incubated overnight, and then performed confocal imaging (**Supplementary Figure 4.3 A**). We indeed observed a high concentration of F4/80 positive cells in both eWAT and iWAT of ob/ob-Veh mice. In addition to that, those cells presented a positive signal for Perilipin 1, suggesting a potential role phagocytosing apoptotic adipocytes. When compared to ob/ob-Rosi samples though, we observed a decrease in the number of the macrophages as well as a remodeling in the morphology, likely reflecting a different state of activation. The effect of rosiglitazone on macrophages has been previously described [149,150] and PPARg activation directs an alternative-activation profile by the IL4-PPARg-STAT6 pathway. To confirm this remodeling, we performed flow cytometry to better characterize the changes in the macrophage subpopulations after rosiglitazone treatment (**Supplementary Figure 4.3B**). Indeed, rosiglitazone treatment decreased the number of inflammatory and lipid-associated macrophages in both eWAT and iWAT, with a robust response in the eWAT (**Supplementary Figure 4.3C-F**).

Profiling of adipose precursor cells in Response to PPARg agonist treatment in the eWAT

Rosiglitazone has been described to induce adipogenesis *in vivo*. During a close examination of the histological sections in eWAT, we observed the presence of multi-locular cells marked with arrowheads that could be indicative of adipogenesis (**Figure 4.3A)**. As adipose tissue has reduced adipogenesis in the maladaptation process during obesity, the results show that rosiglitazone treatment did remodel the cell populations in a way that restores adipogenesis similar to the lean mice.

For a more detailed investigation of APCs in the scRNA-seq dataset, and to assess the transcriptomic shifts induced by rosiglitazone in APC subtypes, we centered our attention on the APC cluster expressing common adipocyte precursor markers such as Pdgfra. This APC cluster was further classified into progenitors and preadipocytes, considering the Louvain clustering of the top 25 principal components and subtype-specific gene expression (Pi16 and Dpp4 for progenitors and Icam1 and Cd36 for preadipocytes[154]) (**Figure 4.3 B-C**). In comparing the transcriptomic landscapes of WT-Veh, ob/ob veh, and ob/ob-Rosi, it was apparent that rosiglitazone treatment reshaped the gene expression profiles in obese mice to resemble that of lean mice. Rosiglitazone also influenced cell proportions in obese mice, with a notable decrease in progenitors and an increase in preadipocytes.

To corroborate these findings, flow cytometry was employed (**Figure 4.3 D**). Considering the high expression of Pdgfra in both progenitors and preadipocytes (FigS4A and FigS5A), we gated in PDGFRa+ cells post lineage exclusion (CD31-, CD45-), and subsequently isolated progenitors (DPP4+) and pre-adipocytes (ICAM1+ and ICAM1+/CD36+) (**Figure 4.3 E**). A significant reduction in both PDGFRA+ cells and DPP4+ cells post rosiglitazone treatment was observed, in alignment with the scRNA-seq data, whereas ICAM1+ and ICAM1+/CD36+ cell numbers remained unaffected. This suggests that transcriptomic alterations may not always manifest in surface marker expression. Utilizing confocal microscopy to visualize LipidTox-marked lipid droplets and quantifying lipid droplet cell area with ImageJ (**Figure 4.3 F-G**), a significant increase in lipid droplet count in both DPP4+ and DPP4- cells was observed, suggesting that rosiglitazone could stimulate adipogenesis in progenitor cells. Overall, rosiglitazone drives a reduction in progenitor cells, induces adipogenesis and remodels expression patterns in both progenitor cells and pre-adipocytes in eWAT.

Rosiglitazone drives enhancement of adipocyte differentiation in inguinal adipose tissue.

The effects of rosiglitazone were also analyzed in the context of iWAT. Upon inspection of histological sections of iWAT, the occurrence of multi-locular cells, indicative of adipogenesis, was also noted (**Figure 4.4A**), suggesting that rosiglitazone potentially induces adipogenesis in iWAT. In the scRNA-seq dataset, APCs are also classified into progenitors and preadipocytes with the same method and markers (**Figure 4.4 B-C**). In comparing the gene expression patterns of WT-Veh, ob/ob veh, and ob/ob-Rosi conditions, rosiglitazone treatment was also found to remodel the transcriptomic landscape in obese mice to more closely resemble lean mice.

Flow cytometry analysis in iWAT demonstrated a significant reduction in PDGFRA+ cells and ICAM1+ cells, while a significant increase in ICAM1+/CD36+ cells was observed following rosiglitazone treatment (**Figure 4.4 D-E**). This suggests that rosiglitazone could enhance the expression of maturation markers in preadipocytes. Observation of LipidTox-marked lipid droplets and assessment of lipid droplet cell area unveiled the existence of smaller-sized lipid droplets (**Figure 4.4F**). However, there was no significant alteration in the overall count of lipid droplets. In summary, within the iWAT environment, rosiglitazone appears to not only reproduce its adipogenesis-inducing and gene expression-modulating effects observed in eWAT, but also to promote the enhancement of adipocyte differentiation.

Comparison of differentially expressed and enriched pathways in response to obesity and rosiglitazone treatment

To discern the genes with distinct expression due to obesity and rosiglitazone treatment, Differentially Expressed Genes (DEGs) were identified using the Wilcoxon Rank Sum test with an Benjamini-Hochberg corrected p value < 0.05. These DEGs were then segmented into four categories: genes with increased expression in obese mice compared to lean mice (ob/ob_UP), genes with decreased expression in obese mice compared to lean mice (ob/ob_DOWN), genes with increased expression in response to Rosiglitazone treatment (Rosi_UP), and genes with decreased expression in response to Rosiglitazone treatment (Rosi_DOWN).

To further investigate the distinct and overlapping aspects of these DEG categories, we explored the intersections of DEGs across all four categories within both APC subtypes and across all cell types (**Figure. 4.5, Supplementary Figure.4.4**). The effects of rosiglitazone treatment, in modifying the transcriptomic profile of obese mice to better mirror lean mice, were evident in the DEGs shared between ob/ob_UP and Rosi_DOWN, and the DEGs shared between ob/ob_UP and Rosi_DOWN. These intersecting DEG sets predominated across all cell types.

In eWAT progenitors and eWAT preadipocytes, the most significant intersecting DEGs were those that exhibited an increase in obese mice and a corresponding decrease following rosiglitazone treatment (**Figure.4.5 A-B**). Conversely, in iWAT progenitors and iWAT preadipocytes, the largest intersecting DEGs were those that showed a decrease in obese mice and a corresponding increase following rosiglitazone treatment (**Figure.4.5 C-D**), highlighting the tissue-specific nature of rosiglitazone's corrective effect.

To comprehend the impact of rosiglitazone's corrective effect on different biological pathways, we undertook a pathway enrichment analysis in the reversed set of DEGs. We used Fisher's exact test to determine the overlap between the identified DEGs and the biological pathways listed in KEGG, REACTOME, BIOCARTA, and HALLMARK databases. The Benjamini-Hochberg method was employed to estimate the False Discovery Rate (FDR) and correct for multiple testing. We defined the enrichment score as the proportion of overlapping genes to total genes within our cell type-specific gene set, scaled by 20,000, and then divided by the total genes within the pathway.

Within the pathways enriched from the reversed set of genes in eWAT progenitors, the most enriched pathways showing an increase under rosiglitazone treatment were angiogenesis, epithelial mesenchymal transition, lysosome, PPAR signaling, and extracellular matrix organization. The pathways demonstrating a decrease under rosiglitazone treatment in eWAT progenitors were Atf6a chaperone activation, TNFA signaling, Ace2 pathway, IL-6 pathway, and Nfkb pathway, signifying that rosiglitazone mitigates the inflammatory response in eWAT progenitors (**Figure 4.5A**).

In eWAT preadipocytes, the top downregulated pathways under rosiglitazone also pertained to the inflammatory response, while the top upregulated pathways under rosiglitazone treatment were ribosome, angiogenesis, peptide chain elongation, translation, and lipid transport, suggesting that rosiglitazone prompts ribosome biogenesis in preadipocytes (**Figure 4.5B**). These variations in pathway enrichment results highlight the cell type-specific influence of rosiglitazone treatment in eWAT APCs.

In iWAT, both progenitors and preadipocytes have ribosome, formation of the 43S complex, peptide chain elongation, 3'UTR mediated translational regulation, and ATP synthesis related pathways in the top upregulated pathways and diverse inflammation-related pathways in the top downregulated pathways. These findings imply that rosiglitazone attenuates the inflammatory response and promotes ATP synthesis and ribosome biogenesis in both iWAT progenitors and preadipocytes.

PPARg-driven enhancement in translation efficiency

As ribosome pathways are among the top upregulated pathways by rosiglitazone treatment in APCs, we decided to examine the expression of ribosomal genes in more depth in relation to obesity and rosiglitazone treatment. We found that 85 ribosomal genes showed altered expression in APCs across both tissues (**Figure 4.6**).

In eWAT progenitors, these ribosomal DEGs demonstrated significant changes in their expression level, being largely downregulated due to obesity but upregulated in response to rosiglitazone treatment. In contrast, iWAT progenitors had only a few ribosomal genes showing differential expression due to obesity and rosiglitazone treatment.

For preadipocytes in both eWAT and iWAT, a number of ribosomal DEGs were found to be downregulated in response to obesity and upregulated following rosiglitazone treatment, with the effect being more pronounced in iWAT preadipocytes. This pattern of results suggests that rosiglitazone treatment stimulates ribosome biogenesis in a cell type specifc manner.

Considering that rosiglitazone is an activator of PPARγ, we pondered whether PPARγ might be binding to the promoter regions of ribosomal genes. According to a previously published study involving genome-wide profiling of PPARγ in eWAT, iWAT, and brown adipose tissue (BAT) using ChIP-Seq[155], PPARγ binding sites were identified in 41 ribosomal genes in eWAT and 24 ribosomal genes in iWAT (**Figure 4.7**). There is a substantial overlap between genes identified as having PPARγ binding sites in the ChIP-Seq study and the DEGs identified in our scRNA-seq analysis (**Supplementary Figure.4.5**). These findings suggest that PPARγ may contribute to enhancing translation efficiency.

4.3 Discussion

The pivotal role of peroxisome proliferator-activated receptor gamma (PPARγ) in adipogenesis and lipid metabolism has been long established, acting as a key molecular switch that regulates adipocyte differentiation, lipid storage, and glucose metabolism[156]. Thiazolidinediones, such as rosiglitazone, as PPARγ agonists, have been employed as insulin sensitizers for type 2 diabetes management. They exert their effect by enhancing insulin sensitivity in adipose tissue and promoting the differentiation of preadipocytes into insulin-sensitive adipocytes[157]. Adipose tissue plasticity, which refers to its capacity to undergo expansion, contraction, and remodeling, is crucial in maintaining metabolic homeostasis. In the context of obesity, adipose tissue remodeling becomes dysfunctional, often resulting in a state of chronic inflammation and metabolic dysregulation. Therefore, the impact of PPARγ agonists on adipose tissue plasticity in obesity warrants further exploration.

The present study offers a perspective on how acute rosiglitazone treatment influences white adipose tissue remodeling and cellular reprogramming in obesity. Rosiglitazone's effect on adipogenesis and the reduction of progenitor cells paints a complex picture of adipose tissue remodeling, with potential implications for adipose tissue function and metabolic regulation in obese states. Our findings demonstrate that rosiglitazone induces substantial transcriptomic alterations in both eWAT and iWAT progenitor cells and preadipocytes. This shift in the transcriptional landscape under the influence of rosiglitazone offers an intriguing insight into how PPARγ agonists may reprogram adipose tissue at the molecular level, promoting a more metabolically beneficial profile.

Rosiglitazone's potent immunomodulatory effects, as evidenced by the shift in macrophage subpopulations, underscore its potential to alleviate the chronic inflammation often associated with obesity. The shift from a pro-inflammatory to an anti-inflammatory macrophage profile could offer systemic metabolic benefits and contribute to improved insulin sensitivity.

Notably, our study also uncovered a potential link between rosiglitazone treatment and enhanced ribosome biogenesis. As the regulation of translation, encompassing ribosome biogenesis and initiation of translation, holds an essential role in cellular function and metabolic processes. Emerging research has suggested that an important protein in this context is the eukaryotic initiation factor 4E (eIF4E), a major cap binding protein, that has been implicated in the regulation of lipid homeostasis and obesity[158]. Notably, messenger RNAs (mRNAs) that are involved in lipid metabolic processing and storage pathways are enhanced at the translational level by eIF4E. It has been suggested that an inability to upregulate these mRNAs translationally results in an increase in fatty acid oxidation, which in turn enhances energy expenditure. Our scRNA-seq dataset also identify eIF4E as a differentially expressed gene, thus pointing towards its potential involvement in our study's context.

In this regard, several promising experimental approaches are worth considering to determine if and how PPARγ contributes to translation regulation. For example, polysome profiling provides a snapshot of the transcripts being translated at any given time, which can inform us about the effect of PPARγ activation on global protein synthesis. Phospho FACS of eIF4E, on the other hand, can elucidate the phosphorylation status of eIF4E, which is crucial in modulating its activity. Another intriguing method is Surface Sensing of Translation (SUnSET). This technique utilizes puromycin, an analogue of the aminoacyl tRNAs, which is incorporated into the nascent peptide chain, causing premature chain termination. By tracking puromycin-incorporated proteins, it allows for the quantification of the rate of protein synthesis, offering insights into translational regulation under varying conditions, including the influence of PPARγ. Through these prospective analyses and experiments, we can delve deeper into the intricate mechanisms underlying the role of PPARγ in translation regulation.

4.4 Conclusions

The present study provides a cell type-specific view of how acute rosiglitazone treatment influences white adipose tissue remodeling and cellular reprogramming in the context of obesity. Rosiglitazone was found to induce adipogenesis, reduce progenitor cells, and significantly alter the transcriptomic landscape of both eWAT and iWAT progenitor cells and preadipocytes. Moreover, rosiglitazone demonstrated the capacity to alleviate inflammatory responses and enhance ATP synthesis and ribosome biogenesis in iWAT cells. The observed shift in macrophage subpopulations further illustrates the potent immunomodulatory effects of rosiglitazone. The pathway analysis suggest a novel potential role for PPARγ in enhancing translation efficiency, underscoring the need for further investigations into its mechanism. This study thus opens new avenues for understanding the cellular and molecular mechanisms underpinning adipose tissue remodeling and the therapeutic effects of PPARγ agonists in the context of obesity.

4.5 Methods

Mice

Adult C57BL/6J (12-week-old) male mice (stock #000664) and Lepob/Lepob (stock #000632) were acquired through Jackson Laboratories. All mice were housed at a maximum of 5 animals per cage in temperature-controlled rooms under a 12-hour light/dark cycle and provided water and chow *ad libitum*. All mouse procedures were performed under animal study proposals approved by the University of California, Los Angeles Animal Research Committee (ARC 2019-066).

Rosiglitazone treatment

To examine the effects of PPARg agonist, C57BL/6J and Lepob/Lepob mice were given 30 mg/kg rosiglitazone (Sigma R2408), or vehicle [2.6% methylcellulose (StemCell Technologies, M3120) diluted 1:5 in Dulbecco's modified medium (GIBCO)] by oral gavage in the morning and evening for three consecutive days.[152]

Stromal vascular fraction isolation

Stromal vascular fractions were isolated as previously described [153]. Briefly, WAT depots were cut into small pieces, suspended in DMEM (GIBCO) + 50 mM HEPES

(GIBCO) + 1mg/mL type II collagenase (Sigma), + 1% BSA -low fatty acid (Gemini), and digested for 30 minutes at 37°C with agitation (120 rpm). The resulting dissociated tissue was passed through 100μm strainers, and adipocytes were removed from the supernatant by centrifugation. After a second filtration with 40μm strainers, red blood cells were lysed using ACK lysis buffer (GIBCO). The resulting pellets were processed further for 10X 3'GEX library preparation and sequencing or flow cytometry.

10X 3'GEX library preparation and sequencing

The Chromium Single Cell Gene Expression Solution upgrades short read sequencers to deliver a scalable microfluidic platform for 3' digital gene expression by profiling 500-10,000 individual cells per sample. A pool of ~3,500,000 10x Barcodes are sampled separately to index each cell's transcriptome. It is done by partitioning thousands of cells into nanoliter-scale Gel Beads-in-emulsion (GEMs), where all generated cDNA shares a common 10x Barcode. Libraries are generated and sequenced from the cDNA and 10x Barcodes are used to associate individual reads back to the individual partitions. In addition to the poly(dT) primer that enables the production of barcoded, full-length cDNA from poly-adenylated mRNA, the Single Cell 3' v3.1 Gel Beads also include two additional primer sequences (Capture Sequence 1 and Capture Sequence 2), that enable capture and priming of Feature Barcoding technology compatible targets or analytes of interest. Only the poly(dT) primers are used in this protocol for generating Single Cell 3' Gene Expression libraries. GEMs are generated by combining barcoded Single Cell 3' v3.1 Gel Beads, a Master Mix containing cells, and Partitioning Oil onto

Chromium Next GEM Chip G. To achieve single cell resolution, cells are delivered at a limiting dilution, such that the majority (~90-99%) of generated GEMs contain no cells, while the remainder largely contain a single cell. Immediately following GEM generation, the Gel Bead is dissolved, primers are released, and any co-partitioned cell is lysed. Primer containing (1) an Illumina TruSeq Read 1 (read 1 sequencing primer), (2) 10x Barcode, (3) 12nt unique molecular identifier (UMI), and (3) 30nt poly(dT) sequence are mixed with the cell lysate and a Master Mix containing reverse transcription (RT) reagents. Incubation of the GEMs produces barcoded, full-length cDNA from poly-adenylated mRNA. After incubation, GEMs are broken, and pooled fractions are recovered. Silane magnetic beads are used to purify the first-strand cDNA from the post GEM-RT reaction mixture, which includes leftover biochemical reagents and primers. Barcoded, full-length cDNA is amplified via PCR to generate sufficient mass for library construction. Enzymatic fragmentation and size selection are used to optimize the cDNA amplicon size. TruSeq Read 1 (read 1 primer sequence) is added to the molecules during GEM incubation. P5, P7, a sample index, and TruSeq Read 2 (read 2 primer sequence) are added via End Repair, A-tailing, Adaptor Ligation, and PCR. The final libraries contain the P5 and P7 primers used in Illumina bridge amplification. A Chromium Single Cell 3’ Gene Expression library comprises standard Illumina paired-end constructs which begin and end with P5 and P7. The 10x Barcode and 12 bp UMI are encoded in Read 1, while Read 2 is used to sequence the cDNA fragment. Sample index sequences are incorporated as the sample index read. TruSeq Read 1 and TruSeq Read 2 are standard Illumina sequencing primer sites used in paired-end sequencing. These libraries were sequenced using Illumina's NovaSeq6000 platform in paired end 2x100bp configuration. Data quality check was done on Illumina SAV, and data de-multiplexing was performed with Illumina Bcl2fastq v2.19.1.403 software.

scRNA-seq data processing and quality control

The 10X Genomics Cell Ranger version 3.0.2 single-cell software[26] was used to perform sample demultiplexing sequencing alignment to mouse genome mm10, filtering, and unique molecular identifier (UMI) counting to generate gene count matrices. Single cells were identified from background noise by filtering on the proportion of mitochondrial reads (threshold: < 25%), the number of UMI (thresholds: 700-22,000), and the number of detected genes (thresholds: 200-6,000).

Cell clustering and cell type identification

The cell clustering and cell type identification were performed using the Seurat R package version 4.0.2. The Louvain algorithm was employed to determine cell clusters based on similarities in transcriptome patterns, and the resulting clusters were visualized using t-Distributed Stochastic Neighbor Embedding (t-SNE) and Uniform Manifold Approximation and Projection (UMAP). Highly variable genes selected using the FindVariableFeatures function with default parameters were subjected to principal component analysis (PCA). The number of principal components used for Louvain clustering and subsequent visualization was determined with the Jackstraw permutation approach (n=25 for clustering of all cells and n=15 for APC sub-clustering). Cell type identities of the clusters were resolved by comparing the cell cluster-specific marker genes expressed in each cluster in our own dataset, identified with a Wilcoxon rank sum test, with known cell-type-specific markers curated from literature, single-cell atlases, and previous studies in the white adipose tissue. For a gene to be considered in the cell cluster marker analysis, it had to be expressed in at least 10% of the single cells from the cluster of interest and exhibit at least a 0.25 log-fold change in the cell cluster of interest compared to other cells. Multiple testing was corrected using the Benjamini-Hochberg method to estimate the false discovery rate (FDR).

Identification of differentially expressed genes (DEGs) and pathways

To determine which genes were affected by genetic background or rosiglitazone treatment, we compared the cell transcriptome of each cell type between age groups using a Wilcoxon rank sum test. To be considered in the analysis, a gene had to be expressed in at least 10% of the single cells from at least one of the two groups for that cell type and there had to be at least 1.1-fold change in gene expression between the groups. Multiple testing correction was done using the Benjamini–Hochberg method to estimate FDR. To assess pathway enrichment, we performed Fisher's exact test to determine the overlap between the DEGs and pathways from KEGG, REACTOME, BIOCARTA, and HALLMARK. Multiple testing correction was performed using the Benjamini-Hochberg method to estimate FDR. The enrichment score was calculated as the number of overlapped genes divided by the number of genes in our cell type-specific gene set, multiplied by 20,000 and then divided by the total number of genes in the pathway.

Flow Cytometry and Sorting

Cells were analyzed for cell-surface markers using fluorophore-conjugated antibodies (BioLegend, eBioscience). Cell surface staining was performed in HBSS (GIBCO). Flow cytometry was performed using the Attune NxT and data were analyzed with FlowJo software (BD). Cell surface and intracellular staining were performed using the following fluorophore-conjugated antibodies: (a) macrophages panel: CD45.2 (104), TCRβ (H57-597), CD3 (17A2), CD19 (6D5), NK1.1 (PK136), Ly6G (1A8), CD11c (N418), CD11b (M1/70), CD88 (20/70), CD9 (MZ3), Tim-4 (RMT4-54). (b) progenitors: Lineage negative: CD45.2 [104], and CD31 [390], PDGFRα (APA5), DPP4 (H194-112), ICAM-1 (YN1/1.7.4), CD36 (HM36). For sorting, cell suspensions were stained with: CD45.2 [104], and CD31 [390], PDGFRα (APA5), DPP4 (H194-112), and DAPI (AAT Bioquest) and sorted on FACSAria III (BD).

Confocal

Sorted cells were plated in a 96-well plate and culture in DMEM (GIBCO), 5mg/mL insulin (GIBCO), 10% FBS (Omega FB#11), 1% PenStrep (GIBCO), and 50ng/mL Primocin (Invivogen) until confluency. Adipogenic cocktail (0.5mM 3-isobutyl-1-methylxanthine (Sigma), 1mM Dexamethasone (Sigma), 5mg/mL Insulin (GIBCO) was added for two days, and then replaced with minimal media (DMEM, 10% FBS, 5mg/mL insulin) until day 4 of differentiation. Cells were fixed with 4% paraformaldehyde, permeabilized with 0.1% Triton and stained with LipidTOX Green Neutral Lipid

(Invitrogen) and DAPI (AAT Bioquest). Images were acquired using Zeiss LSM900 microscope.

Histology and Lipid Droplet Quantification

Tissues were fixed for 48h in 10% buffered formalin (ThermoFisher), after which they were washed with 70% ethanol (Thermofisher), sectioned in paraffin (10 μm thickness for adipose tissues and 5 μm for liver), and stained with hematoxylin and eosin (H&E). The lipid droplet cell area was quantified using ImageJ.

Glucose tolerance test

For glucose tolerance tests, mice were fasted for 6 hours prior to the challenge with glucose (1 g/kg mouse) via intraperitoneal injection. Blood glucose levels were assessed by tail vein bleeding using a glucometer (Accu-Chek). AUC was determined using Prism software (GraphPad).

Serum metabolomics

For metabolite extraction 5 μL plasma was mixed with 500 μL methanol: water (80:20) solution (-80 °C). Samples were centrifuged for ten minutes at 17,000 g (4 °C) and 450 μL of each sample was evaporated using a Nitrogen evaporator (Organomation). Evaporated metabolite extracts were stored at -80 °C. Dried metabolites were reconstituted in 100 μL of a 50% acetonitrile (ACN) 50% dH20 solution. Samples were vortexed and spun down for 10 min at 17,000g. 70 µL of the supernatant was then transferred to HPLC glass vials. 10 µL of these metabolite solutions were injected per analysis. Samples were run on a Vanquish (Thermo Scientific) UHPLC system with mobile phase A (20mM ammonium carbonate, pH 9.7) and mobile phase B (100% ACN) at a flow rate of 150 µL/min on a SeQuant ZIC-pHILIC Polymeric column (2.1 × 150 mm 5 µm, EMD Millipore) at 35°C. Separation was achieved with a linear gradient from 20% A to 80% A in 20 min followed by a linear gradient from 80% A to 20% A from 20 min to 20.5 min. 20% A was then held from 20.5 min to 28 min. The UHPLC was coupled to a Q-Exactive (Thermo Scientific) mass analyzer running in polarity switching mode with spray-voltage=3.2kV, sheath-gas=40, aux-gas=15, sweep-gas=1, aux-gas-temp=350°C, and capillary-temp=275°C. For both polarities mass scan settings were kept at full-scan-range = (70-1000), ms1-resolution=70,000, max-injection-time=250ms, and AGC-target=1E6. MS2 data was also collected from the top three most abundant singly charged ions in each scan with normalized-collision-energy=35. Each of the resulting ". RAW" files were then centroided and converted into two ".mzXML" files (one for positive scans and one for negative scans) using msconvert from ProteoWizard. These ".mzXML" files were imported into the MZmine 2 software package. Ion chromatograms were generated from MS1 spectra via the built-in Automated Data Analysis Pipeline (ADAP) chromatogram module and peaks were detected via the ADAP wavelets algorithm. Peaks were aligned across all samples via the Random sample consensus aligner module, gap-filled, and assigned identities using an exact mass MS1(+/-15ppm) and retention time RT (+/-0.5min) search of our in-house MS1-RT database. Peak boundaries and identifications were then further refined by manual curation. Peaks were quantified by area under the curve integration and exported as CSV files. If stable isotope tracing was used in the experiment, the peak areas were additionally processed via the R package AccuCor 2 to correct for natural isotope abundance. Peak areas for each sample were normalized by the measured area of the internal standard trifluoromethanesulfonate (present in the extraction buffer) and by the number of cells present in the extracted well.

μPET/μCT

Lepob/Lepob mice (stock #000632) (12 weeks old, male) treated with either vehicle (n=6) or rosiglitazone (n=6) were fasted for six hours, prior to intravenous injections via tail vein with 85-90 μCi of [18F]-FDG that had been mixed with glucose based on the weight of the mouse (1g/Kg). Following a 50-minute conscious uptake of [18F]-FDG, mice were anesthetized with 2% vaporized isoflurane, and PET (energy window 350-650 keV, 10-min static scan) and CT (voltage 80 kVp, current 150 μA, 720 projections, 200μm resolution, scan time 1 min) images were acquired on a GNEXT PET/CT scanner (Sofie Biosciences, Dulles, VA). The PET images were reconstructed using a 3D-Ordered Subset Expectation Maximization (OSEM) algorithm (24 subsets and 3 iterations), with random, attenuation, and decay correction. The CT images were reconstructed using a Modified Feldkamp Algorithm. Amide software was used to analyze co-registered μPET/μCT images, and a full body panel was generated by placing ROIs for the brain, blood, liver, left and right kidney, bladder, muscle, left and right lung, gastrointestinal tract, and adipose tissues. Visual representation of μPET signal from adipose tissues was generated using ORS Dragonfly software (Object Research Systems Inc, Montreal, Canada).

4.6 Figures

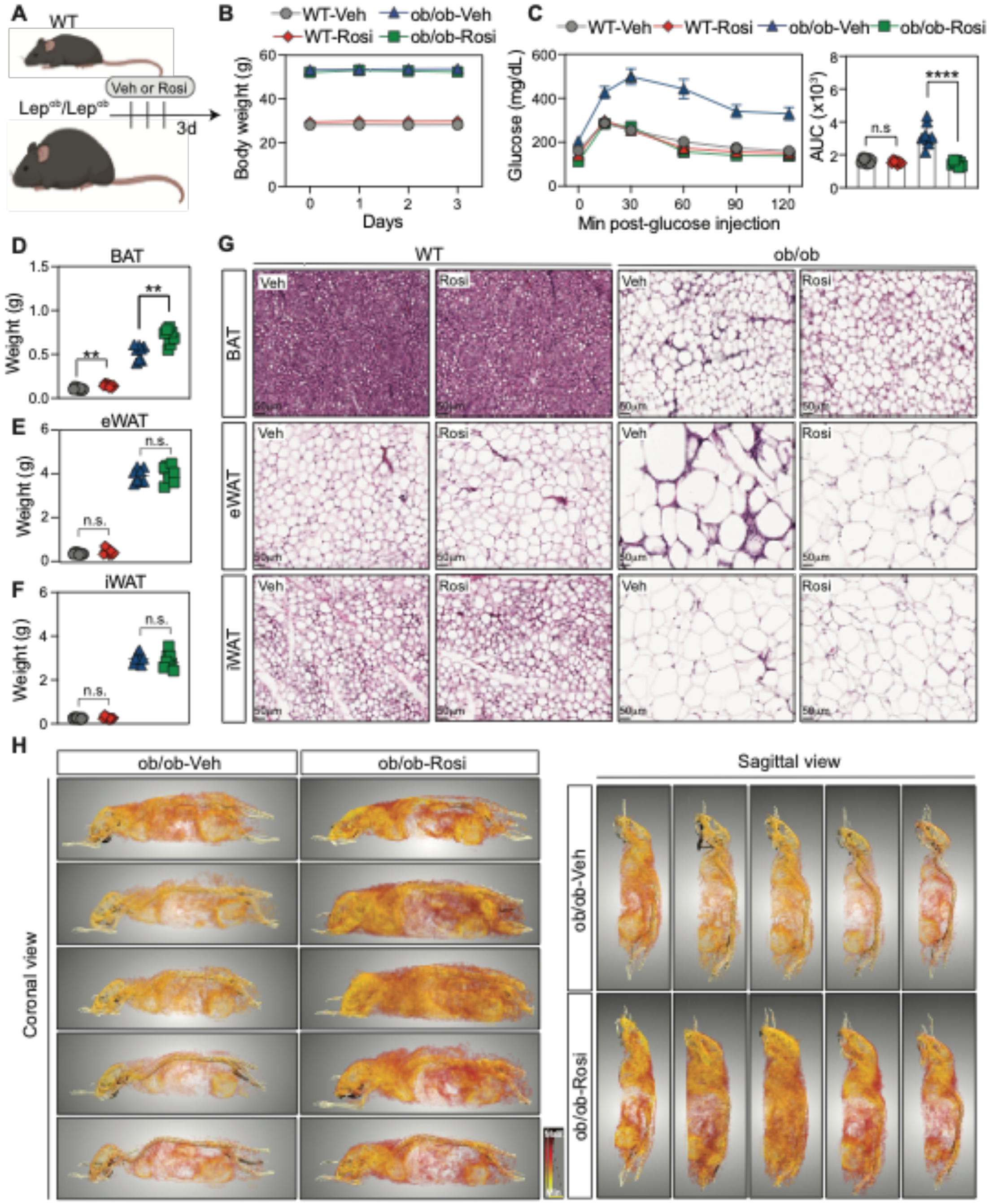

Fig 4. 1 Adipose tissue remodeling after acute rosiglitazone treatment
A, Schematic diagram of the experimental design: lean (WT) and obese (ob/ob) mice were orally gavaged with either vehicle or rosiglitazone (30mg/Kg) for 3 days.

B, Total body weight for the four groups**.**

C, Blood glucose curve during intraperitoneal glucose tolerance test and area under the curve of blood glucose for four groups.

D-F, Adipose tissue weight: brown adipose tissue (BAT), epidydimal adipose tissue (eWAT), inguinal adipose tissue (iWAT).

G, Histological analysis of BAT, eWAT, and iWAT (hematoxylin and eosin stain).

H, Dragonfly visualization of adipose tissue 18F-FDG (100mCi) glucose uptake after one-hour conscious uptake. Data represent mean ± SEM (n = 8 mice per group). *$P < 0.05$; **$P < 0.01$; ***$P < 0.001$ by two-tailed Student's t test, (C) two-way ANOVA followed by Bonferroni post hoc test.

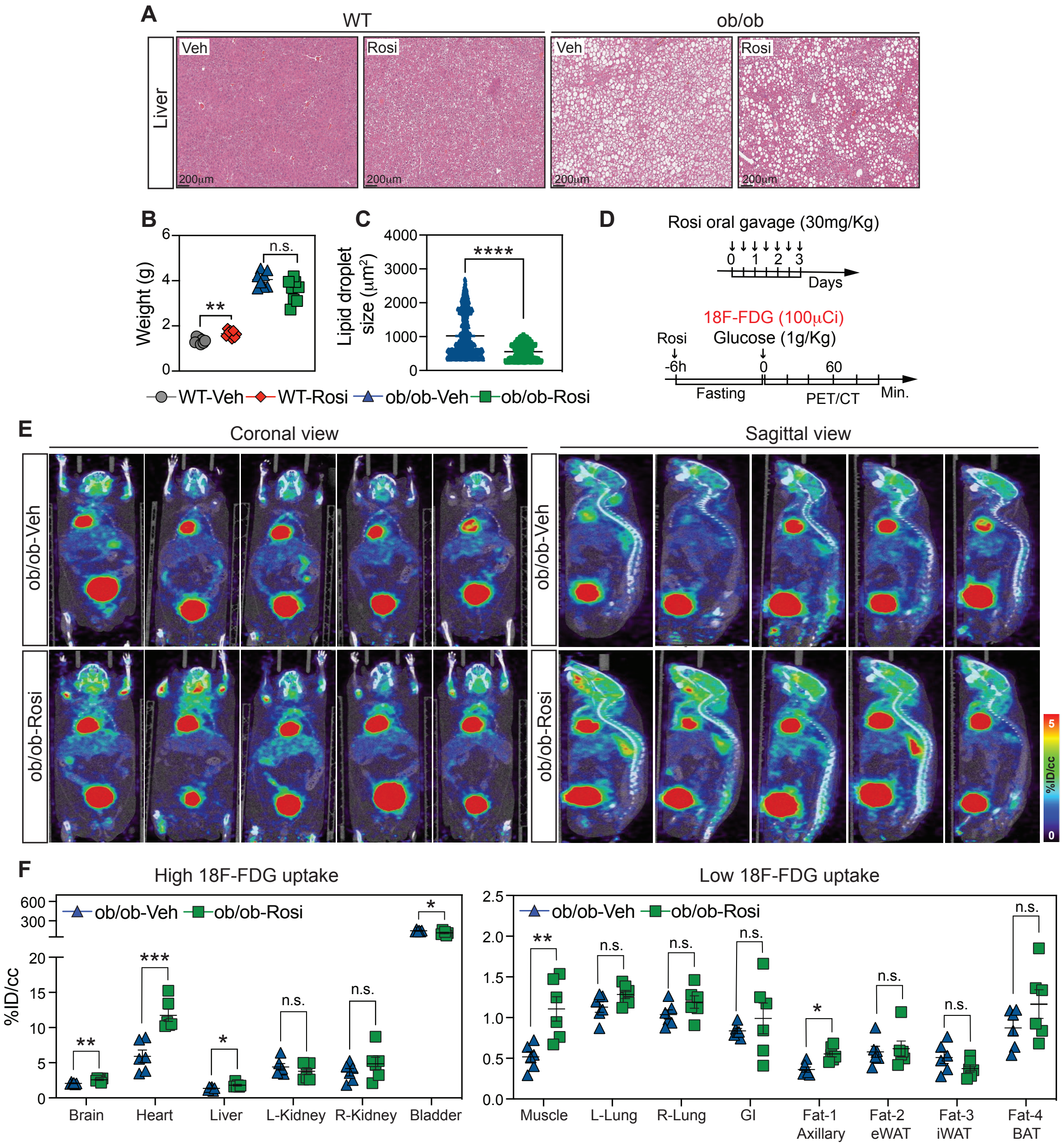

Sup Fig 4. 1 Host physiology remodeling after rosiglitazone treatment
A, Histological analysis of liver after acute rosiglitazone treatment (30mg/Kg).

B, Liver weight.

C, Lipid droplet area quantification of ob/ob mice treated either vehicle or rosiglitazone.

D, Schematic overview of conscious glucose uptake *in vivo* using a bolus of glucose (1g/Kg) and 18F-FDG (100mCi).

E, PET/CTs at coronal and sagittal view of ob/ob mice treated either vehicle or rosiglitazone.

F, Quantification of percent injected dose per cubic centimeter in tissue (%ID/cc). Data represent mean ± SEM (n = 6-8 mice per group). $^*P < 0.05$; $^{**}P < 0.01$; $^{***}P < 0.001$ by two-tailed Student's t test.

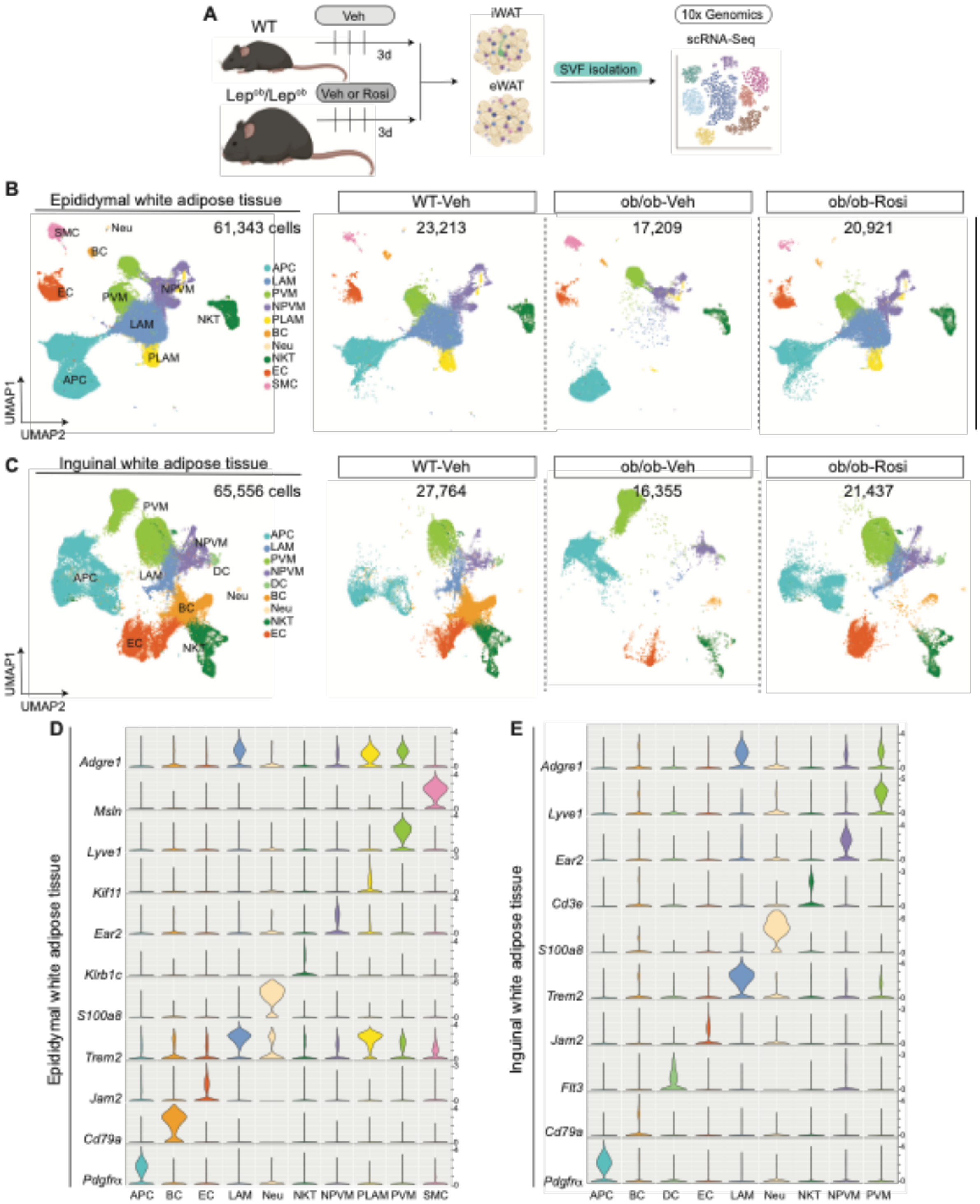

Fig 4. 2 Single-Cell RNA Sequencing Uncovers Stromal Vascular Cell Remodeling after PPARγ agonist treatment

A, Single-cell RNA Sequencing was conducted on the stromal vascular fraction extracted from both epididymal white adipose tissue (eWAT) and inguinal white adipose tissue (iWAT) in C56BL/6J and Lepob/Lepob mice that had received either a 30 mg/kg dose of rosiglitazone or a vehicle control for three consecutive days.

B, C, Uniform Manifold Approximation and Projection (UMAP) plot illustrates the cell clusters among 61,343 eWAT cells and 65,556 iWAT cells. The right three panels separately represent cells from WT-Veh, ob/ob-Veh, and ob/ob-Rosi. Each colored dot signifies a cell, with distinct colors indicating various cell types. The Louvain algorithm was utilized to determine cell clusters. This dataset was gleaned from a single experiment, with n=2 per group.

D, E, Cluster-specific expression of known cell markers: Adipocyte Progenitor Cells (APC) — Pdgfra, B Lymphocytes (BC) — Cd79a, Dendric Cells (DC) — Flt3, Endothelial cells (EC) — Jam2, Lipid-Associated Macrophages (LAM) — Trem2 and Adgre1, Neutrophils (Neu) — S100a8, Natural killer T cells (NKT) — Klrb1c and Cd3e, Non-Perivascular-like Macrophages (NPVM) — Ear2 and Adgre1, Proliferating-LAM (P-LAM) — Kif11, Trem2 and Adgre1, Perivascular Macrophages (PVM) — Lyve1 and Adgre1, Smooth Muscle Cells (SMC) — Msln. This analysis confirms that each cluster validates a particular cell type.

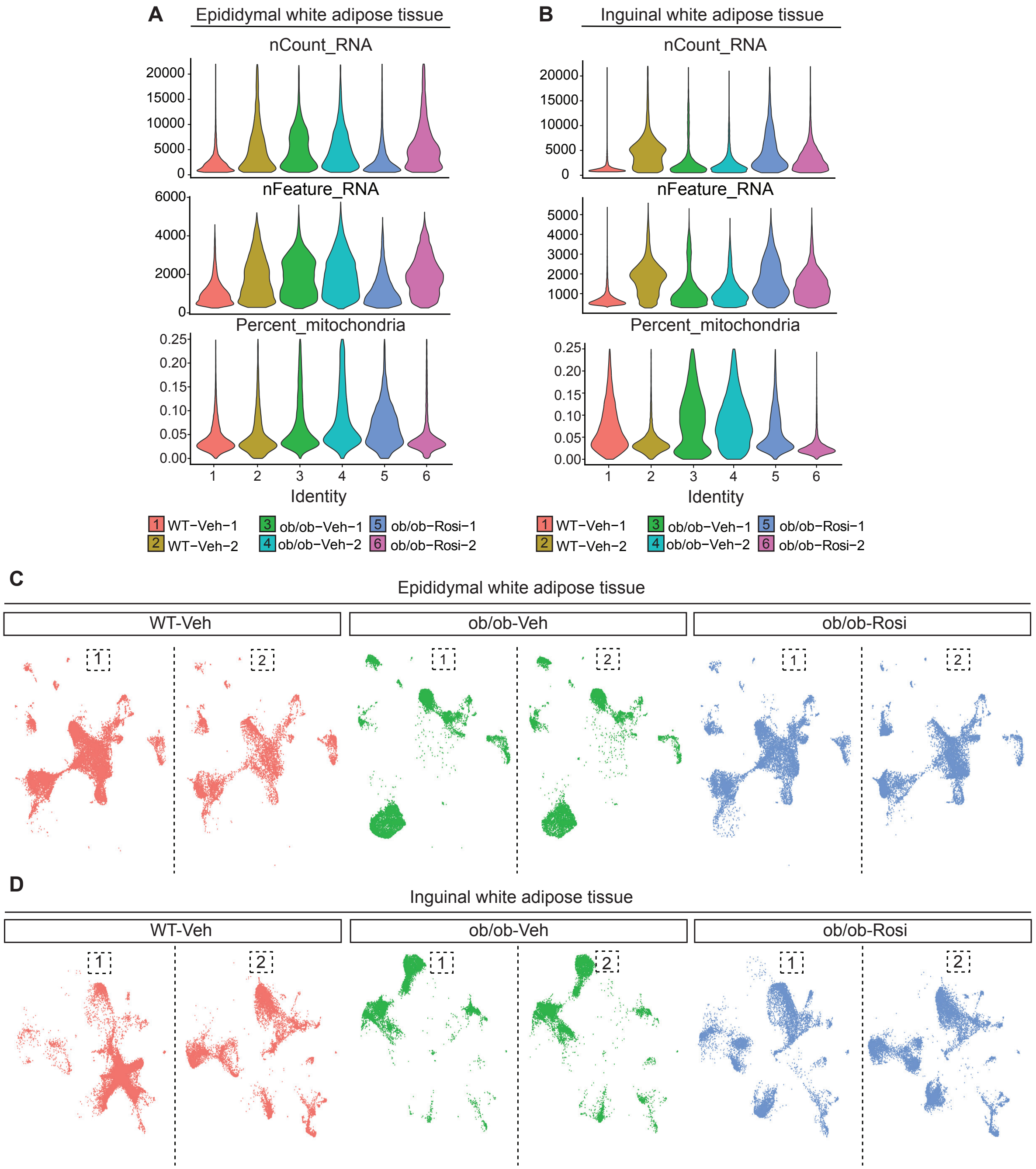

Sup Fig 4. 2 Adipose stromal vascular fraction Single-Cell RNA Sequencing quality control

A, B, Violin plots display the distribution of the number of Unique Molecular Identifiers (UMI) (nCount_RNA), the number of detected genes (nFeature_RNA), and the proportion of mitochondrial reads (Percent_mitochondria) across each sample in eWAT

(**A**) and iWAT (**B**). Cells were selected based on the number of UMIs (with a threshold range of 700-22,000), the number of detected genes (with a threshold range of 200-6,000), and the proportion of mitochondrial reads (with a threshold of less than 25%). **C, D,** UMAP plot illustrates the cell clusters among 61,343 eWAT cells (C) and 65,556 iWAT cells (D) by each sample. The three panels separately represent cells from WT-Veh, ob/ob-Veh, and ob/ob-Rosi groups. Each colored dot signifies a cell. Data shows a single scRNA-Seq experiment (n=2 per group).

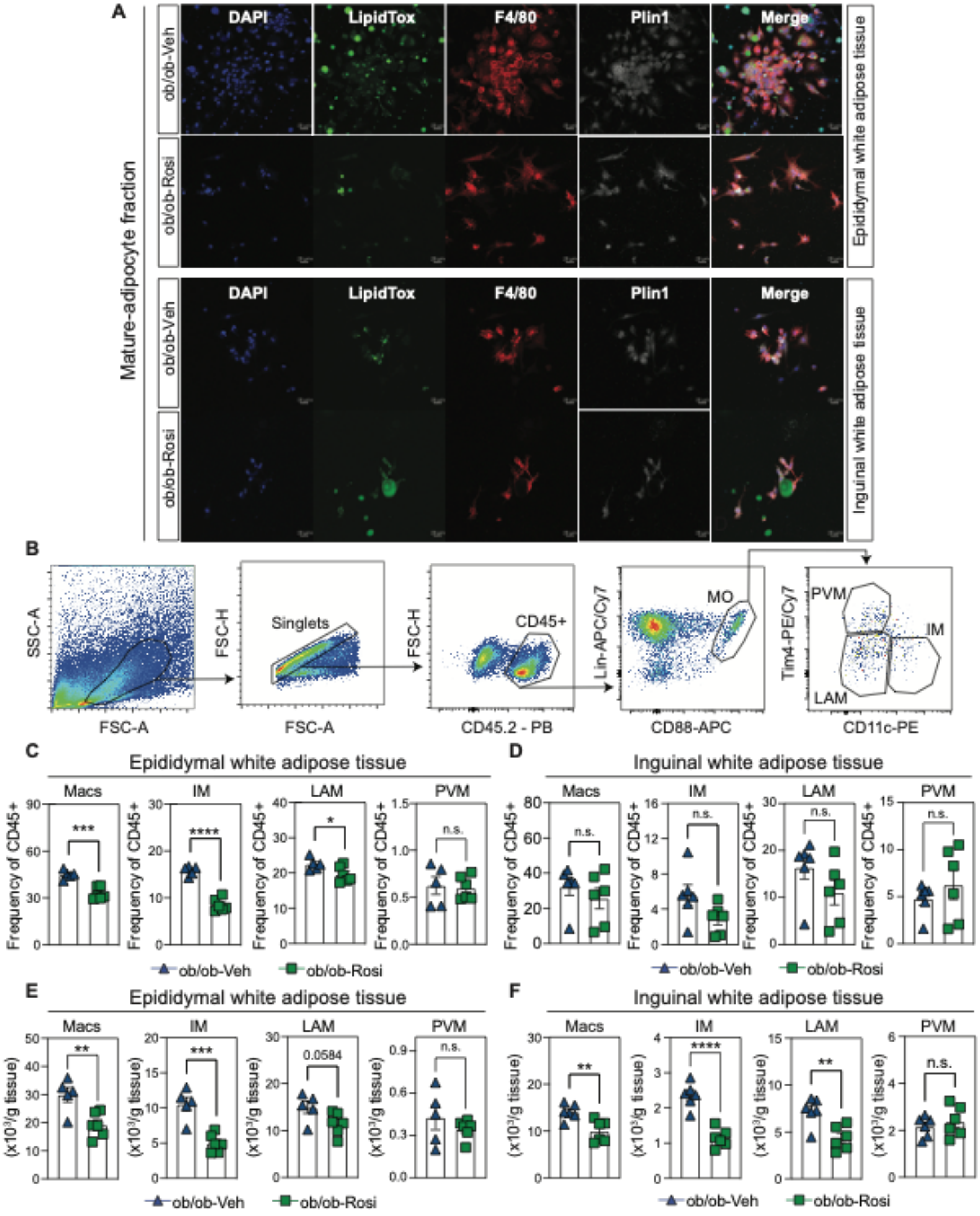

Sup Fig 4. 3 Adipose-specific macrophage profile remodeling after PPARg agonist treatment

A, Confocal images of macrophages (F4/80+) cultured overnight from the mature-adipocyte fraction of either ob/ob-Veh or ob/ob-Rosi: DAPI (nuclei), LipidTox (neutral lipids), F4/80 (macrophages), Plin1 (adipocyte-specific perilipin).

B, Flow cytometry gate strategy for macrophages: Tim4+: perivascular macrophages (PVM), Cd11c+: inflammatory macrophages (IM), Tim4-, Cd11c-: lipid-laden macrophages (LAM).

C-F, Frequency and absolute number of Macrophages (Mac), IM, LAM, and PVM from epididymal and inguinal adipose tissue. Data represent mean ± SEM (n = 6 mice per group). $^{*}P < 0.05$; $^{**}P < 0.01$; $^{***}P < 0.001$ by two-tailed Student’s t test.

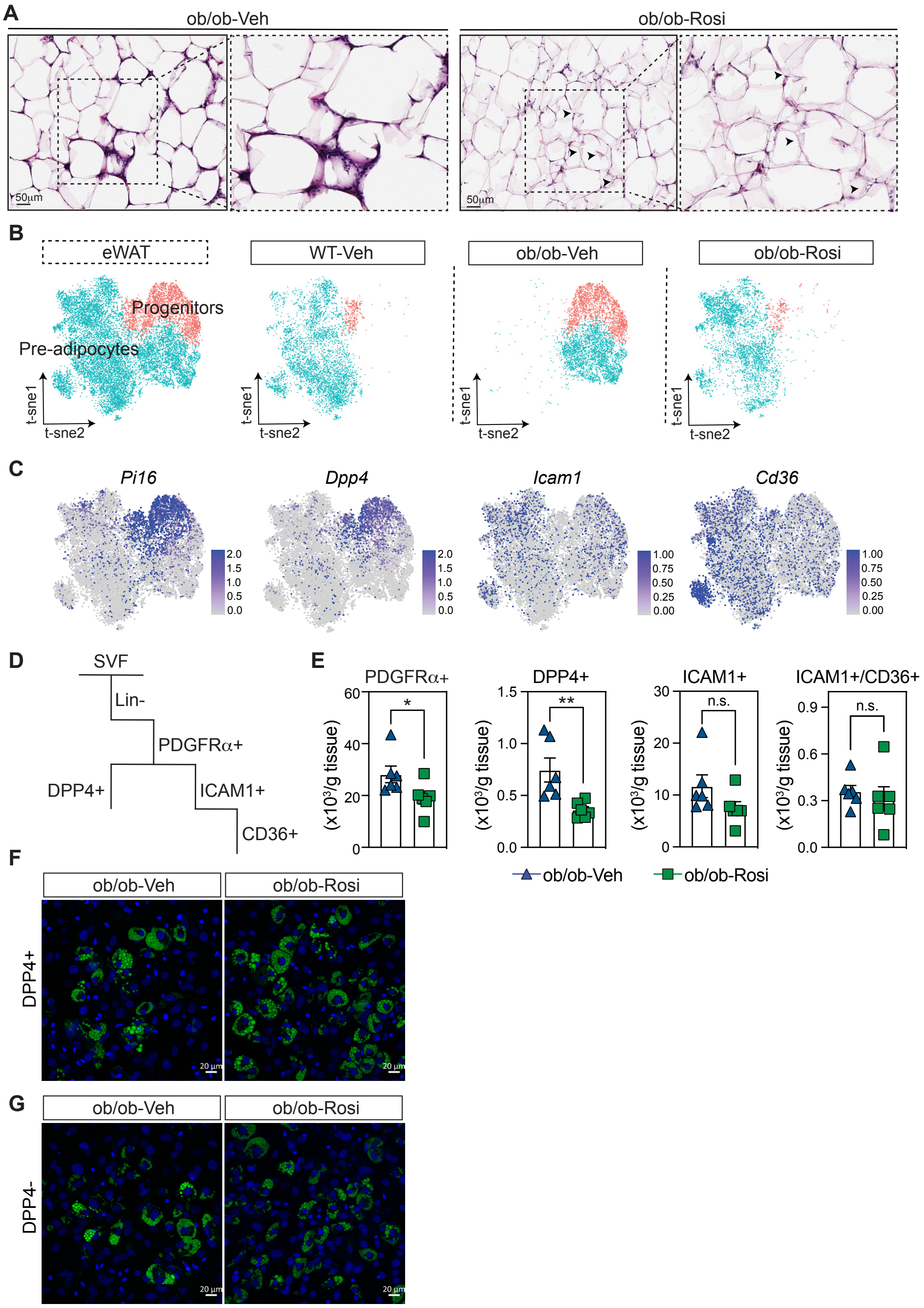

Fig 4. 3 Remodeling of epididymal adipocyte precursor cells in response to PPARg agonist

A, Histological analysis of epididymal adipose tissue (hematoxylin and eosin stain) from either ob/ob-Veh or ob/ob-Rosi mice.

B, t-distributed stochastic neighbor embedding (t-SNE) plot illustrates two subclusters of adipocyte precursor cells in the eWAT: progenitors and preadipocytes. The right three panels separately represent cells from WT-Veh, ob/ob-Veh, and ob/ob-Rosi. Each color-coded dot represents a cell, with progenitors being represented by red and preadipocytes by cyan. The Louvain algorithm was utilized to determine cell clusters.

C, Individual gene t-SNE plots showing the expression and distribution of representative marker genes: Pi16 and Dpp4 for progenitors, Icam1 and Cd36 for preadipocytes.

D, Gate strategy to characterize progenitor cells: Lineage negative (CD45-, CD31-), PDGFRa+, DPP4+ (progenitors), and ICAM1+/CD36+ (pre-adipocytes).

E, Absolute number of progenitor and pre-adipocytes from ob/ob-Veh and ob/ob-Rosi mice.

F-G, Confocal of sorted lineage negative (CD45-, CD31-), PDGFRa+, DPP4+ and DPP4- cells differentiated for 4 days on DMI (dexamethasone, IBMX, and insulin) media, DAPI (nuclei), LipidTox (neutral lipids). Data represent mean ± SEM (n = 6 mice per group). Confocal images: 4 wells per conditions, 2 representative images per well were acquired. $^*P < 0.05$; $^{**}P < 0.01$; $^{***}P < 0.001$ by two-tailed Student's t test.

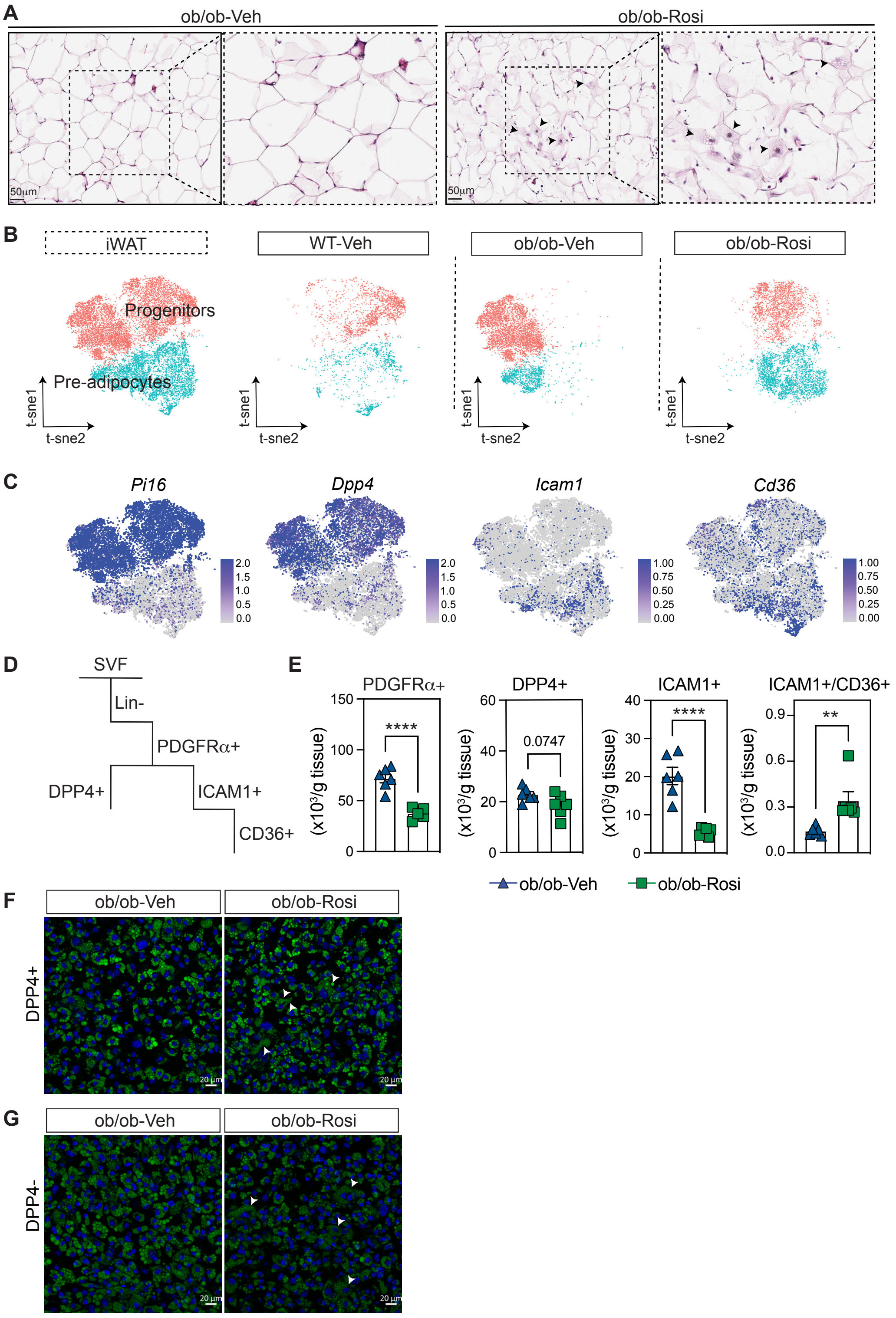

Fig 4. 4 Rosiglitazone-driven enhancement of adipocyte differentiation in inguinal adipose tissue

A, Histological analysis of inguinal adipose tissue (hematoxylin and eosin stain) from either ob/ob-Veh or ob/ob-Rosi mice.

B, t-distributed stochastic neighbor embedding (t-SNE) plot illustrates two subclusters of Adipocyte Precursor Cells in iWAT: Progenitors and Pre-adipocytes. The right three panels separately represent cells from WT-Veh, ob/ob-Veh, and ob/ob-Rosi. Each color-coded dot represents a cell, with Progenitors being represented by red and Pre-adipocytes by cyan. The Louvain algorithm was utilized to determine cell clusters.

C, Individual gene t-SNE plots showing the expression and distribution of representative marker genes: Pi16 and Dpp4 for progenitors, Icam1 and Cd36 for preadipocytes.

D, Gate strategy to characterize progenitor cells: Lineage negative (CD45-, CD31-), PDGFRa+, DPP4+ (progenitors), and ICAM1+/CD36+ (pre-adipocytes).

E, Absolute number of progenitor and pre-adipocytes from ob/ob-Veh and ob/ob-Rosi mice.

F-G Confocal of sorted lineage negative (CD45-, CD31-), PDGFRa+, DPP4+ and DPP4- cells differentiated for 4 days on DMI (dexamethasone, IBMX, and insulin) media, DAPI (nuclei), LipidTox (neutral lipids). Data represent mean ± SEM (n = 6 mice per group). Confocal images: 4 wells per conditions, 2 representative images per well were acquired. *P < 0.05; **P < 0.01; ***P < 0.001 by two-tailed Student’s t test.

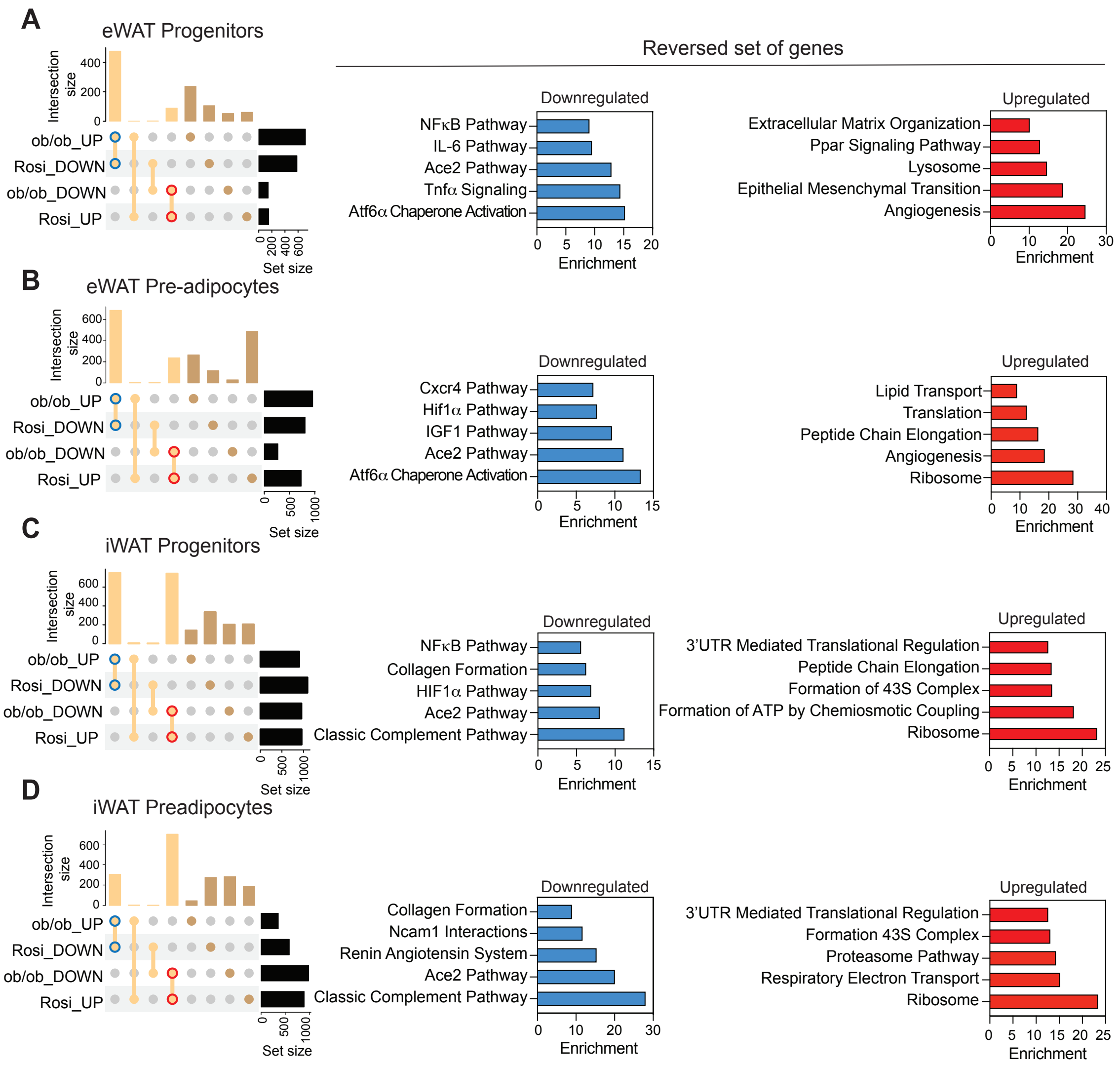

Fig 4. 5 Comparison of differentially expressed and enriched pathways in response to obesity and rosiglitazone treatment

A-D, UpSet plot illustrates intersections of differentially expressed genes (DEGs) for the 4 categories within eWAT progenitors (**A**), eWAT pre-adipocytes (**B**), iWAT progenitors (**C**), and iWAT pre-adipocytes (**D**), all at a Bonferroni-adjusted p-value < 0.05. The 4 categories include upregulated DEGs in obese mice than in lean mice (ob/ob_UP), down-regulated DEGs in obese mice than in lean mice (ob/ob_DOWN), up-regulated DEGs in response to Rosiglitazone treatment (Rosi_UP), down-regulated DEGs in response to Rosiglitazone treatment (Rosi_DOWN). Horizontal bars (set size) indicate total DEGs for each cluster in each plot. In the UpSet plots, dots point to the specific clusters for which the vertical bars for DEG counts are shown, and vertical lines between dots represent the intersections between two or more clusters. The blue circle signifies the set of DEGs that are upregulated in obese mice and downregulated in response to rosiglitazone treatment. Conversely, the red circle represents the DEGs that are downregulated in obese mice and upregulated following rosiglitazone treatment. Right bar plots illustrate the top enriched pathways in response to rosiglitazone treatment, which act to reverse the effects of obesity. Red bars represent pathways enriched from DEGs that are downregulated in obese mice and upregulated following rosiglitazone treatment. Conversely, the blue bars represent pathways enriched from DEGs that are upregulated in obese mice and downregulated following rosiglitazone treatment. All pathways displayed met the cut-off for statistical significance at Bonferroni corrected p values < 0.05. The enrichment score is calculated using the formula: (Number of overlapping genes / Number of genes in our cell type-specific gene set) × (20000 / Number of genes in the pathway).

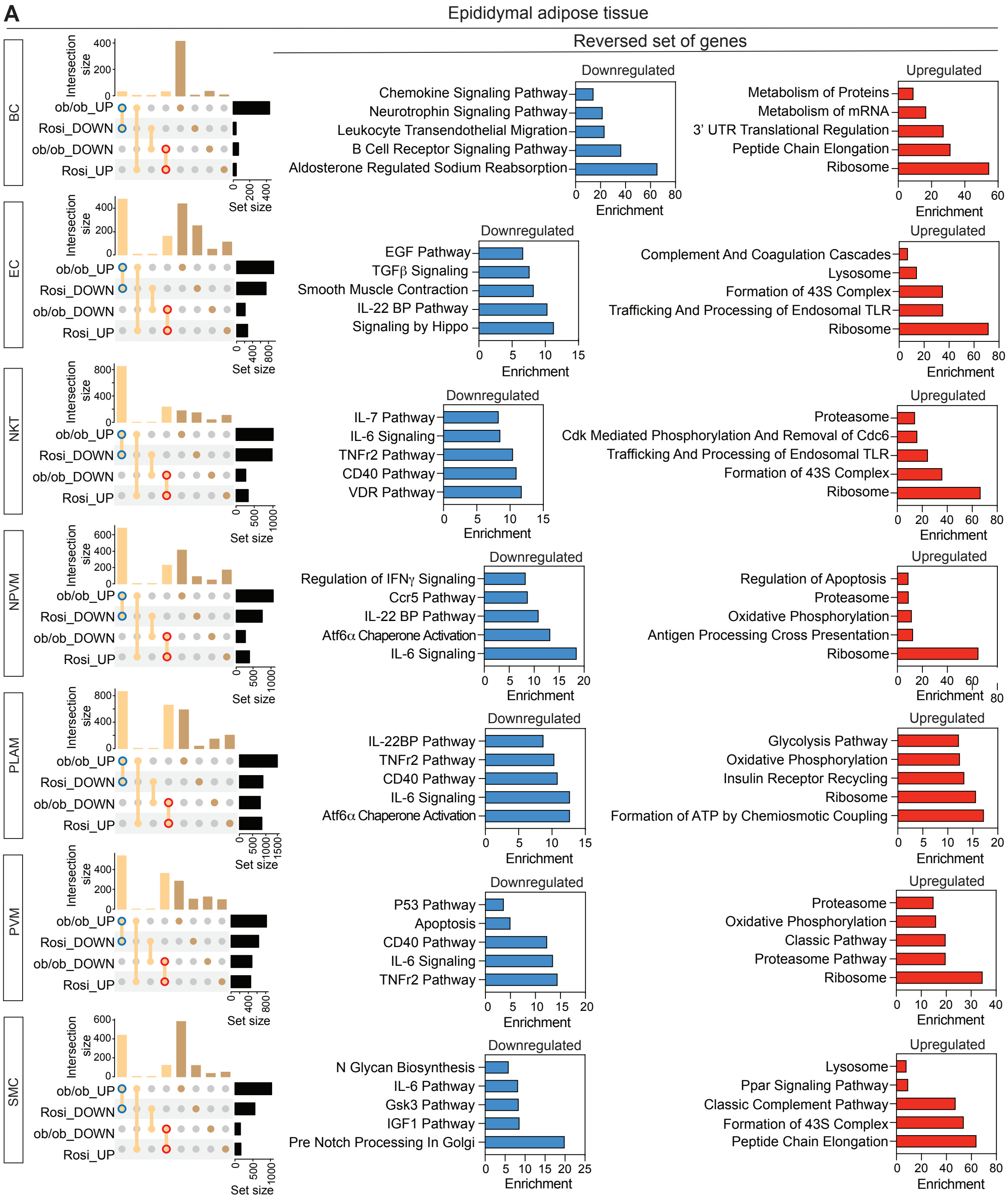

Sup Fig 4. 4 Effects of rosiglitazone treatment in the stromal vascular fraction of epididymal adipose tissue

UpSet plot illustrates intersections of DEGs for 4 categories within eWAT cell types all

at a Bonferroni-adjusted p-value < 0.05. The 4 categories include upregulated DEGs in obese mice than in lean mice (ob/ob_UP), down-regulated DEGs in obese mice than in lean mice (ob/ob_DOWN), up-regulated DEGs in response to rosiglitazone treatment (Rosi_UP), down-regulated DEGs in response to rosiglitazone treatment (Rosi_DOWN). Horizontal bars (set size) indicate total DEGs for each cluster in each plot. In the UpSet plots, dots point to the specific clusters for which the vertical bars for DEG counts are shown, and vertical lines between dots represent the intersections between two or more clusters. The blue circle signifies the set of DEGs that are upregulated in obese mice and downregulated in response to rosiglitazone treatment. Conversely, the red circle represents the DEGs that are downregulated in obese mice and upregulated following rosiglitazone treatment. Right bar plots illustrate the top enriched pathways in response to rosiglitazone treatment, which act to reverse the effects of obesity. Red bars represent pathways enriched from DEGs that are downregulated in obese mice and upregulated following Rosiglitazone treatment. Conversely, the blue bars represent pathways enriched from DEGs that are upregulated in obese mice and downregulated following rosiglitazone treatment. All pathways displayed meet the cut-off for statistical significance at Bonferroni corrected p values < 0.05. The enrichment score is calculated using the formula: (Number of overlapping genes / Number of genes in our cell type-specific gene set) × (20000 / Number of genes in the pathway).

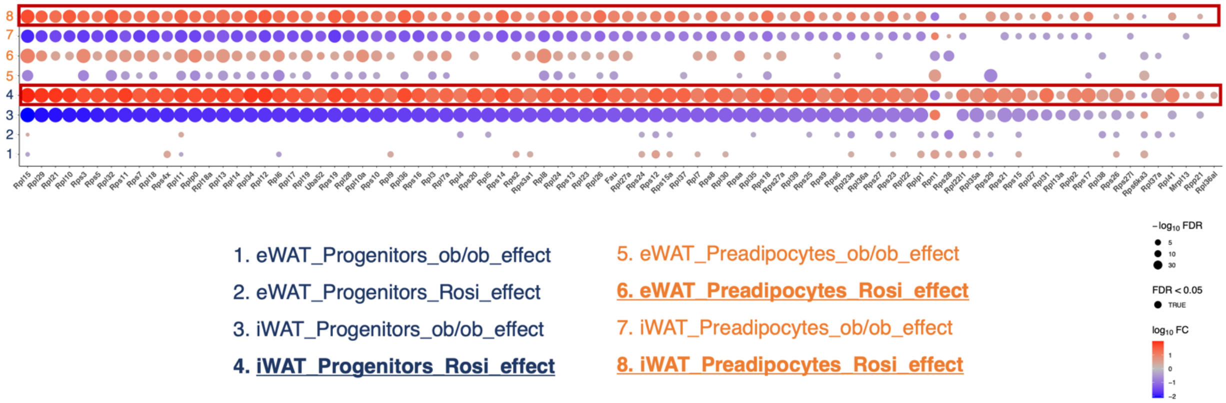

Fig 4. 6 PPARg-driven enhancement in translation efficiency

Dot plot showing differentially expressed ribosomal genes influenced by the ob/ob effect or Rosi effect in eWAT and iWAT progenitors or pre-adipocytes all at a Bonferroni-adjusted p-value < 0.05. The size of the dots reflect the -log10(FDR) of the DEGs and the color of the dots reflect the fold change of the DEGs.

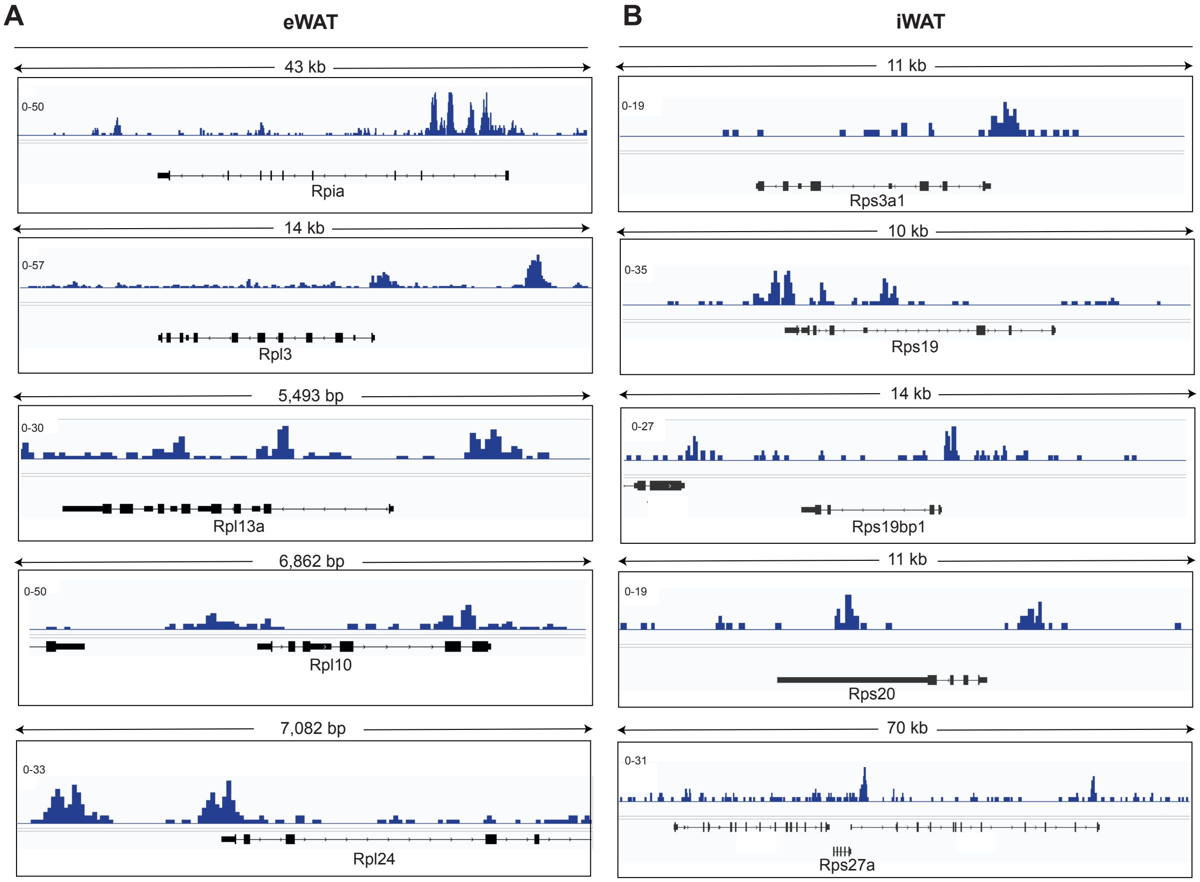

Fig 4. 7 PPARg binding sites in ribosomal genes
A, Visualization of peaks of PPARg binding sites in separate ribosomal genes in eWAT

B, Visualization of peaks of PPARg binding sites in separate ribosomal genes in iWAT

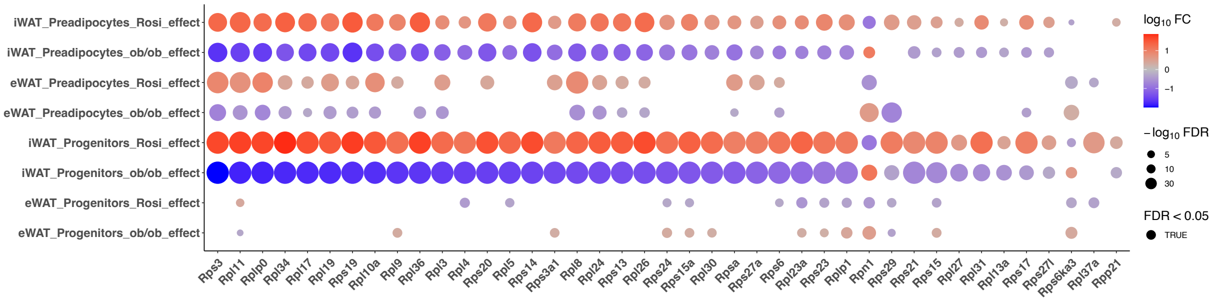

Supplementary Fig.4.5 Overlapping ribosomal genes between PPARg-ChIP Seq and scRNA-seq

Dot plot showing ribosomal DEGs from scRNA-seq that overlap with ribosomal genes that contain Pparg binding sites, as inferred from PPARG Chip-seq data. The size of each dot is proportional to the -log10(FDR) value of each differentially expressed gene (DEG), illustrating the level of statistical significance. The color of each dot corresponds to the fold change of each DEG, providing an indicator of the magnitude of gene expression changes.

References

1. Waterson, M. J. & Horvath, T. L. Neuronal Regulation of Energy Homeostasis: Beyond the Hypothalamus and Feeding. Cell Metab. 22, 962–970 (2015).
2. Chen, W., Balland, E. & Cowley, M. A. Hypothalamic Insulin Resistance in Obesity: Effects on Glucose Homeostasis. Neuroendocrinology 104, 364–381 (2017).
3. Giralt, M., Cereijo, R. & Villarroya, F. Adipokines and the Endocrine Role of Adipose Tissues. in Metabolic Control (ed. Herzig, S.) 265–282 (Springer International Publishing, 2016). doi:10.1007/164_2015_6.
4. Farkhondeh, T. et al. An Overview of the Role of Adipokines in Cardiometabolic Diseases. Molecules 25, 5218 (2020).
5. Swaab, D. F., Chung, W. C. J., Kruijver, F. P. M., Hofman, M. A. & Ishunina, T. A. Structural and Functional Sex Differences in the Human Hypothalamus. Horm. Behav. 40, 93–98 (2001).
6. Yang, C. F. et al. Sexually Dimorphic Neurons in the Ventromedial Hypothalamus Govern Mating in Both Sexes and Aggression in Males. Cell 153, 896–909 (2013).
7. Jin, J.-M. & Yang, W.-X. Molecular regulation of hypothalamus–pituitary–gonads axis in males. Gene 551, 15–25 (2014).
8. Bailey, M. & Silver, R. Sex differences in circadian timing systems: Implications for disease. Front. Neuroendocrinol. 35, 111–139 (2014).
9. Clark, T. D., Reichelt, A. C., Ghosh-Swaby, O., Simpson, S. J. & Crean, A. J. Nutrition, anxiety and hormones. Why sex differences matter in the link between obesity and behavior. Physiol. Behav. 247, 113713 (2022).

10. Heck, A. L. & Handa, R. J. Sex differences in the hypothalamic–pituitary–adrenal axis' response to stress: an important role for gonadal hormones. Neuropsychopharmacology 44, 45–58 (2019).
11. Jais, A. & Brüning, J. C. Hypothalamic inflammation in obesity and metabolic disease. J. Clin. Invest. 127, 24–32 (2017).
12. Pasquali, R. The hypothalamic–pituitary–adrenal axis and sex hormones in chronic stress and obesity: pathophysiological and clinical aspects. Ann. N. Y. Acad. Sci. 1264, 20–35 (2012).
13. Jacobson, L. Hypothalamic-Pituitary-Adrenocortical Axis: Neuropsychiatric Aspects. Compr. Physiol. 4, (2014).
14. Arnold, A. P. & Chen, X. What does the "four core genotypes" mouse model tell us about sex differences in the brain and other tissues? Front. Neuroendocrinol. 30, 1–9 (2009).
15. Itoh, Y. et al. Four Core Genotypes mouse model: localization of the Sry transgene and bioassay for testicular hormone levels. BMC Res. Notes 8, 69 (2015).
16. Dastani, Z. et al. Novel Loci for Adiponectin Levels and Their Influence on Type 2 Diabetes and Metabolic Traits: A Multi-Ethnic Meta-Analysis of 45,891 Individuals. PLOS Genet. 8, e1002607 (2012).
17. Morris, A. P. et al. Large-scale association analysis provides insights into the genetic architecture and pathophysiology of type 2 diabetes. Nat. Genet. 44, 981–990 (2012).

18. Ingelsson, E. et al. Detailed Physiologic Characterization Reveals Diverse Mechanisms for Novel Genetic Loci Regulating Glucose and Insulin Metabolism in Humans. Diabetes 59, 1266–1275 (2010).
19. Fritsche, L. G. et al. Seven new loci associated with age-related macular degeneration. Nat. Genet. 45, 433–439 (2013).
20. Kilpeläinen, T. O. et al. Obesity-susceptibility loci have a limited influence on birth weight: a meta-analysis of up to 28,219 individuals. Am. J. Clin. Nutr. 93, 851–860 (2011).
21. Mäkinen, V.-P. et al. Integrative Genomics Reveals Novel Molecular Pathways and Gene Networks for Coronary Artery Disease. PLoS Genet. 10, e1004502 (2014).
22. Macosko, E. Z. et al. Highly Parallel Genome-wide Expression Profiling of Individual Cells Using Nanoliter Droplets. Cell 161, 1202–1214 (2015).
23. Harris, G. C., Wimmer, M. & Aston-Jones, G. A role for lateral hypothalamic orexin neurons in reward seeking. Nature 437, 556–559 (2005).
24. Deem, J. D., Faber, C. L. & Morton, G. J. AgRP neurons: Regulators of feeding, energy expenditure, and behavior. FEBS J. 289, 2362–2381 (2022).
25. Gouveia, A., de Oliveira Beleza, R. & Steculorum, S. M. AgRP neuronal activity across feeding-related behaviours. Eur. J. Neurosci. 54, 7458–7475 (2021).
26. Stuart, T. et al. Comprehensive Integration of Single-Cell Data. Cell 177, 1888-1902.e21 (2019).
27. Ritchie, M. E. et al. limma powers differential expression analyses for RNA-sequencing and microarray studies. Nucleic Acids Res. 43, e47 (2015).

28. Kanehisa, M. & Goto, S. KEGG: kyoto encyclopedia of genes and genomes. Nucleic Acids Res. 28, 27–30 (2000).
29. Fabregat, A. et al. The Reactome Pathway Knowledgebase. Nucleic Acids Res. 46, D649–D655 (2018).
30. Nishimura, D. BioCarta. Biotech Softw. Internet Rep. 2, 117–120 (2001).
31. Liberzon, A. et al. The Molecular Signatures Database Hallmark Gene Set Collection. Cell Syst. 1, 417–425 (2015).
32. Hoeffer, C. A. & Klann, E. mTOR signaling: At the crossroads of plasticity, memory and disease. Trends Neurosci. 33, 67–75 (2010).
33. Nordvall, G., Forsell, P. & Sandin, J. Neurotrophin-targeted therapeutics: A gateway to cognition and more? Drug Discov. Today 27, 103318 (2022).
34. Subedi, L., Venkatesan, R. & Kim, S. Y. Neuroprotective and Anti-Inflammatory Activities of Allyl Isothiocyanate through Attenuation of JNK/NF-κB/TNF-α Signaling. Int. J. Mol. Sci. 18, 1423 (2017).
35. Wang, H. et al. Protocatechuic Acid Inhibits Inflammatory Responses in LPS-Stimulated BV2 Microglia via NF-κB and MAPKs Signaling Pathways. Neurochem. Res. 40, 1655–1660 (2015).
36. Ma, Y. J. et al. Neuregulins Signaling via a Glial erbB-2–erbB-4 Receptor Complex Contribute to the Neuroendocrine Control of Mammalian Sexual Development. J. Neurosci. 19, 9913–9927 (1999).
37. Ge, Y. & Wang, Y. T. GluA1-homomeric AMPA receptor in synaptic plasticity and neurological diseases. Neuropharmacology 197, 108708 (2021).

38. Franchini, L., Carrano, N., Di Luca, M. & Gardoni, F. Synaptic GluN2A-Containing NMDA Receptors: From Physiology to Pathological Synaptic Plasticity. Int. J. Mol. Sci. 21, 1538 (2020).
39. Brann, D. W. et al. Neuron-Derived Estrogen—A Key Neuromodulator in Synaptic Function and Memory. Int. J. Mol. Sci. 22, 13242 (2021).
40. Tozzi, A., Bellingacci, L. & Pettorossi, V. E. Rapid Estrogenic and Androgenic Neurosteroids Effects in the Induction of Long-Term Synaptic Changes: Implication for Early Memory Formation. Front. Neurosci. 14, (2020).
41. Lonsdale, J. et al. The Genotype-Tissue Expression (GTEx) project. Nat. Genet. 45, 580–585 (2013).
42. Arneson, D., Bhattacharya, A., Shu, L., Mäkinen, V.-P. & Yang, X. Mergeomics: a web server for identifying pathological pathways, networks, and key regulators via multidimensional data integration. BMC Genomics 17, 722 (2016).
43. Santos, S., Ferreira, H., Martins, J., Gonçalves, J. & Castelo-Branco, M. Male sex bias in early and late onset neurodevelopmental disorders: Shared aspects and differences in Autism Spectrum Disorder, Attention Deficit/hyperactivity Disorder, and Schizophrenia. Neurosci. Biobehav. Rev. 135, 104577 (2022).
44. Bangasser, D. A. & Cuarenta, A. Sex differences in anxiety and depression: circuits and mechanisms. Nat. Rev. Neurosci. 22, 674–684 (2021).
45. Kok, F. M., Groen, Y., Fuermaier, A. B. M. & Tucha, O. The female side of pharmacotherapy for ADHD—A systematic literature review. PLOS ONE 15, e0239257 (2020).

46. Picciotto, M. R., Brabant, C., Einstein, E. B., Kamens, H. M. & Neugebauer, N. M. Effects of galanin on monoaminergic systems and HPA axis: Potential mechanisms underlying the effects of galanin on addiction- and stress-related behaviors. Brain Res. 1314, 206–218 (2010).
47. Werling, D. M. & Geschwind, D. H. Sex differences in autism spectrum disorders. Curr. Opin. Neurol. 26, 146–153 (2013).
48. Comeras, L. B., Herzog, H. & Tasan, R. O. Neuropeptides at the crossroad of fear and hunger: a special focus on neuropeptide Y. Ann. N. Y. Acad. Sci. 1455, 59–80 (2019).
49. Cataldo, I., Azhari, A. & Esposito, G. A Review of Oxytocin and Arginine-Vasopressin Receptors and Their Modulation of Autism Spectrum Disorder. Front. Mol. Neurosci. 11, (2018).
50. Chiodini, I. et al. Hypothalamic-pituitary-adrenal activity in type 2 diabetes mellitus: role of autonomic imbalance. Metabolism 55, 1135–1140 (2006).
51. Flegal, K. M., Kruszon-Moran, D., Carroll, M. D., Fryar, C. D. & Ogden, C. L. Trends in Obesity Among Adults in the United States, 2005 to 2014. JAMA 315, 2284-2291, doi:10.1001/jama.2016.6458 (2016).
52. Gallagher, D. et al. Healthy percentage body fat ranges: an approach for developing guidelines based on body mass index. Am J Clin Nutr 72, 694-701, doi:10.1093/ajcn/72.3.694 (2000).
53. Stenholm, S. et al. Sarcopenic obesity: definition, cause and consequences. Curr Opin Clin Nutr Metab Care 11, 693-700, doi:10.1097/MCO.0b013e328312c37d (2008).

54. Roh, E. & Choi, K. M. Health Consequences of Sarcopenic Obesity: A Narrative Review. Frontiers in Endocrinology 11, doi:10.3389/fendo.2020.00332 (2020).
55. Karakelides, H., Irving, B. A., Short, K. R., O'Brien, P. & Nair, K. S. Age, obesity, and sex effects on insulin sensitivity and skeletal muscle mitochondrial function. Diabetes 59, 89-97, doi:10.2337/db09-0591 (2010).
56. Decaria, J. E., Sharp, C. & Petrella, R. J. Scoping review report: obesity in older adults. Int J Obes (Lond) 36, 1141-1150, doi:10.1038/ijo.2012.29 (2012).
57. Pontzer, H. et al. Daily energy expenditure through the human life course. Science 373, 808-812, doi:10.1126/science.abe5017 (2021).
58. Ghaben, A. L. & Scherer, P. E. Adipogenesis and metabolic health. Nat Rev Mol Cell Biol, doi:10.1038/s41580-018-0093-z (2019).
59. Wang, Q. A., Tao, C., Gupta, R. K. & Scherer, P. E. Tracking adipogenesis during white adipose tissue development, expansion and regeneration. Nat Med 19, 1338-1344, doi:10.1038/nm.3324 (2013).
60. Vishvanath, L. et al. Pdgfrβ+ Mural Preadipocytes Contribute to Adipocyte Hyperplasia Induced by High-Fat-Diet Feeding and Prolonged Cold Exposure in Adult Mice. Cell Metabolism 23, 350-359, doi:http://dx.doi.org/10.1016/j.cmet.2015.10.018 (2016).
61. Wang, Q. A. et al. Reversible De-differentiation of Mature White Adipocytes into Preadipocyte-like Precursors during Lactation. Cell Metabolism 28, 282-288.e283, doi:https://doi.org/10.1016/j.cmet.2018.05.022 (2018).
62. Spalding, K. L. et al. Dynamics of fat cell turnover in humans. Nature 453, 783-787, doi:10.1038/nature06902 (2008).

63. Palmer, A. K. & Kirkland, J. L. Aging and adipose tissue: potential interventions for diabetes and regenerative medicine. Experimental Gerontology 86, 97-105, doi:https://doi.org/10.1016/j.exger.2016.02.013 (2016).
64. Hepler, C., Vishvanath, L. & Gupta, R. K. Sorting out adipocyte precursors and their role in physiology and disease. Genes Dev 31, 127-140, doi:10.1101/gad.293704.116 (2017).
65. Burl, R. B. et al. Deconstructing Adipogenesis Induced by β3-Adrenergic Receptor Activation with Single-Cell Expression Profiling. Cell Metabolism 28, 300-309.e304, doi:https://doi.org/10.1016/j.cmet.2018.05.025 (2018).
66. Hepler, C. et al. Identification of functionally distinct fibro-inflammatory and adipogenic stromal subpopulations in visceral adipose tissue of adult mice. eLife 7, doi:10.7554/eLife.39636 (2018).
67. Schwalie, P. C. et al. A stromal cell population that inhibits adipogenesis in mammalian fat depots. Nature 559, 103-108, doi:10.1038/s41586-018-0226-8 (2018).
68. Merrick, D. et al. Identification of a mesenchymal progenitor cell hierarchy in adipose tissue. Science 364, doi:10.1126/science.aav2501 (2019).
69. Vijay, J. et al. Single-cell analysis of human adipose tissue identifies depot and disease specific cell types. Nat Metab 2, 97-109, doi:10.1038/s42255-019-0152-6 (2020).
70. Sárvári, A. K. et al. Plasticity of Epididymal Adipose Tissue in Response to Diet-Induced Obesity at Single-Nucleus Resolution. Cell Metab 33, 437-453.e435, doi:10.1016/j.cmet.2020.12.004 (2021).

71. Nguyen, H. P. et al. Aging-dependent regulatory cells emerge in subcutaneous fat to inhibit adipogenesis. Developmental cell 56, 1437-1451.e1433, doi:10.1016/j.devcel.2021.03.026 (2021).

72. Oh, J., Lee, Y. D. & Wagers, A. J. Stem cell aging: mechanisms, regulators and therapeutic opportunities. Nat Med 20, 870-880, doi:10.1038/nm.3651 (2014).

73. Ren, R., Ocampo, A., Liu, G. H. & Izpisua Belmonte, J. C. Regulation of Stem Cell Aging by Metabolism and Epigenetics. Cell Metab 26, 460-474, doi:10.1016/j.cmet.2017.07.019 (2017).

74. Ambrosi, T. H. et al. Aged skeletal stem cells generate an inflammatory degenerative niche. Nature, doi:10.1038/s41586-021-03795-7 (2021).

75. Pajvani, U. B. et al. Fat apoptosis through targeted activation of caspase 8: a new mouse model of inducible and reversible lipoatrophy. Nat Med 11, 797-803, doi:10.1038/nm1262 (2005).

76. Berry, R. & Rodeheffer, M. S. Characterization of the adipocyte cellular lineage in vivo. Nature Cell Biology 15, 302, doi:10.1038/ncb2696

77. Houlihan, D. D. et al. Isolation of mouse mesenchymal stem cells on the basis of expression of Sca-1 and PDGFR-α. Nat Protoc 7, 2103-2111, doi:10.1038/nprot.2012.125 (2012).

78. Viswanadhapalli, S., Dileep, K. V., Zhang, K. Y. J., Nair, H. B. & Vadlamudi, R. K. Targeting LIF/LIFR signaling in cancer. Genes Dis 9, 973-980, doi:10.1016/j.gendis.2021.04.003 (2022).

79. Guo, T. et al. LIFR-α-dependent adipocyte signaling in obesity limits adipose expansion contributing to fatty liver disease. iScience 24, 102227, doi:10.1016/j.isci.2021.102227 (2021).

80. Wang, Q. A. et al. Distinct regulatory mechanisms governing embryonic versus adult adipocyte maturation. Nature cell biology 17, 1099 (2015).

81. Picard, F. et al. Sirt1 promotes fat mobilization in white adipocytes by repressing PPAR-gamma. Nature 429, 771-776, doi:10.1038/nature02583 (2004).

82. Kanfi, Y. et al. SIRT6 protects against pathological damage caused by diet-induced obesity. Aging cell 9, 162-173 (2010).

83. Armoni, M. et al. FOXO1 represses peroxisome proliferator-activated receptor-gamma1 and -gamma2 gene promoters in primary adipocytes. A novel paradigm to increase insulin sensitivity. The Journal of biological chemistry 281, 19881-19891, doi:10.1074/jbc.M600320200 (2006).

84. Wang, M. C., Bohmann, D. & Jasper, H. JNK Extends Life Span and Limits Growth by Antagonizing Cellular and Organism-Wide Responses to Insulin Signaling. Cell 121, 115-125, doi:https://doi.org/10.1016/j.cell.2005.02.030 (2005).

85. Roichman, A. et al. SIRT6 Overexpression Improves Various Aspects of Mouse Healthspan. J Gerontol A Biol Sci Med Sci 72, 603-615, doi:10.1093/gerona/glw152 (2017).

86. Bluher, M., Kahn, B. B. & Kahn, C. R. Extended longevity in mice lacking the insulin receptor in adipose tissue. Science 299, 572-574, doi:10.1126/science.1078223 (2003).

87. Um, S. H. et al. Absence of S6K1 protects against age- and diet-induced obesity while enhancing insulin sensitivity. Nature 431, 200, doi:10.1038/nature02866

88. Lamming, D. W. & Sabatini, D. M. A Central role for mTOR in lipid homeostasis. Cell Metab 18, 465-469, doi:10.1016/j.cmet.2013.08.002 (2013).

89. Barzilai, N., Banerjee, S., Hawkins, M., Chen, W. & Rossetti, L. Caloric restriction reverses hepatic insulin resistance in aging rats by decreasing visceral fat. J Clin Invest 101, 1353-1361, doi:10.1172/jci485 (1998).

90. Redman, L. M. et al. Metabolic Slowing and Reduced Oxidative Damage with Sustained Caloric Restriction Support the Rate of Living and Oxidative Damage Theories of Aging. Cell Metab 27, 805-815 e804, doi:10.1016/j.cmet.2018.02.019 (2018).

91. Wu, Z. et al. Dietary Restriction Extends Lifespan through Metabolic Regulation of Innate Immunity. Cell Metab 29, 1192-1205 e1198, doi:10.1016/j.cmet.2019.02.013 (2019).

92. Brandhorst, S. et al. A Periodic Diet that Mimics Fasting Promotes Multi-System Regeneration, Enhanced Cognitive Performance, and Healthspan. Cell Metab 22, 86-99, doi:10.1016/j.cmet.2015.05.012 (2015).

93. Rondini, E. A. & Granneman, J. G. Single cell approaches to address adipose tissue stromal cell heterogeneity. Biochem J 477, 583-600, doi:10.1042/bcj20190467 (2020).

94. Ferrero, R., Rainer, P. & Deplancke, B. Toward a Consensus View of Mammalian Adipocyte Stem and Progenitor Cell Heterogeneity. Trends in Cell Biology 30, 937-950, doi:https://doi.org/10.1016/j.tcb.2020.09.007 (2020).

95. Sakers, A., De Siqueira, M. K., Seale, P. & Villanueva, C. J. Adipose-tissue plasticity in health and disease. Cell 185, 419-446, doi:10.1016/j.cell.2021.12.016 (2022).

96. Shao, M. et al. Pathologic HIF1α signaling drives adipose progenitor dysfunction in obesity. Cell Stem Cell 28, 685-701.e687, doi:10.1016/j.stem.2020.12.008 (2021).

97. Shan, B. et al. Perivascular mesenchymal cells control adipose-tissue macrophage accrual in obesity. Nat Metab 2, 1332-1349, doi:10.1038/s42255-020-00301-7 (2020).

98. Zhang, Q. et al. Distinct functional properties of murine perinatal and adult adipose progenitor subpopulations. Nat Metab 4, 1055-1070, doi:10.1038/s42255-022-00613-w (2022).

99. White, U. A. & Stephens, J. M. The gp130 receptor cytokine family: regulators of adipocyte development and function. Curr Pharm Des 17, 340-346, doi:10.2174/138161211795164202 (2011).

100. Richard, A. J. & Stephens, J. M. Emerging roles of JAK-STAT signaling pathways in adipocytes. Trends Endocrinol Metab 22, 325-332, doi:10.1016/j.tem.2011.03.007 (2011).

101. Marcelin, G. et al. A PDGFRalpha-Mediated Switch toward CD9(high) Adipocyte Progenitors Controls Obesity-Induced Adipose Tissue Fibrosis. Cell Metab 25, 673-685, doi:10.1016/j.cmet.2017.01.010 (2017).

102. Marcelin, G., Silveira, A. L. M., Martins, L. B., Ferreira, A. V. & Clement, K. Deciphering the cellular interplays underlying obesity-induced adipose tissue fibrosis. J Clin Invest 129, 4032-4040, doi:10.1172/JCI129192 (2019).

103. Xu, M. et al. Targeting senescent cells enhances adipogenesis and metabolic function in old age. eLife 4, e12997, doi:10.7554/eLife.12997 (2015).

104. van Deursen, J. M. The role of senescent cells in ageing. Nature 509, 439, doi:10.1038/nature13193 (2014).

105. Childs, B. G., Durik, M., Baker, D. J. & van Deursen, J. M. Cellular senescence in aging and age-related disease: from mechanisms to therapy. Nature Medicine 21, 1424, doi:10.1038/nm.4000 (2015).

106. Baker, D. J. et al. Naturally occurring p16Ink4a-positive cells shorten healthy lifespan. Nature 530, 184, doi:10.1038/nature16932

107. Minamino, T. et al. A crucial role for adipose tissue p53 in the regulation of insulin resistance. Nature Medicine 15, 1082, doi:10.1038/nm.2014

108. Chen, Y. W., Harris, R. A., Hatahet, Z. & Chou, K. M. Ablation of XP-V gene causes adipose tissue senescence and metabolic abnormalities. Proc Natl Acad Sci U S A 112, E4556-4564, doi:10.1073/pnas.1506954112 (2015).

109. Wang, C. Y. et al. Obesity increases vascular senescence and susceptibility to ischemic injury through chronic activation of Akt and mTOR. Sci Signal 2, ra11, doi:10.1126/scisignal.2000143 (2009).

110. Tchkonia, T. et al. Fat tissue, aging, and cellular senescence. Aging cell 9, 667-684 (2010).

111. Villaret, A. et al. Adipose tissue endothelial cells from obese human subjects: differences among depots in angiogenic, metabolic, and inflammatory gene expression and cellular senescence. Diabetes (2010).

112. Palmer, A. K. et al. Cellular Senescence in Type 2 Diabetes: A Therapeutic Opportunity. Diabetes 64, 2289-2298, doi:10.2337/db14-1820 (2015).

113. Schafer, M. J. et al. Exercise Prevents Diet-Induced Cellular Senescence in Adipose Tissue. Diabetes 65, 1606-1615, doi:10.2337/db15-0291 (2016).

114. Shirakawa, K. et al. Obesity accelerates T cell senescence in murine visceral adipose tissue. The Journal of Clinical Investigation 126, 4626-4639, doi:10.1172/JCI88606 (2016).

115. Krtolica, A., Parrinello, S., Lockett, S., Desprez, P. Y. & Campisi, J. Senescent fibroblasts promote epithelial cell growth and tumorigenesis: a link between cancer and aging. Proc Natl Acad Sci U S A 98, 12072-12077, doi:10.1073/pnas.211053698 (2001).

116. Campisi, J. Aging, cellular senescence, and cancer. Annual review of physiology 75, 685-705, doi:10.1146/annurev-physiol-030212-183653 (2013).

117. Ruhland, M. K. et al. Stromal senescence establishes an immunosuppressive microenvironment that drives tumorigenesis. Nat Commun 7, 11762, doi:10.1038/ncomms11762 (2016).

118. Asterholm, I. W. et al. Adipocyte inflammation is essential for healthy adipose tissue expansion and remodeling. Cell metabolism 20, 103-118 (2014).

119. Lackey, D. E. & Olefsky, J. M. Regulation of metabolism by the innate immune system. Nature Reviews Endocrinology 12, 15 (2016).

120. Hotamisligil, G. S. Inflammation, metaflammation and immunometabolic disorders. Nature 542, 177, doi:10.1038/nature21363

121. Rodier, F. et al. Persistent DNA damage signalling triggers senescence-associated inflammatory cytokine secretion. Nat Cell Biol 11, 973-979, doi:10.1038/ncb1909 (2009).

122. He, S. & Sharpless, N. E. Senescence in Health and Disease. Cell 169, 1000-1011, doi:10.1016/j.cell.2017.05.015 (2017).

123. Sapieha, P. & Mallette, F. A. Cellular Senescence in Postmitotic Cells: Beyond Growth Arrest. Trends in cell biology (2018).

124. Camell, C. D. et al. Aging Induces an Nlrp3 Inflammasome-Dependent Expansion of Adipose B Cells That Impairs Metabolic Homeostasis. Cell Metab 30, 1024-1039 e1026, doi:10.1016/j.cmet.2019.10.006 (2019).

125. Hildreth, A. D. et al. Single-cell sequencing of human white adipose tissue identifies new cell states in health and obesity. Nat Immunol 22, 639-653, doi:10.1038/s41590-021-00922-4 (2021).

126. Jaitin, D. A. et al. Lipid-Associated Macrophages Control Metabolic Homeostasis in a Trem2-Dependent Manner. Cell 178, 686-698 e614, doi:10.1016/j.cell.2019.05.054 (2019).

127. LaMarche, N. M. et al. Distinct iNKT Cell Populations Use IFNgamma or ER Stress-Induced IL-10 to Control Adipose Tissue Homeostasis. Cell Metab 32, 243-258 e246, doi:10.1016/j.cmet.2020.05.017 (2020).

128. CDC. Overweight & Obesity. Center for Disease Control and Prevention, 2023.

129. WHO. Obesity. World Health Organization, 2023.

130. Sakers, A., et al. Adipose-tissue plasticity in health and disease. Cell, 185, 419-446 (2022).

131. Merrick, D., et al. Identification of a mesenchymal progenitor cell hierarchy in adipose tissue. Science, 364, eaav2501 (2019).

132. Henriques, F., et al. Single-Cell RNA Profiling Reveals Adipocyte to Macrophage Signaling Sufficient to Enhance Thermogenesis. Cell Rep, 32, 107998 (2020).

133. Angueira, A.R., et al. Defining the lineage of thermogenic perivascular adipose tissue. Nat Metab, 3, 469-484 (2021).

134. Ramirez, A.K., et al. Single-cell transcriptional networks in differentiating preadipocytes suggest drivers associated with tissue heterogeneity. Nature Communications, 11, 2117 (2020).

135. Hildreth, A.D., et al. Single-cell sequencing of human white adipose tissue identifies new cell states in health and obesity. Nature Immunology, 22, 639-653 (2021).

136. Sárvári, A.K., et al. Plasticity of Epididymal Adipose Tissue in Response to Diet-Induced Obesity at Single-Nucleus Resolution. Cell Metab, 33, 437-453.e5 (2021).

137. Vijay, J., et al. Single-cell analysis of human adipose tissue identifies depot- and disease-specific cell types. Nature Metabolism, 2, 97-109 (2020).

138. Oguri, Y., et al. CD81 Controls Beige Fat Progenitor Cell Growth and Energy Balance via FAK Signaling. Cell, 182, 563-577.e20 (2020).

139. Min, S.Y., et al. Diverse repertoire of human adipocyte subtypes develops from transcriptionally distinct mesenchymal progenitor cells. Proceedings of the National Academy of Sciences, 116, 17970-17979 (2019).

140. Hepler, C., et al. Identification of functionally distinct fibro-inflammatory and adipogenic stromal subpopulations in visceral adipose tissue of adult mice. eLife, 7, e39636 (2018).

141. Spallanzani, R.G., et al. Distinct immunocyte-promoting and adipocyte-generating stromal components coordinate adipose tissue immune and metabolic tenors. Sci Immunol, 4 (2019).

142. Song, A., et al. Low- and high-thermogenic brown adipocyte subpopulations coexist in murine adipose tissue. J Clin Invest, 130, 247-257 (2020).

143. Rajbhandari, P., et al. Single cell analysis reveals immune cell–adipocyte crosstalk regulating the transcription of thermogenic adipocytes. eLife, 8, e49501 (2019).

144. Wang, Q.A., et al. Peroxisome Proliferator-Activated Receptor γ and Its Role in Adipocyte Homeostasis and Thiazolidinedione-Mediated Insulin Sensitization. Mol Cell Biol, 38 (2018).

145. Cariou, B., Charbonnel, B., Staels, B. Thiazolidinediones and PPARγ agonists: time for a reassessment. Trends Endocrinol Metab, 23, 205-15 (2012).

146. Chao, L., et al. Adipose tissue is required for the antidiabetic, but not for the hypolipidemic, effect of thiazolidinediones. J Clin Invest, 106, 1221-8 (2000).

147. Soccio, R.E., et al. Targeting PPARγ in the epigenome rescues genetic metabolic defects in mice. J Clin Invest, 127, 1451-1462 (2017).

148. Kang, J.G., et al. Mechanisms of adipose tissue redistribution with rosiglitazone treatment in various adipose depots. Metabolism, 59, 46-53 (2010).

149. Odegaard, J.I., et al. Macrophage-specific PPARgamma controls alternative activation and improves insulin resistance. Nature, 447, 1116-20 (2007).

150. Szanto, A., et al. STAT6 transcription factor is a facilitator of the nuclear receptor PPARγ-regulated gene expression in macrophages and dendritic cells. Immunity, 33, 699-712 (2010).

151. Davies, B.S., et al. The expression of GPIHBP1, an endothelial cell binding site for lipoprotein lipase and chylomicrons, is induced by peroxisome proliferator-activated receptor-gamma. Mol Endocrinol, 22, 2496-504 (2008).

152. Church, C.D., Berry, R., Rodeheffer, M.S. Isolation and study of adipocyte precursors. Methods Enzymol, 537, 31-46 (2014).

153. Zheng, G.X.Y., et al. Massively parallel digital transcriptional profiling of single cells. Nature Communications, 8, 14049 (2017).

154. Stefkovich, Megan, et al. Dpp4+ interstitial progenitor cells contribute to basal and high fat diet-induced adipogenesis. Molecular Metabolism, 54, 101357 (2021).

155. Siersbæk, Majken S., et al. Genome-wide profiling of peroxisome proliferator-activated receptor γ in primary epididymal, inguinal, and brown adipocytes reveals depot-selective binding correlated with gene expression. Molecular and cellular biology, 32, 3452-3463 (2012).

156. Ahmadian, Maryam, et al. PPARγ signaling and metabolism: the good, the bad and the future. Nature medicine, 19, 557-566 (2013).

157. Lee, Samuel M., et al. Rosiglitazone requires hepatocyte PPARγ expression to promote steatosis in male mice with diet-induced obesity. Endocrinology, 162 (2021).

158. Conn, Crystal S., et al. The major cap-binding protein eIF4E regulates lipid homeostasis and diet-induced obesity. Nature Metabolism, 3, 244-257 (2021).